Vloeibaar-kristaltoepassingen met in-het-vlak draaiende director

Liquid Crystal Devices with In-Plane Director Rotation

Chris Desimpel

Promotor: prof. dr. ir. K. Neyts
Proefschrift ingediend tot het behalen van de graad van
Doctor in de Ingenieurswetenschappen: Elektrotechniek

Vakgroep Elektronica en Informatiesystemen
Voorzitter: prof. dr. ir. J. Van Campenhout
Faculteit Ingenieurswetenschappen
Academiejaar 2005 - 2006

UNIVERSITEIT
GENT

ISBN 90-8578-073-X
NUR 959, 924
Wettelijk depot: D/2006/10.500/31

The most exciting phrase to hear in science,
the one that heralds new discoveries,
is not "Eureka!",
but rather "Hmm . . . that's funny . . . "

Isaac Asimov

Promotor:

prof. dr. ir. Kristiaan Neyts
Faculty of Engineering
Universiteit Gent

Members of the board of examiners:

prof. dr. ir. Daniël De Zutter (chairman)
prof. dr. ir. Alex De Vos (secretary)
prof. dr. ir. Kristiaan Neyts
prof. dr. ir. Marc Burgelman
prof. dr. ir. Herbert Desmet
prof. dr. ir. Dries Van Thourhout
dr. Dick K. G. de Boer (Philips Research, Eindhoven, the Netherlands)
dr. Fatiha Bougrioua (Université de Picardie - Jules Verne, Amiens, France)

Universiteit Gent
Faculty of Engineering
Department of Electronics and Information Systems
Liquid Crystals & Photonics Group
Sint-Pietersnieuwstraat 41
B-9000 Gent
Belgium

The research of Chris Desimpel was financially supported by the Institute for the Promotion of Innovation through Science and Technology in Flanders (IWT-Vlaanderen).

A word of Gratitude

During the past years at the university, I had the chance to meet lots of new and interesting people. All of them helped me in a certain way. Therefore, it is impossible to thank every single one personally. Nevertheless, a few people deserve a personal thank you.

A special thanks goes to my promotor, prof. K. Neyts. He gave me the opportunity to join the Liquid Crystal & Photonics Group of the Universiteit Gent. Despite his busy agenda, he is always available for scientific advise or help. Thanks to his continuous enthusiasm and support, our research group has become a close group of friends. I also want to acknowledge the Institute for the Promotion of Innovation by Science and Technology in Flanders (IWT-Vlaanderen) for their financial support.

An important group which I should not forget, are my colleagues of the Liquid Crystal & Photonics Group (Stefaan, Goran, Artur, Jeroen, Hans, Filip S., Filip B., Julien, Reza, Matthias and Angel) and the other research groups of the Physical Electronics. The positive atmosphere in the office, where everybody supports each other, is an example for many other labs.

Many thanks to Goran and Stefaan for their help in my quest for spelling mistakes.

Last but not least, I want to thank my parents and Tine who had to miss me a lot the last months but nevertheless helped me to keep my motivation.

Chris Desimpel
Gent, May 11, 2006

Table of Contents

Nederlandse Samenvatting

Vloeibaar-kristaltoepassingen met in-het-vlak draaiende director

Vloeibare kristallen zijn, door een aantal unieke eigenschappen, een veel gebruikt materiaal in tal van optische toepassingen. Vloeibare kristallen zijn optisch dubbelbrekend en laten dus toe om de polarisatie van het invallende licht te veranderen. De elektrische anisotropie van vloeibare kristallen heeft tot gevolg dat de uniaxiale as die de polarisatiewijziging controleert op eenvoudige wijze kan gestuurd worden door een extern aangelegd elektrisch veld. Daarom worden vloeibare kristallen vaak gebruikt als elektrisch controleerbare dubbelbrekende lagen.

Waarschijnlijk de meest bekende toepassing waarin de elektrische en optische anisotropie van vloeibare kristallen ten volle benut wordt, is het zogenaamde vloeibaar-kristalbeeldscherm of Liquid Crystal Display (LCD). Vloeibaar-kristalbeeldschermen hebben doorheen de jaren een belangrijk deel van de beeldschermmarkt ingenomen. Dankzij hun talrijke voordelen zoals beperkte gewicht en afmetingen, de eenvoud in productie en het lage energieverbruik hebben ze een aantal sterke troeven ten opzichte van andere beeldschermtechnologieën.

Het onderzoek naar vloeibare kristallen is nog steeds volop aan de gang, maar stilaan ligt het zwaartepunt van vloeibaar-kristalonderzoek minder bij beeldschermen. Sommige nieuwe toepassingen zoals Spatial Light Modulators zijn nauw verwant aan beeldschermen, terwijl andere zoals diffractieroosters, dubbelbrekende lagen en solitonen van een totaal andere aard zijn. Een gemeenschappelijk aspect van veel nieuwe onderzoeksonderwerpen is het gebruik van microscopisch kleine variaties. Microscopisch kleine veranderingen in een optisch materiaal brengen speciale effecten met zich mee zoals diffractie en verstrooi-

ing die een meer nauwkeurige studie vragen.

Mijn onderzoek begon als een studie van de optische eigenschappen van vloeibaar-kristalbeeldschermen. Het belangrijkste aandachtspunt was hierbij de in-het-vlak draaiende of in-plane switching (ips) mode. In de in-het-vlak draaiende mode wordt de gemiddelde richting van de moleculen in het vloeibaar kristal (de director) gedraaid in een vlak parallel met de substraten. Tijdens mijn onderzoek ben ik in contact gekomen met vele aspecten van vloeibare kristallen zoals modellering, optica, verankering aan het oppervlak, technologie, ... Gebruik makend van de in-het-vlak draaiende mode heb ik uiteindelijk een nieuw vloeibaar-kristalcomponent ontwikkeld met een aantal opvallende eigenschappen.

Het doctoraatswerk start met een beknopte inleiding tot vloeibare kristallen. In de inleiding worden de terminologie, de belangrijkste eigenschappen en het modelleren van vloeibare kristallen besproken. Speciale aandacht gaat hierbij naar de in-het-vlak draaiende mode die verder gebruikt wordt in de andere hoofdstukken.

Optische transmissie doorheen vloeibare kristallen

Vloeibaar-kristaltoepassingen hebben bijna steeds een optisch aspect. Om de resultaten van de optische experimenten te kunnen vergelijken met berekeningen is daarom een optisch algoritme nodig dat toelaat de optische transmissie doorheen de inhomogene anisotrope lagen te berekenen. Tijdens mijn onderzoek heb ik gebruik gemaakt van verschillende optische algoritmes. Voor eendimensionale lagen volstaat de Jones-matrix Methode. Dit is een eenvoudig 2×2 matrix algoritme dat toelaat op snelle wijze de transmissie doorheen het vloeibaar kristal te berekenen. Voor twee- en driedimensionale lagen, is een uitgebreider optisch algoritme vereist. Daarom worden eveneens de Rigorous Coupled Wave Method en de Reduced Grating Method gebruikt. Twee bestaande methoden die nauwkeurig de optische transmissie doorheen periodieke anisotrope media berekenen.

Nadeel van de Rigorous Coupled Wave Method en de Reduced Grating Method is echter dat deze tijdrovend zijn en een grote hoeveelheid computergeheugen vereisen. Daarom is een bijkomend vereenvoudigd optisch algoritme opgesteld, gebaseerd op de Jones-matrix Methode. Dit laat toe om een snelle berekening te maken van de optische transmissie doorheen twee- en driedimensionale dubbelbrekende lagen. De nauwkeurigheid van het vereenvoudigd algoritme wordt na-

gegaan door vergelijking met de resultaten van de andere algoritmes.

Oppervlakteverankering van vloeibare kristallen

Een tweede aspect van vloeibare kristallen waar uitgebreid aandacht aan wordt besteed is de verankering van de vloeibaar-kristalmoleculen aan het oppervlak. Voor toepassingen is een defectvrij vloeibaar-kristalvolume van belang. Daarom worden vloeibare kristallen gewoonlijk gebruikt in dunne lagen tussen twee glassubstraten. Controle van de director aan het oppervlak laat toe om een controleerbare en reproduceerbare verdeling van de director in het volume te bekomen. Gedurende vele jaren werd verankering gezien als een nevenaspect van vloeibaar-kristaltechnologie. Maar door het toenemend belang van zachte verankering in allerhande toepassingen treedt het de laatste jaren steeds meer op de voorgrond.

In klassieke toepassingen van vloeibare kristallen zoals bv. beeldschermen, wordt een vaste verankering aan het oppervlak gebruikt. Dit betekent dat de director van het vloeibaar kristal aan het oppervlak in een vaste richting wijst. In het hoofdstuk over verankering wordt dieper ingegaan op zachte verankering. Zachte verankering is een algemene term voor alle situaties waarin de oppervlaktedirector van het vloeibaar kristal kan gewijzigd worden door een extern aangelegd elektrisch veld of een elastische kracht. Dergelijke oppervlakken vertonen één of meerdere stabiele richtingen voor de oppervlaktedirector, maar elektrische of mechanische krachten kunnen de oppervlaktedirector wijzigen. Toepassingen van zachte verankering situeren zich in het domein van multistabiele vloeibaar-kristalconfiguraties, elektrisch controleerbare verankering en reductie van de drempelspanning en energieverbruik bij toepassingen. Het gedrag van de oppervlaktedirector wordt bepaald door de gebruikte materialen, de behandeling van het oppervlak en de oppervlaktetopologie.

Verschillende materialen worden in dit hoofdstuk vergeleken op het vlak van oppervlakteverankering, met als ultiem doel een materiaal te vinden waarbij de sterkte van de azimutale verankering van de director aan het oppervlak zo laag mogelijk is. Om de verschillende materialen te kunnen vergelijken werd een meetprocedure ontwikkeld waarmee de sterkte van de oppervlakteverankering experimenteel kan gemeten worden. Uiteindelijk werd de surfactant FC4430 aangeduid als materiaal met een zeer zwakke azimutale verankering van de director.

Ontwikkeling van een nieuw vloeibaar-kristalcomponent

De kennis die verzameld werd over de diverse aspecten van vloeibare kristallen heeft uiteindelijk geleid tot de ontwikkeling van een nieuw type vloeibaar-kristalcomponent met de unieke eigenschap dat de director 360° kan draaien in het vlak parallel met het substraatoppervlak. Het schakelen van de director wordt veroorzaakt door horizontale velden tussen zeshoekige elektroden in een honingraatmotief aan de onderzijde van een diëlektrische laag met bovenop een vloeibaar-kristallaag. De nieuw ontwikkelde component kan onder andere gebruikt worden als herconfigureerbare dubbelbrekende laag in optische experimenten.

Vooreerst wordt het werkingsprincipe van de component besproken aan de hand van driedimensionale berekeningen van de directorverdeling. De mogelijkheid om de director 360° te draaien in het vlak parallel met het substraatoppervlak wordt gedemonstreerd en aan de hand van uitgebreide optische simulaties wordt aangetoond dat de optische component zich voor de gemiddelde transmissie gedraagt als een homogene dubbelbrekende laag.

Uiteindelijk werd een testcomponent gebouwd in samenwerking met de Chalmers University of Technology in Göteborg (Zweden) en de vakgroep Intec van de Universiteit Gent. Door middel van experimenten kon worden aangetoond dat de director zoals vooropgesteld in 3 verschillende richtingen kan gealigneerd worden. Het ultieme doel, het draaien van de director over 360°, bleek niet volledig gerealiseerd te zijn. Op het eind van het hoofdstuk worden een aantal suggesties gegeven om de component te verbeteren en het draaien van de director over 360° mogelijk te maken.

De resultaten van dit werk heeft geresulteerd in een tiental artikels die gepresenteerd werden op internationale conferenties of gepubliceerd werden in internationale tijdschriften.

English Summary

Liquid crystal devices with in-plane director rotation

Liquid crystals are a widely used material in all kinds of optical applications. The growing importance of liquid crystals as a versatile material in optical setups rises from their unique features. Optically, nematic liquid crystals are uniaxially birefringent and thus modify the polarization state of the light wave propagating through the material. The electrical anisotropy allows to reorient the uniaxial axis, also known as the director, by application of an externally applied electric field. Therefore, liquid crystals serve as an electrically controllable birefringent layer.

The most familiar application of liquid crystals exploiting the optical and electrical anisotropy, is the liquid crystal display (LCD). Liquid crystal displays acquired an important position on the display market because they are lightweight, easy to produce and use a limited amount of power.

The research on liquid crystals is still very active, but the focus is moving gradually away from pure display research. The unique features of liquid crystals are now exploited in totally different domains. Some of the new applications like Spatial Light Modulators are closely related to displays, while others such as phase gratings, wave plates and solitary waves are of a totally different nature. A common aspect of many new research topics is miniaturization. Also in new liquid crystal devices, the involved electrodes and surface topologies have micrometer scale features. This leads to microscopic variations inside the liquid crystal material. Microscopic changes in an optical material induce special effects such as diffraction and scattering of the transmitted light which require further study.

My research started as a study of the optical characteristics of liquid crystal displays, focused on the in-plane switching mode of liquid crystals. During my research, I came in contact with many different aspects of liquid crystals: modeling, optics, anchoring, technology, ... Using the principle of in-plane switching, I worked toward a new type of liquid crystal device with remarkable features. The common aspect of the different topics treated in my phd thesis is liquid crystal devices with microscopic lateral variations.

The text starts with a brief introduction to the field of liquid crystals, explaining the main features of liquid crystals and how to model and use them. Special attention goes to the in-plane switching mode of liquid crystals, which is further used for different purposes in the other chapters.

Optical transmission through liquid crystals

Applications of liquid crystals involve almost always optics. For a comparison of the optical experiments with simulational results, a good tool is required for the calculation of the optical transmission through a liquid crystal layer. Therefore, three different existing optical algorithms are used to model the light propagation through the inhomogeneous liquid crystal layers. For one-dimensional liquid crystal layers, the Jones Matrix Method is used. A simple 2 matrix formalism which give fast and accurate results. For two and three-dimensional liquid crystal layers the Rigorous Coupled Wave Method and the Reduced Grating Method have been used. Two existing methods, which calculate accurately the optical transmission through periodic anisotropic media.

A drawback of the Rigorous Coupled Wave Method and the Reduced Grating Method is that they require a large amount of computer memory and calculation time. Therefore, an additional simplified transmission model was developed based on the Jones Matrix Method, which allows a fast and easy calculation of the transmission through thin three-dimensional liquid crystal layers. The usefulness and correctness of the simplified algorithm was demonstrated by comparison with the accurate optical algorithms.

Weak surface anchoring of liquid crystals

A second aspect of liquid crystals which is studied in more detail is the anchoring of the liquid crystal molecules at the surface. For appli-

cations it is important to obtain a region free of defects with a known director distribution. Therefore, liquid crystals are usually handled in thin layers between two substrates. Control of the director at the surfaces allows a reproducible director distribution in the liquid crystal volume. Therefore it is an important aspect when designing liquid crystal devices.

Anchoring was longtime considered a side topic of liquid crystals, but with the increasing importance of weak anchoring it entered in the spotlights in the past years. Nowadays, many of the mechanisms are being studied and it is a main challenge for chemists to develop new materials with specific anchoring properties. In classic liquid crystal devices such as displays strong anchoring is used, which implies that the surface director is fixed. In the chapter on anchoring, the phenomena related to weak anchoring of liquid crystals are studied. Weak anchoring is a generic term for all situations where the surface director can be altered by an externally applied field or elastic torque. Such surfaces exhibit one or more stable orientations of the surface director, but electric or mechanical torques can change the orientation of the surface director. The applications of weak anchoring are situated in the field of multistable nematic liquid crystal devices, electrically controllable anchoring and reduction of the threshold voltage and power consumption of liquid crystal devices. The behavior of the surface anchoring is determined by the surface material, treatment or structure.

Different alignment materials have been compared on their anchoring properties with as ultimate goal finding a surface material in which the azimuthal anchoring, the anchoring strength related to changes of the director twist angle at the surface, is reduced to a minimum. As a tool for comparing the materials, a measurement method was developed to accurately estimate the weak azimuthal anchoring strength at the surface. As a result, the surfactant FC4430 was indicated as a material with a weak azimuthal anchoring strength.

Development of a new liquid crystal reconfigurable wave plate

The knowledge gathered about the different aspects of liquid crystals was finally combined in the last chapter to develop a new type of liquid crystal device with the unique ability to rotate the liquid crystal director 360° in the plane parallel to the glass substrates. Switching of the liquid crystal director is possible to three different directions. The switching is induced by horizontal fields between hexagonal electrodes

in a honeycomb arrangement on the underside of a stack comprising a dielectric layer and a liquid crystal layer. Both switching and switching back are driven by an electric field. The presented device can serve as a reconfigurable wave plate in optical setups or as a pixel in display applications.

First, the principle operation of the device is studied by three-dimensional director simulations. The feasibility of a 360° in-plane director rotation was demonstrated and by means of extensive optical simulations, the working as a reconfigurable wave plate was shown. Finally, a first prototype has been built in collaboration with Chalmers University of Technology in Göteborg (Sweden) and Intec department at the Universiteit Gent. By microscope observation has been proved that the director could be aligned in three different directions as expected, but the ultimate 360° rotation did not succeed. At the end, a number of suggestions were given to improve the device and realize the 360° director rotation.

The results of the work has been published in two papers in SCI Journals and was presented at several scientific meetings and international conferences.

List of Tables

List of Figures

List of Symbols and Abbreviations

Abbreviations	
3-GPS	(3-glycidoxypropyl)trimethoxysilane
BCB	Benzocyclobutene
CRT	Cathode Ray Tube
EJMM	Extended Jones Matrix Method
FC4430	Novec surfactant (3M)
ips	In-plane switching
ITO	Indium Tin Oxide
JMM	Jones Matrix Method
LCD	Liquid Crystal Display
LED	Light Emitting Diode
OLED	Organic Light Emitting Diode
PDA	Personal Digital Assistant
PI	Polyimide
RCWM	Rigorous Coupled Wave Method
RGM	Reduced Grating Method

Electrical symbols	
μ_0	Magnetic permeability of vacuum ($\mu_0 = 4\pi\ 10^{-7}$ H/m)
$\overline{1}_x$	Unit vector along the x-direction
$\overline{1}_y$	Unit vector along the y-direction
$\overline{1}_z$	Unit vector along the z-direction

$\overline{\overline{\varepsilon}}$	Dielectric tensor
$\overline{D}$	Dielectric displacement
$\overline{E}$	Electric field
$\overline{H}$	Magnetic field
ρ	Dimensionless reduced surface-coupling parameter
ε_0	Dielectric permittivity of vacuum ($\varepsilon_0 = 8.85\ 10^{-12}$ F/m)
ε_d	Dielectric constant of a dielectric layer
ε_{lc}	Dielectric constant of a liquid crystal layer in the isotropic approximation
ζ	Normalized height
F	Free energy
f_d	Oseen-Frank distortion energy
f_e	Macroscopic electrostatic energy
f_s	Surfce anchoring energy
h	Normalized electric field
V_{th}	Threshold voltage
W_a	Azimuthal anchoring parameter
W_p	Polar anchoring parameter

Liquid crystal parameters

Δn	Birefringence or optical anisotropy: $n_\mathrm{e} - n_\mathrm{o}$
Δ	Width of a surface inversion wall
$\Delta\varepsilon$	Dielectric anisotropy: $\varepsilon_\parallel - \varepsilon_\perp$
γ_1	Rotational viscosity
$\overline{\epsilon}$	Easy direction of the surface director
$\overline{E}_{av}$	The average horizontal electric field
$\overline{n}$	Liquid crystal director
ϕ	Azimuthal angle of the liquid crystal director
ϕ_0	Azimuthal angle of the alignment
ϕ_{av}	Azimuthal angle of the average horizontal electric field
ϕ_a	Azimuthal angle of the analyzer transmission axis
ϕ_d	Average of the twist angle in all nodes of the mesh

ϕ_p	Azimuthal angle of the polarizer transmission axis
θ	Tilt angle of the liquid crystal director
θ_0	Pretilt of the liquid crystal director at the surface
θ_e	Angle of the electric field $\overline{E}$ with the xy-plane
$\varepsilon_{\parallel}$	Dielectric constant parallel to the uniaxial axis
$\varepsilon_{\perp}$	Dielectric constant perpendicular to the uniaxial axis
ξ_a	Extrapolation length for the azimuthal anchoring
a	Side length of a hexagonal electrode
b	Distance between two neighboring hexagonal electrodes
C_1	Driving configuration of the reconfigurable wave plate
C_2	Driving configuration of the reconfigurable wave plate
C_3	Driving configuration of the reconfigurable wave plate
d	Thickness of a liquid crystal layer
d_o	Thickness of the dielectric layer between the liquid crystal layer and the electrodes
g	Distance between the electrodes in the ips mode
k_{11}	Splay elastic constant
k_{22}	Twist elastic constant
k_{33}	Bend elastic constant
n_{d}	Refractive index of a dielectric layer
n_{eff}	Effective refractive index of the extra-ordinary mode
n_{e}	Extra-ordinary refractive index, parallel to the uniaxial axis
n_{o}	Ordinary refractive index, perpendicular to the uniaxial axis
s	Strength of a singular point
w	Width of the electrodes in the ips mode

Optical symbols

χ	Ellipticity angle of the polarization ellipse
Δ_x	Period in the x-direction
δ_x	Phase of the x-component of the Jones vector
Δ_y	Period in the y-direction
δ_y	Phase of the y-component of the Jones vector

λ	Wavelength in vacuum
ω	Angular frequency
$\overline{k}$	Wave vector inside a medium
$\overline{k}_0$	Wave vector in vacuum
ψ	Rotation of the longest principle axis of the polarization ellipse
φ_0	Azimuthal angle of the wave vector of a plane wave in air
ϑ	Inclination angle of the wave vector of a plane wave
ϑ_0	Inclination angle of the wave vector of a plane wave in air
c	Speed of light in vacuum ($c = 299\,792\,458\,\mathrm{m/s}$)
k	Wave number inside a medium
k_0	Wave number in vacuum

Chapter 1

Introduction

1.1 Background

Technology has experienced a tremendous evolution in the past years. People got used to the recently developed consumer applications and benefit without thinking from the numerous advantages. A vital part of many new devices is the user interface. Whereas 20 years ago, devices used to have a few LED's (light emitting diodes) to indicate their status, many small applications nowadays have an extensive menu on a color display.

Liquid crystal displays (LCD's) acquired an important position on this quickly growing market. Liquid crystal devices began their evolution as simple black-and-white displays with only a few pixels (the acronym for "picture element") in digital watches and calculators. At this time, they evolved toward full color displays with hundreds of thousands of pixels and are used in a wide variety of applications: desktop monitors, televisions, projectors, notebooks, car navigation systems, PDA's (personal digital assistant), digital cameras, audio-video equipment, mobile phones, head-up projection displays, ...

Important competitors in the field of displays are the classic cathode ray tube (CRT), organic light emitting diodes (OLED) and plasma displays. The heavy competition between different display technologies forces industry to continue improving their products. But LCD's benefit from some major advantages to fulfill the growing demands. They are small and lightweight, easy to produce, require low driving voltages and use a limited amount of power.

A large effort has been made over the past decade to produce LCD's at lower cost, with improved properties. The viewing angle dependency is reduced (color and intensity change when looking obliquely at the display), the colors have better saturation and the contrast ratio has increased (the ratio between the luminances of a white and a black screen).

The research on liquid crystals is still very active, but the focus is moving gradually away from pure display research. The unique features of liquid crystals are now exploited in totally different domains. Some of the new applications like Spatial Light Modulators are closely related to displays, while others such as phase gratings, wave plates and solitary waves are of a totally different nature. A common aspect of many new research topics is the exploitation of microscopic device features inside liquid crystals. Liquid crystals are typically used as a versatile material in optical setups. Microscopic variations in an optical material involve special effects such as diffraction and scattering of the transmitted light which require further study.

1.2 Goal

My work started as a study of the optical characteristics of liquid crystal displays, focused on the in-plane switching mode of liquid crystals. During my research, I came in contact with many different aspects of liquid crystals: modeling, optics, anchoring, technology, ... Using the principle of in-plane switching, I worked toward a new type of liquid crystal device with remarkable features.

In the second chapter, a brief introduction in the field of liquid crystals is given, explaining the main features of liquid crystals and how to model and use them. Special attention goes to the in-plane switching mode, which is further used in the other chapters.

Applications of liquid crystals involve almost always optics. For comparing optical experiments with simulational results, a good tool is required for calculating the optical transmission through a liquid crystal layer. Therefore, chapter 3 deals with the optical algorithms used during my work to model light propagation through inhomogeneous liquid crystal layers. At the end of the chapter a simplified transmission model is presented which allows fast and easy calculation of the transmission.

Chapter 4 investigates in more detail the anchoring of liquid crystals at surfaces, an important aspect of liquid crystal technology. Anchoring was longtime considered a side topic of liquid crystals, but with the increasing importance of weak anchoring it entered in the spotlights in the past years. Nowadays, many of the mechanisms are being studied and it is a main challenge for chemists to develop new materials with specific anchoring properties. Through a number of experiments different alignment materials are compared and a method is developed which allows to measure the anchoring strength at the surfaces.

Finally in chapter 5, a new type of liquid crystal device is introduced. The device is based on hexagonal electrodes in a honeycomb arrangement on one of the two parallel substrates. The simulations in the chapter focus mainly on its applications as a rotatable wave plate in optical setups, but other applications such as displays are also possible.

I have studied the principle of operation of this device by numerical simulations and optimized the dimensions. A first prototype has been realized in collaboration with Chalmers University of Technology in Göteborg (Sweden) and Intec department at the Universiteit Gent. The feasibility of the device is demonstrated throughout the experiments and some suggestions for future improvements are being made.

Chapter 2

Liquid Crystals

This chapter gives an introduction to liquid crystals, explaining the most important features and characteristics which will be used in the following chapters.

2.1 Material properties

Materials in nature can be divided into different phases, also called states of matter, depending on the mobility of the individual atoms or molecules. The obvious states of matter are the solid, the fluid and the gaseous state. In the solid state, intermolecular forces keep the molecules close together at a fixed position and orientation, so the material remains in a definite shape. In the fluid state, the molecules are still packed closely together, but they are able to move around. Hence a fluid does not have a rigid shape, but adapts to the contours of the container that holds it. Like a liquid, a gas has no fixed shape, but it has little resistance to compression because there is enough empty space for the molecules to move closer. Whereas a liquid placed in a container will form a puddle at the bottom of the container, a gas will expand to fill the container.

Although the three categories seem very well defined, the borders between the different states are not always clear. Apart from the three familiar states, there exist a large number of other intermediate phases. A simple example is a gel. A gel is not quite solid, neither is it a liquid. Liquid crystals are another important intermediate phase which exhibits features from both the solid and the fluid state. Liquid crystals

have the ordering properties of solids but they flow like liquids. Liquid crystalline materials have been observed for over a century but were not recognized as such until 1880s. In 1888, Friedrich Reinitzer [1] is credited for the first systematic description of the liquid crystal phase and reported his observations when he prepared cholesteryl benzoate, the first liquid crystal.

Ordinary fluids are isotropic in nature: they appear optically, magnetically, electrically, etc. to be the same from any direction in space. Although the molecules which comprise the fluid are generally anisometric in shape, this anisometry generally plays little role in macroscopic behavior. Liquid crystals [2–6] are composed of moderate size organic molecules which tend to be elongated, like a cigar. At high tem-

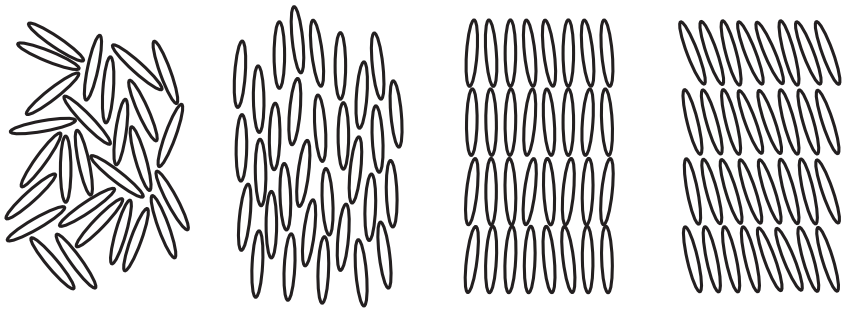

(a) Isotropic (b) Nematic (c) Smectic A (d) Smectic C

Figure 2.1: Different phases of a thermotropic liquid crystals.

peratures, the molecules will be oriented arbitrarily as shown in Figure 2.1(a) forming an isotropic liquid. Because of their elongated shape, under appropriate conditions, the molecules exhibit orientational order such that all the axes line up and form a so-called nematic liquid crystal (Figure 2.1(b)). The molecules are still able to move around in the fluid, but their orientation remains the same. Not only orientational order can appear, but also a positional order is possible. Liquid crystals exhibiting some positional order are called smectic liquid crystals. In smectics, the molecular centers of mass are arranged in layers and the movement is mainly limited inside the layers as illustrated in Figures 2.1(c) and 2.1(d). If the molecules are on average oriented perpendicular to the layers one speaks of a Smectic A phase, if they are oriented at an angle to the layer normal one speaks of Smectic C.

Beside these simple examples, more complicated ways of stacking

are possible, giving rise to many other types of liquid crystals. Chiral molecules, molecules without mirror symmetry, can give rise to helices comprising cholesteric liquid crystal phases. In ferroelectric or antiferroelectric liquid crystals the smectic layers possess a permanent polarization which is constant or alternating between successive layers respectively [7–9]. The nematic liquid crystal phase is by far the most important phase for applications. In the rest of this document only the nematic phase of liquid crystals is used.

In the nematic phase all molecules are aligned approximately parallel to each other. In each point a unit vector $\overline{n}$ can be defined, parallel to the average direction of the long axis of the molecules in the immediate neighborhood. This vector, known as the director, is not constant throughout the whole medium, but is a function of space $\overline{n}(x, y, z)$. For practical use, the director is usually specified by the twist and tilt angle as illustrated in Figure 2.2. The azimuthal angle ϕ between the positive x-axis and the projection of the liquid crystal director on the xy-plane is defined as the twist angle or azimuthal angle of the director. The angle θ between the director and its projection on the xy-plane is called the tilt angle. The vectorial representation of the director is not unambigu-

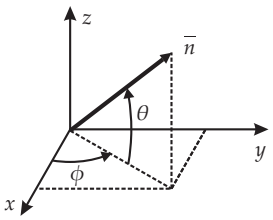

Figure 2.2: Definition of the twist angle ϕ and the tilt angle θ of the liquid crystal director $\overline{n}$.

ous. Physically there is no difference between the director orientations $\overline{n}$ and $-\overline{n}$, since as many molecules in the material have the tail pointing upward as downward. Unless specified otherwise the xy-plane in this work will always coincide with the bottom glass substrate, with the z-axis pointing toward the top substrate. In two-dimensional problems, there is no variation along the y-direction and only the xz-plane is represented.

Nematic liquid crystals have uniaxial symmetry, which means that in a homogeneous liquid crystal medium a rotation around the director does not make a difference. The bulk ordering has a profound influence

on the way light and electric fields behave in the material. Nematic liquid crystals are uniaxially anisotropic: the electrical and optical parameters are different if considered along the director or in a plane perpendicular to it.

Figure 2.3 shows the molecular structure of a typical rod-like liquid crystal molecule. It consists of two or more ring systems connected by a central linkage group [5, 10]. The presence of the rings provides

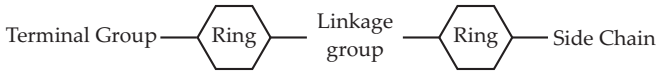

Figure 2.3: Molecular structure of a typical liquid crystal.

the short range molecular forces needed to form the nematic phase, but also affects the electrical and elastic properties. The chemical stability of liquid crystals, their resistance to e.g. moisture or ultraviolet radiation, depends strongly on the central linkage group. Compounds with a single bond in the center are among the most stable ones. At one side of the rings there is a long side chain which strongly influences the elastic constants and the transition temperature of the liquid crystal phases. At the other end, a terminal group is connected, which determines the dielectric constant and its anisotropy. Figure 2.4 shows four

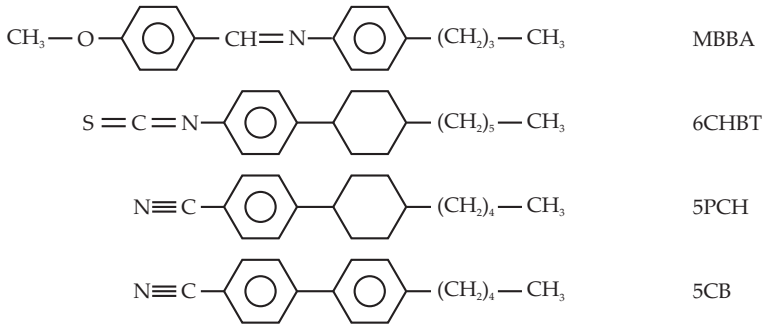

Figure 2.4: The molecular structure of four liquid crystal materials: MBBA (4′ - methoxybenzylidiene - 4 - butylaniline), 6CHBT (4 - trans - n - hexyl - cyclohexyl - isothiocyanatobenzene), 5PCH (4 - (trans - 4′ - pentyl - cyclohexyl) - benzonitril) and 5CB (4 - pentyl - 4′ - cyanobiphenyl).

examples of liquid crystal molecules [4,10–12]. Apart from the rod-like molecules, more advanced-shaped liquid crystals are possible such as

disk-like or banana-shaped liquid crystals which can give rise to other types of ordering.

The phase in which a pure liquid crystal (with only one type of molecule) exists depends on the temperature. Pure liquid crystals, or mixtures of them, in which the phase is controlled by temperature are called thermotropic liquid crystals. The Brownian motion of the molecules increases with the temperature, reducing the order in the material. At high temperature, orientational order is lost and the material changes to the isotropic phase. When decreasing the temperature, the material changes to the nematic phase. The temperature at which the phase transition occurs, is specific for each material and is called the nematic-isotropic transition temperature or clearing point. By further lowering the temperature, the phase can change to the smectic A phase, the smectic C and finally to the solid state. Each of the phase transitions occurs at a specific temperature, but depending on the material additional phases can appear or some can be missing.

Table 2.1 gives an overview of the temperature range of the nematic phase for the liquid crystals used in this work [4,10–12]. Pure materials such as 6CHBT, 5CB and 5PCH have a limited temperature range in which the nematic phase occurs. ZLI-4792 and E7 [5, 10] are so-called eutectic mixtures, designed to operate in a broader temperature range. The nematic temperature range of a mixture of nematic liquid crystals can be several orders of magnitude larger than that of the individual components. The mixture for which the nematic temperature range is maximal is called eutectic [2, 5, 10].

Table 2.1: Temperature range of the nematic phase of the used liquid crystals

	E7	ZLI-4792	6CHBT	5CB	5PCH
Melting point (°C)	-10	-40	12.5	24	30
Clearing point (°C)	60.5	92	43	35.3	55

Beside the thermotropic liquid crystals, a different class of liquid crystals is called lyotropic. These are mixtures of rod-like molecules in an isotropic solvent and the concentration of the solution is primarily responsible for the occurring phase. Lyotropic liquid crystals are mainly of interest in biological applications and exhibit a considerable number of different phases. In our research, only thermotropic liquid crystal are examined.

2.2 Alignment

In a glass vessel a liquid crystal appears as an opaque milky fluid. The random variation of the director in the material on a micrometer scale is the main cause of the light scattering.

For applications, it is important to obtain a region free of defects with a known director distribution. Therefore, liquid crystals are usually handled in thin layers between two substrates. Control of the director at the surfaces allows reproducible director orientations as illustrated in Figure 2.5. The fixed orientation of the surface director forces the director in the bulk to follow this direction. Two commonly used types of alignment are planar and homeotropic alignment. In planar alignment the surface director is oriented parallel to the surface, for homeotropic alignment it is oriented perpendicular to the surface.

Homeotropic alignment can be achieved by treating the surface with a surfactant such as HTAB (hexadecyl trimethyl ammonium bromide). The molecules of HTAB tend to align themselves and the liquid crystal director above perpendicular to the substrate surface.

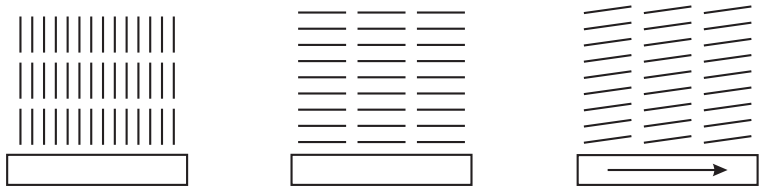

(a) homeotropic (b) planar (c) planar with pretilt

Figure 2.5: Different possibilities for aligning liquid crystals at a surface, to control the director orientation in the volume.

Many materials give rise to planar alignment, but an additional operation is required to select the desired azimuthal angle. For example, certain materials (e.g. polyvinylalcohol or polyvinylcinnamate) when illuminated with polarized ultraviolet light, can force the surface director to align parallel to the surface along a chosen direction. This process is known as photoalignment [13–15]. Another simple and widely used process to achieve planar alignment is rubbing. A polymer layer (e.g. polyimide, nylon or polyvinylalcohol) is deposited on the surface and rubbed with a soft tissue [16]. A liquid crystal deposited on the rubbed polymer surface will exhibit a surface director parallel to the direction

of rubbing with a small tilt angle. The direction of rubbing and the resulting surface director are shown in Figure 2.5(c). The azimuthal direction of rubbing is indicated with the pretwist ϕ_0, called the rubbing or alignment direction. The tilt angle at the rubbed surface θ_0 is named the pretilt.

A more detailed treatment of the alignment of liquid crystals at the surface will be given in the chapter on weak anchoring.

2.3 Electric and elastic properties

As a result of the uniaxial anisotropy, an electric field experiences a different dielectric constant when oscillating in a direction parallel or perpendicular to the director. The difference $\Delta\varepsilon = \varepsilon_{\parallel} - \varepsilon_{\perp}$ is called the dielectric anisotropy. If the dielectric constant along the director $\varepsilon_{\parallel}$, is larger than in the direction perpendicular to it $\varepsilon_{\perp}$, one speaks of positive anisotropy. The dielectric displacement $\overline{D}$ and the electric field $\overline{E}$ are related to each other by a dielectric tensor of rank two. In case the director is parallel to the z-axis, the tensor relation can be written as

$$\overline{D} = \varepsilon_0 \overline{\overline{\varepsilon}} \cdot \overline{E} = \varepsilon_0 \begin{pmatrix} \varepsilon_{\perp} & 0 & 0 \\ 0 & \varepsilon_{\perp} & 0 \\ 0 & 0 & \varepsilon_{\parallel} \end{pmatrix} \cdot \overline{E}, \tag{2.1}$$

with $\varepsilon_0 = 8.85\ 10^{-12}$ F/m the dielectric permittivity of vacuum. Due to the anisotropy, the dielectric displacement $\overline{D}$ and the induced dipole moment are not parallel to the electric field, except when the director $\overline{n}$ is parallel or perpendicular to the electric field $\overline{E}$. Therefore, a torque

$$\overline{\Gamma} = \varepsilon_0 \Delta\varepsilon \left(\overline{n}.\overline{E}\right)\left(\overline{n} \times \overline{E}\right) \tag{2.2}$$

is exerted on the director. For materials with positive anisotropy, the director prefers to align parallel to the electric field. Liquid crystals with a negative anisotropy tend to orient themselves perpendicularly to the electric field.

In a configuration with an externally applied electric field, the macroscopic electrostatic energy per unit volume can be expressed as a function of the electric field $\overline{E}$ and the director $\overline{n}$:

$$f_e = \frac{1}{2}\,\overline{D} \cdot \overline{E} = \frac{\varepsilon_0}{2}\left(\Delta\varepsilon \left(\overline{n} \cdot \overline{E}\right)^2 + \varepsilon_{\perp}\left(\overline{E} \cdot \overline{E}\right)\right). \tag{2.3}$$

The reorientation of the liquid crystal director by an externally applied electric field is one of the most exploited characteristic of liquid crystals. It is the base of operation for the so-called liquid crystal displays (LCD's).

The externally applied electric field $\overline{E}$ is often generated by electrodes on the bottom and/or top substrate. For optical devices transparent electrodes are used, made from Indium Tin Oxide (ITO). Ionic contamination of the liquid crystal material lowers the effective electric field that acts on the director. Since only squares of the electric field and the director are present in the electrostatic energy (2.3), the direction of the field $\pm\overline{E}$ does not make a difference. Therefore, to avoid negative effects of ions moving in the liquid crystal such as image sticking and flicker [17–21], the applied voltages used in applications are always square waves with alternating positive and negative pulses. Also in this work, applied voltages are without exception assumed to be square waves.

A liquid crystal medium prefers a uniform director distribution. A variation of the director in space induces an increase of the free energy. According to the elastic theory for liquid crystals, the distortion energy related to the variation of the director in space can be written as [3, 10]

$$f_d = \frac{1}{2}\left[k_{11}\left(\nabla\cdot\overline{n}\right)^2 + k_{22}\left(\overline{n}\cdot\nabla\times\overline{n}\right)^2 + k_{33}\left(\overline{n}\times\nabla\times\overline{n}\right)^2\right], \qquad (2.4)$$

with the three elastic constants k_{11}, k_{22} and k_{33}. This equation is known as the Oseen-Frank distortion energy. The three terms in the equation are related to distortion due to splay, twist and bend respectively as illustrated in Figure 2.6.

(a) splay (b) twist (c) bend

Figure 2.6: Twist, bend and splay distortion of the liquid crystal director.

Calculations of the equilibrium director distribution involve mini-

mizing the total free energy of the volume. In our approach, a constant voltage is applied to the electrodes, in which case the Gibbs free energy of the liquid crystal medium [22, 23]

$$F = \int_V \left[f_d\left(\overline{n}\right) - f_e\left(\overline{n}, \overline{E}\right) \right] \, dV. \tag{2.5}$$

must be minimized using the Euler-Lagrange equation. During my research I used different numerical tools to perform the necessary calculations. For one-dimensional calculations with plane electrodes at top and bottom, I used the software tool Glue [24]. Glue was developed in the Liquid Crystals & Photonics Group of the Universiteit Gent. It performs calculations of the director distribution and the optical transmission for one-dimensional liquid crystal layers as a function of the applied voltage or wavelength of the incident light.

Two- or three-dimensional simulations have been performed using a dynamic three-dimensional Liquid Crystal Director Simulation tool MonLCD [25–29], developed by the Computer Modelling Group of University College London in the framework of the European project MonLCD (G5RD-CT-2000-00115). The method is based on an approach starting from the Oseen-Frank elastic distortion energy density and the electrostatic energy of the liquid crystal. It calculates the dynamic evolution of the liquid crystal director, which is governed by the three relaxation equations

$$\frac{\partial F}{\partial n_\delta} + \frac{\partial}{\partial \dot{n}_\delta} \left(\frac{\gamma_1}{2} \int_V \dot{n}_\mu \dot{n}_\mu dV \right) = 0, \tag{2.6}$$

with $\mu, \delta = x, y, z$ and using the Einstein summation convention with respect to μ. γ_1 is the rotational viscosity of the liquid crystal material. A finite elements approach is used to solve the above system of differential equations for the director and the electric fields. A detailed description of the algorithm used for the relaxation and minimization of the total free energy and the calculation of the potential distribution are given in references [28–30]. A limited number of two-dimensional director calculations have also been performed using the commercial software tool 2dimMOS [31].

Table 2.2 gives an overview of the electrical and elastic parameters for the liquid crystals used for the experiments and simulations in this work [4, 10–12, 32].

Table 2.2: Electrical parameters of the used liquid crystals

	E7	ZLI-4792	6CHBT	5CB	5PCH
$\varepsilon_{\parallel}$	19.6	8.3	12	19.7	17.1
$\varepsilon_{\perp}$	5.1	3.1	4	6.7	5
$\Delta\varepsilon$	14.5	5.2	8	13	12 .1
k_{11} (pN)	12	13.2	8.57	6.4	8.5
k_{22} (pN)	9	6.5	3.7	3	5.1
k_{33} (pN)	19.5	18.3	9.51	10	16.2
γ_1 (mPa.s)	0.15	0.1232	0.083	0.081	0.123

2.4 One-dimensional configurations

Figure 2.7 shows three examples of liquid crystal layers sandwiched between two substrates. On the surfaces in contact with the liquid crystal, electrodes and alignment layers are deposited. A voltage applied over the electrodes generates an electric field along the z-axis, perpendicular to the surfaces. From the minimization of (2.5) results a one-dimensional director distribution, which varies along the z-axis.

In Figure 2.7(a) the alignment layers of both surfaces were rubbed in the same direction. This is called a π-cell or splay cell. The obtained director distribution is inhomogeneous and shows a splay distortion. Technologically this cell is less attractive since it suffers from inhomogeneous switching. The director in the middle of the layer, the midplane, is perpendicular to the electric field and feels no net torque, while just above and below the director is forced to rotate in opposite directions. This leads to domains with different switching directions. A homoge-

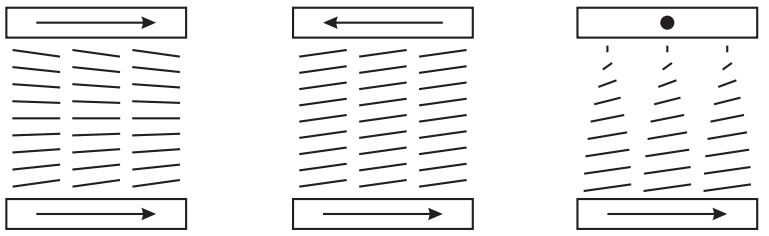

(a) splay (b) anti-parallel (c) twisted nematic

Figure 2.7: Different configurations of liquid crystal layers between two surfaces with rubbed alignment layers with no externally applied electric field.

neous director distribution during switching is obtained when the top and bottom substrate are rubbed in opposite direction as illustrated in the anti-parallel rubbed liquid crystal cell in Figure 2.7(b). An angle of 90° between the rubbing at the top and bottom substrate results in a linear variation of the twist angle along the surface normal. This is referred to as a twisted nematic cell [33].

The distance d, between the top and bottom substrate in a liquid crystal cell ranges typically from 1 to 100 μm, depending on the used liquid crystal and the intended application. The two surfaces are kept parallel at a constant distance by spacers, microscopic spheres or rods made of polymer or glass. The spacers are mixed in the glue that holds the two substrates together and if necessary also spread on the whole substrate surface by spinning.

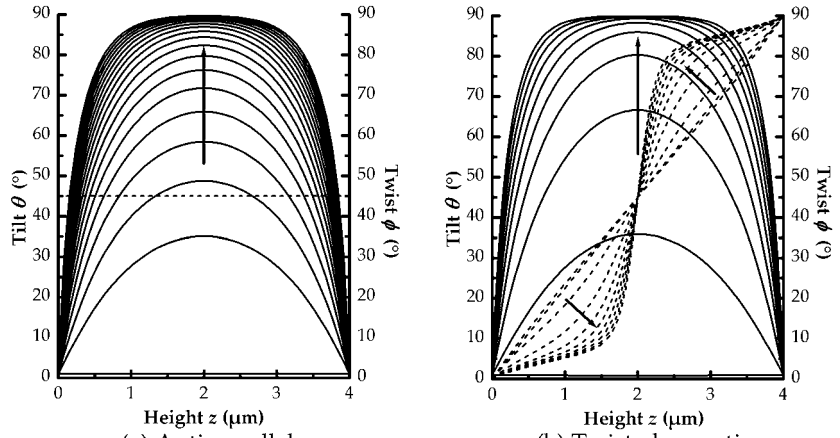

Figure 2.8: Tilt and twist distribution for voltages from 0 to 5 V in an anti-parallel rubbed and a twisted nematic liquid crystal cell. The full curves represent the tilt angle, the dashed curves correspond with the twist. The arrows indicate the direction in which the voltage increases.

Figure 2.8 shows the variation of the tilt angle θ and the twist angle ϕ along the surface normal for different values of the applied voltage for the anti-parallel rubbed and the twisted nematic liquid crystal cell. The calculations are done with Glue, using a layer thickness d of 4 μm and the parameters of the liquid crystal E7. The anti-parallel liquid crystal cell has a pretwist of 45° and the twisted nematic was aligned along the x and y-axis respectively at the top and bottom surface. The tilt angle variation as a function of the height z is drawn as a full line

and looks similar for the anti-parallel rubbed and twisted nematic cell. At 0 V, the tilt equals the pretilt as was shown in Figures 2.7(b) and 2.7(c). With an increasing electric field the midplane director starts tilting toward 90°.

In the anti-parallel rubbed liquid crystal cell, the twist angle is not influenced by the electric field. In the twisted nematic cell, the twist at 0 V varies linearly from 0 to 90°(see Figure 2.7(c)). By increasing the applied voltage, the 90° rotation is concentrated around the midplane, because a change in the azimuth requires less energy if the tilt is close to 90°.

At high voltages, both cells can be approximated by a stack of three twistless layers. At the two surfaces, a thin layer is present with a constant twist angle equal to the alignment direction (ϕ = 45° for Figure 2.8(a) and ϕ is either 0° or 90° for Figure 2.8(b)). The tilt angle θ in the layers varies quickly from θ_0 at the surface to 90°. Between the two layers at the surfaces lies a thick homogeneous layer with the director perpendicular to the surfaces (θ = 90°).

2.5 In-Plane switching

The in-plane switching (ips) mode of liquid crystals [34–37] is based on the principle of a rotatable wave plate. The liquid crystal layer, with thickness d, is sandwiched between two glass substrates as shown in Figure 2.9.

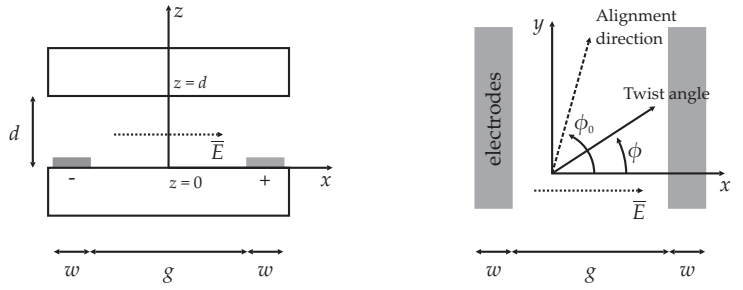

(a) side view: coordinate axes x and z (b) top view: coordinate axes x and y

Figure 2.9: Schematic drawing of the in-plane switching mode of a liquid crystal cell

The director at top and bottom is aligned by anti-parallel rubbing

along the azimuthal direction ϕ_0 with a small pretilt and forms a uniform birefringent layer. Whereas in the previous section, the positive and negative electrodes were positioned on the opposite glass plates, here the positive and negative electrodes are both positioned on the bottom glass substrate forming a pattern of parallel interdigitated stripes along the y-direction at a small angle to the rubbing direction. The width of the electrodes and the gap between the electrodes are indicated as w and g. A voltage applied over the electrodes generates an electric field $\overline{E}$ between the electrodes. Whereas in the previous section, the electric field $\overline{E}$ was oriented parallel to the z-axis, the electric field $\overline{E}$ in the in-plane switching mode is mainly directed along the x-direction and rotates the director in the plane parallel to the surface.

2.5.1 Director distribution

In real devices, the interdigitated electrodes of the in-plane switching mode are formed by two overlapping comb-shaped electrodes, as in Figure 2.10, both positioned on the bottom substrate. The dashed rect-

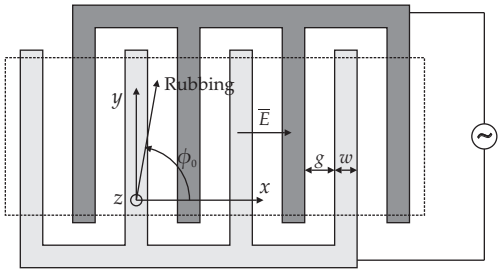

Figure 2.10: Electrode structure of the in-plane switching mode of liquid crystals on the bottom glass substrate.

angle which takes up most of the surface is the most important region. In good approximation the electrode configuration in the rectangle generates a periodic two-dimensional potential distribution, invariant along the y-axis. Therefore, also the obtained director distribution varies along the x- and z-direction.

Figure 2.11 shows the director and potential distribution for the in-plane switching mode in the xz-plane. The distribution is calculated for the liquid crystal material E7, using the three-dimensional simulation tool MonLCD. The full width of the electrodes w is 6 µm and the

distance g between them is 12 μm. The voltage applied over the electrodes is 10 V. The thickness of the simulated liquid crystal layer d is

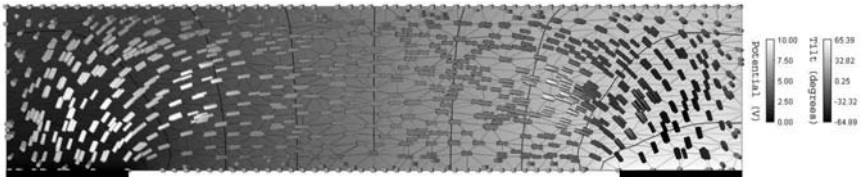

Figure 2.11: Two-dimensional calculation between the center of two neighboring electrodes of the director and potential distribution in the in-plane switching mode of liquid crystals (liquid crystal E7, $\phi_0 = 80°$, $\theta_0 = 1°$, $d = 4$ μm, $w = 6$ μm, $g = 12$ μm, applied voltage 10 V). Plotted area = 18×4 μm.

4 μm and the alignment has a pretwist ϕ_0 of 80° and a pretilt θ_0 of 1°. The plotted area covers the region between the center of two neighboring electrodes with horizontal dimension $g + w$ and vertical dimension d. Below the distribution, two black rectangles indicate the location of the electrodes. The background color indicates the potential distribution, the color and length of the cylinders indicate the director tilt and twist angle.

Between the two neighboring electrodes, the horizontal electric field has rotated the bulk director toward the x-direction. At the top and bottom surface, the director is strongly anchored along the rubbing direction. Over a thin surface layer the director is reoriented from the alignment direction toward the bulk orientation. Above the electrodes, the electric field has a strong perpendicular component. This yields an almost vertical orientation of the director above the electrodes.

2.5.2 One-dimensional approximation

The liquid crystal director in the in-plane switching mode is rotated in the plane parallel to the glass surfaces due to a horizontal electric field, generated by a pattern of interdigitated electrodes on one of the two substrates. The gap between neighboring electrodes is typically wider than the width of the electrodes and the thickness of the layer ($g > w \approx d$). The region between the electrodes is therefore the most significant for the transmission of the cell and a simple one-dimensional [34] approach is possible. It is valid if the spacing between the electrodes g is

large compared to the thickness of the liquid crystal layer d. When this is the case, a number of simplifications can be introduced:

- The electric field $\overline{E}$ is assumed to be homogeneous and parallel to the x-axis (Figure 2.9). The strength of the electric field E is related to the applied voltage by $E \approx V/g$.
- The small pretilt at the surface due to the rubbing process is neglected: $\theta_0 = 0$.
- The liquid crystal director at top and bottom is fixed at an angle ϕ_0 with the x-axis.

The two-dimensional director calculation in Figure 2.11 shows that these one-dimensional simplifications simplifications are valid in the region between the electrodes not too close to the electrode edges. In display applications, the electrodes are mostly opaque to avoid the adverse effects of light transmission through the regions above the electrodes. Therefore, the simple model gives also useful results.

The distribution of the director is derived by minimizing the total free energy of the liquid crystal layer. With the simplifications listed above, the free energy per unit surface is transformed to

$$F = \frac{1}{2} \int_0^d \left[k_{22} \left(\frac{\mathrm{d}\phi}{\mathrm{d}z} \right)^2 - \varepsilon_0 \, \Delta\varepsilon \, E^2 \, \cos^2 \phi \right] \mathrm{d}z, \tag{2.7}$$

with k_{22} the twist elastic constant and $\Delta\varepsilon$ the dielectric anisotropy of the liquid crystal material. This shows that the tilt angle is not affected by the electric field ($\theta(z) = \theta_0 = 0$) and only the twist angle ϕ is a function of the height z.

The equation is simplified by substituting the electric field E and the height z by the normalized parameters [38]

$$h = \frac{E}{E_c} \text{ with } E_c = \frac{\pi}{d} \sqrt{\frac{k_{22}}{|\Delta\varepsilon| \, \varepsilon_0}} \tag{2.8}$$

and

$$\zeta = \frac{z}{d}. \tag{2.9}$$

The critical electric field E_c [34,39] is the minimal strength of the electric field required for reorientation of the director in case of $\phi_0 = \pi/2$. This

is known as the Fréedericksz transition [3, 11]. From E_c the threshold voltage of the in-plane switching mode can be estimated

$$V_{th} = E_c\, g = \frac{\pi g}{d}\sqrt{\frac{k_{22}}{|\Delta\varepsilon|\,\varepsilon_0}}. \tag{2.10}$$

Substitution of (2.8) and (2.9) in (2.7) leads to a simplified expression for the free energy

$$F = \frac{k_{22}}{2d}\int_0^1 \left[\left(\frac{\mathrm{d}\phi}{\mathrm{d}\zeta}\right)^2 - \pi^2 h^2\,\cos^2\phi\right]\mathrm{d}\zeta \tag{2.11}$$

as a function of the normalized applied electric field h and the relative height ζ.

Solution of (2.11) for $\phi(\zeta)$ requires a variational approach. Substitution of the integrand in the Euler-Lagrange equation [40, 41] gives a nonlinear differential equation

$$\frac{\mathrm{d}^2\phi}{\mathrm{d}\zeta^2} - \pi^2 h^2 \sin\phi\cos\phi = 0. \tag{2.12}$$

with boundary conditions $\phi(0) = \phi(1) = \phi_0$. For the further calculations, this boundary value problem is solved numerically using the Matlab boundary value problem solver for ordinary differential equations [42].

The free energy in equation (2.7) together with the boundary conditions depends on 5 physical parameters: the liquid crystal twist elastic constant k_{22} and its dielectric anisotropy $\Delta\varepsilon$, the applied electric field E, the alignment direction ϕ_0 and the layer thickness d. After normalization, Euler-Lagrange leads to a differential system with only two independent variables: the normalized electric field h and the alignment direction ϕ_0. This means that all liquid crystals will exhibit the same director distribution in the in-plane switching mode. The choice of the liquid crystal material and the dimensions of the cell only result in a different scaling of the applied field.

Figure 2.12 shows the result of a calculation of the azimuthal angle ϕ of the director as a function of the height ζ for different values of the normalized field h and $\phi_0 = 85°$. Initially at $h = 0$ the twist ϕ is uniform throughout the whole layer ($\phi(\zeta) = \phi_0$). For increasing field strengths, the rotation toward the x-direction is initiated in the center. For higher values of h the azimuthal angle ϕ saturates at $\phi = 0$. A further increase

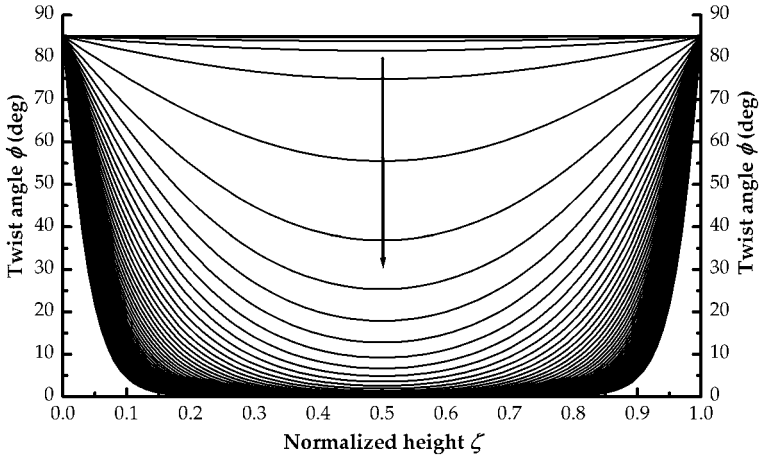

Figure 2.12: Twist angle ϕ as a function of the normalized height ζ for different values of the field $h = 0, 0.2, \ldots, 10$ and an alignment direction $\phi_0 = 85°$. The arrow indicates the direction in which the field increases.

of h yields a homogeneous layer in the middle with the director along the x-direction and two narrow layers at top and bottom with a rapid reorientation of the director, similar to the variation of the tilt angle in the twisted nematic and anti-parallel liquid crystal cell in Figure 2.8.

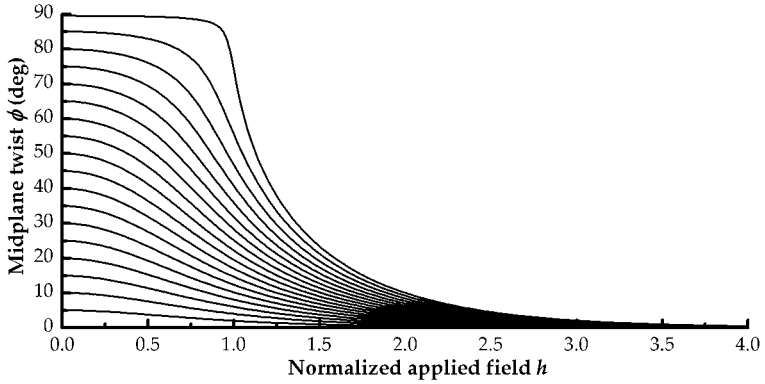

Figure 2.13: Midplane twist angle as a function of the normalized applied field h for different values of the alignment direction $\phi_0 = 5, 10, \ldots, 85, 89.5°$. The different curves can be distinguished by their value at h=0.

The midplane twist $\phi(1/2)$ is plotted as a function of the applied field h in Figure 2.13 for different directions of the alignment ϕ_0. For $\phi_0 = 90°$ the differential equation is not well conditioned, therefore the highest value of ϕ_0 is 89.5°.

It is clear that the alignment angle ϕ_0 has a profound influence on the switching behavior. Only for $\phi_0 \approx 90°$ a sharp threshold at $h = 1$ is obtained. For non-perpendicular alignment ($\phi_0 < 90°$), the rotation of the midplane director starts at small values of h. A smaller ϕ_0 yields a decrease of the threshold, but the transition to zero is less sharp.

In display applications a sharp threshold is usually preferred, but for $\phi_0 = 90°$ the rotation can occur toward the positive or the negative x-axis. This results in domains with opposite rotations. To avoid this in applications, the symmetry is broken by choosing a value of ϕ_0 close to 90°.The obtained smooth transition is called a quasi-threshold [11].

A side effect of decreasing ϕ_0 (not discussed here), is a faster response time of the liquid crystal [43, 44]. In display applications this is regarded as an advantage.

Chapter 3

Optical Transmission

Applications of liquid crystals involve almost always optics. For comparing optical experiments with simulational results, a good tool is required for calculating the optical transmission through a liquid crystal layer. Optical waves also involve electric fields, but the associated frequencies are much higher than those of the fields generated by the applied voltages. Therefore the dielectric constants, which arise from the electronic response of the molecules to the externally applied fields, are different. To make the distinction, the refractive index is usually given for optical waves instead of the dielectric constant. For non-magnetic materials, the dielectric constant ε and the refractive index n are related to each other by the relation $\varepsilon = n^2$.

In a uniaxial liquid crystal medium, the refractive index for an electric field oscillating in the plane perpendicular to the director is called the ordinary refractive index n_o, the electric field parallel to the director experiences the extra-ordinary refractive index n_e. The uniaxial anisotropy of the refractive index $\Delta n = n_e - n_o$ is called birefringence. Birefringence allows to manipulate the polarization of light propagating through the medium (see further). Table 3.1 gives the ordinary and extra-ordinary refractive index of the liquid crystals used in this work with the wavelength and temperature at which they are specified [4,10–12,32]. The value of Δn ranges from below 0.1 for lowly birefringent liquid crystals up to exceptional values of about 0.4 for highly birefringent liquid crystals.

Optical waves can also reorient the liquid crystal director in an analogue manner as the electrically applied fields [5, 45, 46]. In a display this can be neglected, since both the optical dielectric anisotropy $\Delta\varepsilon$

Table 3.1: The ordinary and extra-ordinary refractive index of the liquid crystals used in this work, with the temperature and wavelength at which they were determined

	E7	ZLI-4792	6CHBT	5CB	5PCH
n_e	1.75	1.5763	1.67	1.7063	1.604
n_o	1.5231	1.4792	1.52	1.5309	1.4875
Δn	0.2269	0.0971	0.15	0.1754	0.1165
T (°C)	20	20	22	25	30.3
λ (nm)	577	589		632.8	589

and the intensity of the optical fields are typically much lower than those used in the static case. Therefore the optical transmission can be calculated separately from the director calculations. Several algorithms are used in this work to calculate the propagation of an optical wave through a liquid crystal medium. The different methods are briefly explained in the next sections.

3.1 Polarization of light

Optical calculations are generally performed at a single wavelength and pure monochromatic light is by definition polarized. The electric field of a polarized plane wave propagating along the z-axis in an isotropic medium with refractive index n is a periodically varying vector in the xy-plane

$$\begin{cases} E_x = A_x \cos(\omega t - kz + \delta_x) \\ E_y = A_y \cos(\omega t - kz + \delta_y) \end{cases}, \tag{3.1}$$

describing an ellipse [47, 48]. $k = 2\pi n/\lambda$ is the wave number and $\omega = 2\pi c/\lambda$ the angular frequency. λ and c are the wavelength and the speed of light in vacuum.

A_x and A_y represent the amplitudes of the oscillations of the electric field along the x and y-axis as shown schematically in Figure 3.1. Usually these amplitudes are normalized with respect to some reference field and therefore dimensionless. The phases δ_x and δ_y determine the shape of the ellipse. For $\delta_y - \delta_x = m\pi$ with $m = 0, \pm 1, \pm 2, \ldots$ the electric field vector moves along a straight line and the polarization state of the light is said to be linear. For $\delta_y - \delta_x = m\pi + \pi/2$ the tip of the electric

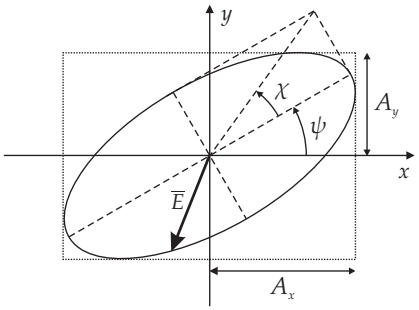

Figure 3.1: The polarization ellipse described in the xy-plane by the oscillating electric field vector of a plane wave propagating in the z-direction.

field vector rotates on a circle and the light is circularly polarized. For other values, the light is polarized elliptically.

If the tip of the electric field vector in a given plane, seen by an observer facing the approaching wave, moves in a clockwise direction the field is said to have right-handed polarization [48, 49]. A counterclockwise rotation corresponds with left-handed polarizations.

The rotation angle ψ and the ellipticity angle χ can be used to represent all polarizations on the Poincaré sphere [10, 48, 50]. On the sphere, the azimuthal angle 2ψ corresponds with twice the rotation ψ of the longest principle axis of the ellipse, while the inclination 2χ is a measure for its ellipticity. Linear polarizations are represented on the equator and circularly polarized light on the poles. The other points correspond to elliptically polarized light, right-handed in the upper half plane and left-handed in the lower. Each meridian represents a class of elliptic polarization states with identical orientation of the principle axes. Circles with a constant latitude correspond with polarization states which have an identical ellipticity, but different rotation angle. The Poincaré sphere is useful for the graphical representation of the change in the polarization state while propagating through a medium.

Without loss of information the electric field can also be written as a complex vector

$$\overline{E} = \begin{bmatrix} E_x \\ E_y \end{bmatrix} = \begin{bmatrix} A_x\, e^{i\delta_x} \\ A_y\, e^{i\delta_y} \end{bmatrix}, \tag{3.2}$$

known as the Jones vector. The representation of (3.1) can be retrieved by the operation $\mathrm{Re}[\overline{E}\, e^{i(\omega t - kz)}]$. The intensity of the wave is calculated

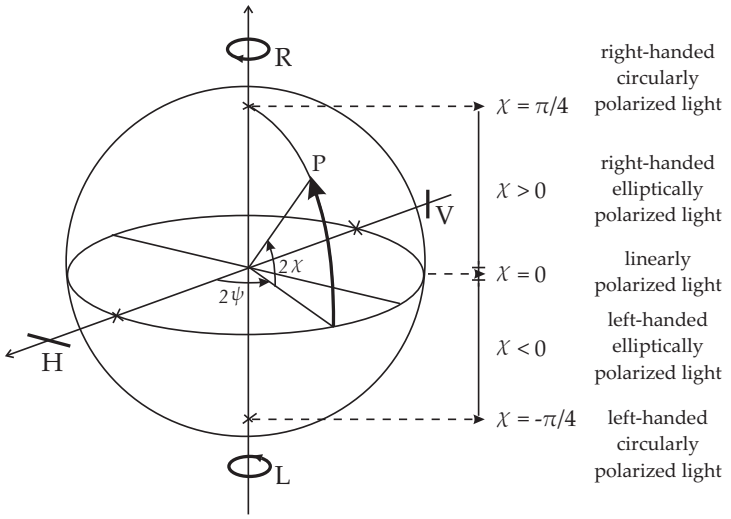

Figure 3.2: Representation of the polarization state of light on the Poincaré sphere.

as $I = |E_x|^2 + |E_y|^2$. The propagation of a plane wave through an isotropic medium with refractive index n can be expressed using the Jones vector as

$$\overline{E}(z) = \overline{E}\, e^{-i\frac{2\pi n}{\lambda}z}. \tag{3.3}$$

In isotropic media, the third component of the electric field E_z is zero, therefore it is omitted in the Jones vector notation. In anisotropic media this is no longer true, nevertheless the Jones vector can still be used. The two components E_x and E_y are sufficient to reconstruct the third component E_z.

3.2 Jones Matrix Method

Light propagation through anisotropic media is a complicated matter, but for normal incidence on a uniaxially birefringent layer, a simple 2×2 matrix formalism is available: the Jones Matrix Method [10,51,52].

The light wave incident from the isotropic medium can be divided in two independently propagation modes. The two modes, the ordinary and the extra-ordinary wave, are orthogonal linearly polarized plane waves propagating with a different speed in the same direction as the incident wave. The polarization of the ordinary wave is per-

pendicular to the direction of propagation and to the uniaxial axis and experiences a refractive index n_o. The extra-ordinary wave has a polarization perpendicular to the ordinary wave and lies in the plane determined by the uniaxial axis and the direction of propagation. The refractive index of the extra-ordinary wave is [10]

$$n_{\text{eff}} = \left[\frac{\sin^2 \theta}{n_o^2} + \frac{\cos^2 \theta}{n_e^2} \right]^{-1/2}, \tag{3.4}$$

with θ the tilt angle of the uniaxial axis as defined in Figure 2.2.

For a layer with the uniaxial axis located in the xz-plane, the Jones vector representations of the polarization for the extra-ordinary and the ordinary wave are parallel to respectively the x and y-axis. Therefore using (3.3), the transmission of an incident wave with arbitrary polarization is governed by

$$\begin{bmatrix} E_{x_1} \\ E_{y_1} \end{bmatrix} = \mathbf{W_0} \begin{bmatrix} E_{x_0} \\ E_{y_0} \end{bmatrix} = \begin{bmatrix} e^{-i\frac{2\pi n_{\text{eff}}}{\lambda} d} & 0 \\ 0 & e^{-i\frac{2\pi n_o}{\lambda} d} \end{bmatrix} \begin{bmatrix} E_{x_0} \\ E_{y_0} \end{bmatrix}, \tag{3.5}$$

with d the thickness of the layer. The retardation matrix $\mathbf{W_0}$ changes the polarization of the wave while propagating through the layer. The difference in optical path length $(n_{\text{eff}} - n_o)d$ between the two waves is called the retardation.

A quarter wave plate is a birefringent plate with the uniaxial axis parallel to the surface and a retardation of $\lambda/4$. Light with a linear polarization at an angle of 45° with the uniaxial axis is, after propagation through the layer, transformed into circularly polarized light. A half wave plate has a retardation of $\lambda/2$. After propagation through the half wave plate, the polarization ellipse of the normally incident plane wave is mirrored with respect to the uniaxial axis.

If the uniaxial axis is not in the xz-plane, a coordinate transformation is necessary to decompose the electric field into the ordinary and extra-ordinary mode of the layer. This transformation is simply a rotation of the coordinate axes around the z-axis

$$\begin{bmatrix} E_{x_1} \\ E_{y_1} \end{bmatrix} = \mathbf{R}\left(\phi\right) \begin{bmatrix} E_{x_0} \\ E_{y_0} \end{bmatrix} = \begin{bmatrix} \cos\phi & \sin\phi \\ -\sin\phi & \cos\phi \end{bmatrix} \begin{bmatrix} E_{x_0} \\ E_{y_0} \end{bmatrix}. \tag{3.6}$$

The combination of coordinate transformation, retardation and a return to the original coordinate system is called the Jones matrix

$$\begin{bmatrix} E_{x_1} \\ E_{y_1} \end{bmatrix} = \mathbf{J} \begin{bmatrix} E_{x_0} \\ E_{y_0} \end{bmatrix} = \mathbf{R}\left(-\phi\right) \mathbf{W_0} \mathbf{R}\left(\phi\right) \begin{bmatrix} E_{x_0} \\ E_{y_0} \end{bmatrix}. \tag{3.7}$$

If the layer is not homogeneous, but only varies along the surface normal, it can be approximated by a stack of thin homogeneous layers. The Jones matrices of the individual layers are then multiplied sequentially

$$\begin{bmatrix} E_{x_1} \\ E_{y_1} \end{bmatrix} = \mathbf{J}_n \, \mathbf{J}_{n-1} \, \ldots \, \mathbf{J}_1 \, \mathbf{J}_0 \begin{bmatrix} E_{x_0} \\ E_{y_0} \end{bmatrix}. \tag{3.8}$$

In one-dimensional liquid crystal layers, the uniaxial axis corresponds with the director and the Jones Matrix Method gives excellent results.

The Jones Matrix Method assumes there is no reflection of the light at either surface or internally and the light is totally transmitted through the layer. A better approximation is taking the transmission losses at the top and bottom interface of the layer into account. This gives a final Jones matrix [10, 53]

$$\begin{bmatrix} E_{x_1} \\ E_{y_1} \end{bmatrix} = t' \, \mathbf{J}_n \, \mathbf{J}_{n-1} \, \ldots \, \mathbf{J}_1 \, \mathbf{J}_0 \, t \begin{bmatrix} E_{x_0} \\ E_{y_0} \end{bmatrix}, \tag{3.9}$$

with t and t' the Fresnel transmission coefficients at the interfaces between the medium and air given by [49]

$$t = \frac{2}{1+n} \tag{3.10a}$$

$$t' = \frac{2n}{1+n}. \tag{3.10b}$$

t and t' represent respectively the air-to-medium and the medium-to-air interface. As refractive index n of the medium is chosen either the refractive index of the polarizers [54] or the ordinary refractive index of the liquid crystal [10, 53].

Although the Jones Matrix Method works solely with polarized light, calculations with unpolarized light can be approximated. The unpolarized light is then decomposed in two components with an orthogonal linear polarization and equal intensity. The transmission of the two linearly polarized components is calculated separately and the intensity of the results is summed afterward.

In case of oblique light incidence the calculation through a birefringent layer is more complicated and I refer to literature [10, 50]. Two different extensions for the Jones Matrix Method to oblique light incidence are available in literature [53–55]. I use the Extended Jones Matrix Method in the approximation of A. Lien [54] which does not make the small birefringence approximation. In this approximation

the difference in propagation direction between the ordinary and extra-ordinary wave due to double refraction [50] is neglected.

3.2.1 Polarizer

A polarizer, used in most optical setups involving birefringence, is a special type of anisotropic layer. In an ideal polarizer the ordinary wave propagates unmodified through the medium, whereas the extra-ordinary wave is absorbed. An arbitrarily polarized plane wave entering such a medium results in a linearly polarized wave exiting the medium. The Jones matrix of an ideal polarizer with the absorbing axis along the y-direction is represented by

$$\mathbf{P} = \begin{bmatrix} 1 & 0 \\ 0 & 0 \end{bmatrix}. \tag{3.11}$$

The orientation of a polarizer is typically indicated by its transmission axis, which corresponds with the polarization of the ordinary wave. In lots of devices a set of crossed polarizers is used, this implies two polarizers with orthogonal transmission axes. The first is referred to as the polarizer, the second as the analyzer. The azimuthal angle of the transmission axis of the polarizer and analyzer will be indicated with respectively ϕ_p and ϕ_a. For crossed polarizers applies that $\phi_a = \phi_p + 90°$.

In practice, polarizers can be made of dichroic materials. These materials absorb light polarized along the uniaxial axis more than in the plane perpendicular to it [49, 56, 57]. Typically the uniaxial axis of polarizers lies in the xy-plane. Absorbing materials are represented by a complex refractive index. For dichroic materials, the real part of the refractive index is isotropic while the imaginary part is anisotropic. An example is polaroid, with $n_\mathrm{o} = 1.887 - i\,2.23\ 10^{-5}$ and $n_\mathrm{e} = 1.887 - i\,1.5\ 10^{-3}$. For good polarizers the absorption of the extra-ordinary wave is several orders of magnitude larger than that of the ordinary wave.

3.2.2 Twisted nematic and anti-parallel rubbed

Figure 3.3 shows the electro-optic transmission characteristic of unpolarized light through the anti-parallel rubbed and the twisted nematic liquid crystal cells of Figure 2.8 for a wavelength λ of 600 nm. The cells are positioned between crossed polarizers with the transmission axes along the x and y-axis ($\phi_p = 0°$ and $\phi_a = 90°$).

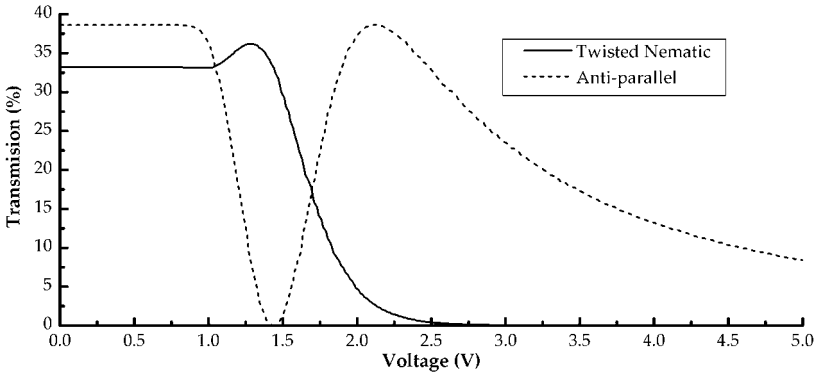

Figure 3.3: Electro-optic characteristic of an anti-parallel rubbed and a twisted nematic liquid crystal cell, calculated with the director distribution obtained in Figure 2.8 for a wavelength λ of 600 nm.

For the anti-parallel rubbed cell, the total retardation of the layer before applying a voltage was one and a half times the wavelength. Applying a voltage orients the director perpendicular to the surface, reducing the total retardation. For a retardation of λ and $\lambda/2$ the transmission reaches first 0 and then a maximum. Further increasing the applied voltage reduces the retardation even more and results in a monotone decline of the transmission toward zero.

In the twisted nematic cell for thick layers, the incident linear polarization follows roughly the rotation of the director and the light is transmitted through the analyzer. Applying a voltage destroys the smooth rotation of the director. The polarization will thus remain along the x-axis and is absorbed by the analyzer.

The transmission of the anti-parallel rubbed liquid crystal cell depends strongly on the considered wavelength. Because the twisted nematic cell is less sensitive to the wavelength, it is more widely used in displays than the anti-parallel rubbed liquid crystal device. The construction and working of a twisted nematic liquid crystal display is shown in Figure 3.4.

A light source at the back provides unpolarized light, which is polarized before entering the liquid crystal layer. Transparent ITO electrodes and alignment layers are deposited on both glass substrates to respectively apply the electric field and ensure the 90° twist of the director. Without any voltage applied, the linear polarization of the incident light follows the rotation of the director as shown on the left. If the

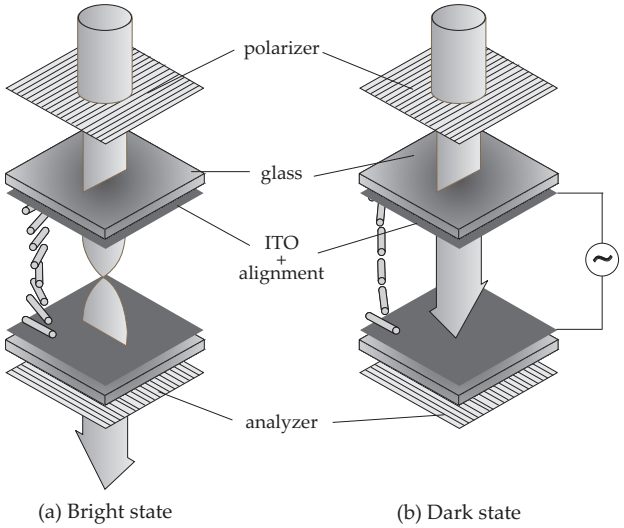

Figure 3.4: Bright state and dark state of a twisted nematic liquid crystal display.

applied electric field is strong enough, the director is oriented perpendicular to the surface and the light experiences an isotropic medium. The polarization is not changed and the light is absorbed by the analyzer, resulting in the dark state.

3.2.3 In-plane switching mode

Finally, Figure 3.5 shows an example of the electro-optic transmission characteristic in the in-plane switching mode for the different directions of the alignment ϕ_0 that were presented in Figure 2.13. The calculations are carried out with the Jones Matrix Method using a layer thickness d of 2.1 µm, a wavelength λ of 600 nm and the parameters of the liquid crystal E7. Since the distance between two neighboring electrodes of the in-plane switching device is not specified, the transmission is still plotted as a function of the normalized applied electric field h. The crossed polarizers at both sides of the layer are for each of the plots oriented parallel and perpendicular to the respective alignment ϕ_0.

The influence of the alignment on the threshold is visible in the transmission characteristics. With decreasing ϕ_0 the threshold voltage is reduced, but the increase of the transmission is less sharp. For ϕ_0 smaller than $\pi/4$ the curves increase monotonously, while for higher

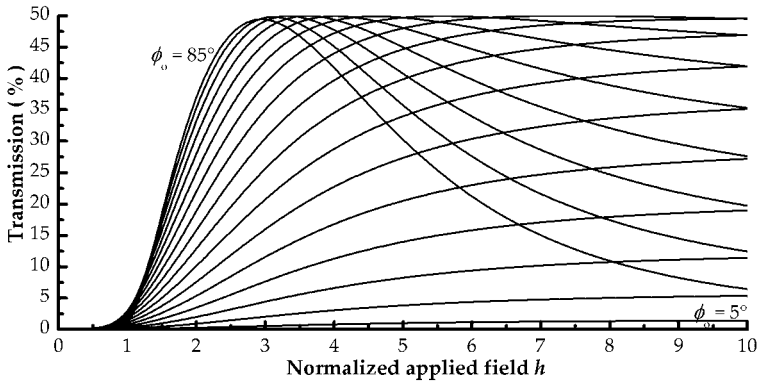

Figure 3.5: Electro-optic characteristic of a liquid crystal cell in the in-plane switching mode, calculated for different directions of the alignment ϕ_0 = 5, 10, ..., 85° and crossed polarizers with the transmission axes parallel and perpendicular to the respective anchorings ϕ_0.

values they reach a maximum. This maximum is shifted to weaker fields for higher values of ϕ_0. In order to keep the voltage range in applications low and achieve a maximum contrast, high values of ϕ_0 (above 45°) are preferred.

The optical characteristics of the in-plane switching mode are far better than those of the classic twisted nematic and anti-parallel configurations [36, 58–61]. In the off-state, the crossed polarizers absorb the light for all wavelengths, which yields a high contrast. Since the transmission in the dark state remains low at oblique viewing angles, the contrast decreases less as a function of the viewing angle. Moreover, gray scale inversion occurs less in the in-plane switching mode. Gray scale inversion happens when the transmission at an oblique viewing angle is no longer a monotonic increasing function of the applied voltage. Therefore the in-plane switching liquid crystal display is frequently used in flat-panel display applications.

3.3 Rigorous Coupled Wave Method

The problems handled in this work concern thin layers of liquid crystal with a lateral periodicity in one or two directions, therefore the Jones Matrix Method is not always useful. To calculate the optical transmission, general optical algorithms are available in literature based on

finite-difference time domain [62–64] or beam-propagation [46, 65–67]. But, for plane waves incident on a periodic dielectric medium, the Rigorous Coupled Wave Method (RCWM) [68–70] can also be used. It starts from an analytical solution for the transmission, using an infinite number of diffraction orders.

Suppose a plane wave with wave vector $\overline{k}_0 = k_{0x}\overline{1}_x + k_{0y}\overline{1}_y + k_{0z}\overline{1}_z$ is incident on an anisotropic dielectric layer invariant along the z-axis and with periods Λ_x and Λ_y along the x and y-direction. The dielectric tensor $\overline{\overline{\varepsilon}}(\overline{r})$, which describes the variation of the director through the volume is no longer a constant, therefore the Maxwell equations

$$\nabla \times \overline{E} + i\omega\mu_0\overline{H} = 0 \tag{3.12a}$$

$$\nabla \times \overline{H} - i\omega\varepsilon_0\,\overline{\overline{\varepsilon}}(\overline{r}) \cdot \overline{E} = 0 \tag{3.12b}$$

$$\nabla \cdot \left(\overline{\overline{\varepsilon}}(\overline{r}) \cdot \overline{E}\right) = 0 \tag{3.12c}$$

$$\nabla \cdot \overline{H} = 0 \tag{3.12d}$$

have to be solved for the electric and magnetic field $\overline{E}$ and $\overline{H}$, with $\mu_0 = 4\pi\ 10^{-7}$ H/m the magnetic permeability of vacuum.

Because of the lateral periodicity, the components of the dielectric tensor $\varepsilon_{\alpha\beta}$ $(\alpha, \beta = x, y, z)$ can be expanded in a Fourier series

$$\varepsilon_{\alpha\beta}(\overline{r}) = \sum_{lm} \varepsilon_{\alpha\beta,lm}\, e^{i\overline{K}_{lm}\cdot\overline{r}}. \tag{3.13}$$

The wave vector $\overline{K}_{lm} = lK_x\overline{1}_x + mK_y\overline{1}_y$ is related to the lateral periodicity by $K_x = 2\pi/\Lambda_x$ and $K_y = 2\pi/\Lambda_y$. The Bloch-Floquet theorem [4] states that in this case the electromagnetic fields inside and outside the grating can also be expressed as a Fourier expansion

$$\overline{E} = \sum_{lm} \overline{e}_{lm}(z)\, e^{-i\overline{k}_{lm}\cdot\overline{r}} \tag{3.14a}$$

$$\overline{H} = \sum_{lm} \overline{h}_{lm}(z)\, e^{-i\overline{k}_{lm}\cdot\overline{r}} \tag{3.14b}$$

with

$$\overline{e}_{lm} = e_{x,lm}\,\overline{1}_x + e_{y,lm}\,\overline{1}_y + e_{z,lm}\,\overline{1}_z \tag{3.15a}$$

$$\overline{h}_{lm} = h_{x,lm}\,\overline{1}_x + h_{y,lm}\,\overline{1}_y + h_{z,lm}\,\overline{1}_z \tag{3.15b}$$

and

$$\overline{k}_{lm} = (k_{0x} + lK_x)\,\overline{1}_x + (k_{0y} + mK_y)\,\overline{1}_y. \tag{3.16}$$

After substitution of (3.13) and (3.14) in (3.12), rearranging the components yields the differential equation

$$\frac{\mathrm{d}\overline{f}_t}{\mathrm{d}z} = i\mathbf{C}\,\overline{f}_t \tag{3.17}$$

$$\overline{f}_n = \mathbf{D}\,\overline{f}_t. \tag{3.18}$$

with the infinite column vectors

$$\overline{f}_t = \begin{bmatrix} e_{x,lm} \\ h_{y,lm} \\ e_{y,lm} \\ h_{x,lm} \end{bmatrix} \text{ and } \overline{f}_n = \begin{bmatrix} e_{z,lm} \\ h_{z,lm} \end{bmatrix} \tag{3.19}$$

containing all components of the electric and magnetic fields expressed in (3.14) and (3.15) with $l, m = -\infty, \ldots, \infty$. The indices t and n of the vectors $\overline{f}_t$ and $\overline{f}_n$ indicate respectively the tangential and normal components of the field components. For the expression of all the elements of the matrices $\mathbf{C}$ and $\mathbf{D}$, I refer to references [16,69,70]. The solution of the differential system (3.17) for the lateral components of the electric field, immediately yields the solution for the normal components using (3.18).

The Fourier expansion of the dielectric tensor and the fields contain an infinite number of orders. For calculations, the number of components in the Fourier series is truncated. Using m and n orders to express the electric and magnetic fields in the x and y-direction, the number of rows in the square matrix $\mathbf{C}$ is $4(2m+1)(2n+1)$. This means the size of the system matrix $\mathbf{C}$ increases quadratically with the number of diffraction orders taken into account, for example $m = n = 10$ yields a matrix of size 1764×1764.

The solution of the Maxwell equations is now reduced to an Eigenvalue problem. Using a matrix $\mathbf{M}$ containing the Eigenvectors of $\mathbf{C}$, equation (3.17) can be rewritten as

$$\frac{\mathrm{d}\overline{\psi}}{\mathrm{d}z} = i\mathbf{K}\,\overline{\psi} \tag{3.20}$$

with

$$\overline{f}_t = \mathbf{M}\,\overline{\psi}. \tag{3.21}$$

$\mathbf{K}$ is a diagonal matrix with the Eigenvalues K_n corresponding to the Eigenvectors in the columns of the matrix $\mathbf{M}$.

The differential equation for the different modes in $\overline{\psi}$ are now decoupled and can be solved as

$$\overline{\psi}(z) = \mathrm{diag}\left(e^{iK_n z}\right). \tag{3.22}$$

The relation between the lateral fields of the upper and lower surfaces can now be written as

$$\overline{f}_t(z = d) = \mathbf{M}\ \mathrm{diag}\left(e^{iK_n d}\right)\ \mathbf{M}^{-1}\ \overline{f}_t(z = 0). \tag{3.23}$$

In the isotropic areas above and below the layer, the Eigenmodes represent plane waves. Instead of using the field vector $\overline{f}_t$ to describe the fields in the regions above and below the grating, it is more convenient to work with a set of plane waves in order to obtain a clear propagation direction. The decomposition in Eigenmodes by the matrix $\mathbf{M_0}$ containing the Eigenvectors in the isotropic media, gives the plane waves in both isotropic regions:

$$\overline{\psi}_0 \ = \ \mathbf{M_0}^{-1}\ \overline{f}_t(z = 0) \quad \text{and} \quad \overline{\psi}_d \ = \ \mathbf{M_0}^{-1}\ \overline{f}_t(z = d). \tag{3.24}$$

Due to the continuity of the tangential fields at the interfaces, the relation between the plane waves in both isotropic regions is

$$\overline{\psi}_d = \mathbf{M_0}^{-1}\mathbf{M}\ \mathrm{diag}\left(e^{iK_n d}\right)\ \mathbf{M}^{-1}\mathbf{M_0}\ \overline{\psi}_0. \tag{3.25}$$

Depending on the direction of propagation (incident or reflected) in the isotropic regions, the plane waves in $\overline{\psi}_0$ and $\overline{\psi}_d$ can be separated into four different groups. In this way (3.25) is rewritten as:

$$\begin{bmatrix} \overline{\psi}_t \\ \overline{\psi}_b \end{bmatrix} = \begin{bmatrix} \mathbf{T}_{11} & \mathbf{T}_{12} \\ \mathbf{T}_{21} & \mathbf{T}_{22} \end{bmatrix} \begin{bmatrix} \overline{\psi}_i \\ \overline{\psi}_r \end{bmatrix}. \tag{3.26}$$

The subdivision distinguishes incident (i), reflected (r), transmitted (t) and backward incident (b) waves depending on the propagation direction of the respective plane waves. The different groups of modes are represented in Figure 3.6. The matrix in (3.26) is known as the transmission or **T**-matrix of the layer. The different block matrices $\mathbf{T}_{i,j}$ connect the modes at the top and bottom of the layer.

In a typical problem, the transmitted waves $\overline{\psi}_t$ and the reflected waves $\overline{\psi}_r$ need to be calculated as a function of the incident waves $\overline{\psi}_i$,

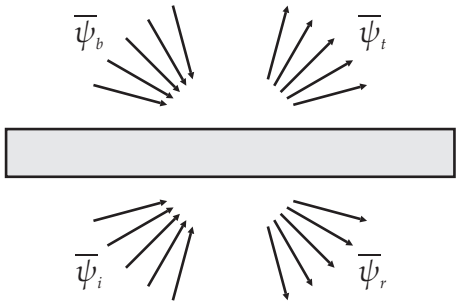

Figure 3.6: Schematical representation of the diffraction modes in the isotropic regions above and below the periodic layer. The modes are grouped in incident (i), reflected (r), transmitted (t) and backward incident (b) waves depending on their propagation direction.

while the backward incident waves $\overline{\psi}_b$ are zero. For the **T**-matrix formalism this means that part of the left and part of the right vector is unknown in equation (3.26). Therefore, forward and backward iteration is required for solving this system. In each step of the iteration, the backward wave $\overline{\psi}_b$ is reset to zero and the incident wave $\overline{\psi}_i$ is replaced by the original.

As in the Jones Matrix Method, a medium which varies along the z-direction can be approximated by a stack of several layers. The solutions of (3.23) must be multiplied sequentially, resulting in the **T**-matrix of the whole system.

The sequential multiplication of **T**-matrices can give rise to numerical problems [69, 71]. Some modes correspond with exponentially growing evanescent waves, which are very large at one side and very small at the other. The matrix components related to propagation of evanescent waves in one direction thus have exponentially growing elements and exponentially decreasing elements for the other direction. The multiplication of very large with very small numbers during the iteration, leads to numerical instability.

To avoid numerical instabilities, the scattering or **S**-matrix formalism should be used. The **S**-matrix propagation algorithm combines the submatrices of the **T**-matrices of the individual layers so that the exponentially growing functions never appear. The final **S**-matrix of the

whole stack looks as

$$\begin{bmatrix} \overline{\psi}_t \\ \overline{\psi}_r \end{bmatrix} = \begin{bmatrix} \mathbf{S}_{11} & \mathbf{S}_{12} \\ \mathbf{S}_{21} & \mathbf{S}_{22} \end{bmatrix} \begin{bmatrix} \overline{\psi}_i \\ \overline{\psi}_b \end{bmatrix}. \tag{3.27}$$

In the **S**-matrix formalism, the incident and backward incident modes are situated at the right-hand side, while the unknown transmitted and reflected waves are obtained as a result of the matrix multiplication.

The **S**-matrix propagation algorithm has been implemented by me together with Hans Desmet. The Eigenmodes in $\overline{\psi}$ have been normalized in such a way that the different propagating modes have an energy flux in the z-direction equal to one. This energy flux corresponds with the intensity of the z-component of the Poynting vector [68]

$$\overline{s} = \left| \overline{E} \times \overline{H} \right|. \tag{3.28}$$

In this way the intensity of each reflected or transmitted mode is immediately relative to the intensity of the incident wave. The algorithm will be demonstrated in the chapter on reconfigurable wave plates.

3.4 Reduced Grating Method

Because of the sometimes very large system matrices, the Rigorous Coupled Wave Method requires lots of calculation time and computer memory. It is therefore mainly useful for two-dimensional gratings or if only a limited number of diffraction orders are required. Therefore an approximation, the Reduced Grating Method (RGM) [72–74], was developed at the Politecnico di Torino during the European project MonLCD (G5RD-CT-2000-00115). I will not explain the whole algorithm but briefly give the main aspects.

The Reduced Grating Method is based on the **T**-matrix algorithm and starts from differential equation (3.17). The general solution of this equation is

$$\overline{f}_d = e^{i\mathbf{C}d}\, \overline{f}_0 \tag{3.29}$$

with

$$\overline{f}_0 = \overline{f}_t(z = 0) \text{ and } \overline{f}_d = \overline{f}_t(z = d). \tag{3.30}$$

This solution can be approximated as a Taylor series [40, 41]:

$$\overline{f}_d \approx \overline{f}_0 + i\mathbf{C}d\overline{f}_0 + \ldots + \frac{(i\mathbf{C}d)^{Q-1}}{(Q-1)!}\overline{f}_0. \tag{3.31}$$

In principle, this summation can be used to avoid the calculation of the Eigenvectors and Eigenvalues of the large matrices in the **T**-matrix algorithm. But, a direct calculation of the summation in (3.31) is numerically not efficient. It shows however that the solution is part of a Krylov subspace [75]:

$$\overline{f}_d \in K^{(Q)}\left(\mathbf{C}, \overline{f}_0\right) = \text{span}\left(\overline{f}_0,\ \mathbf{C}\overline{f}_0,\ \ldots,\ \mathbf{C}^{Q-1}\overline{f}_0\ \right). \tag{3.32}$$

The vectors in the basis of the Krylov subspace $K^{(Q)}(\mathbf{C}, \overline{f}_0)$ are strongly linear dependent. By using a Singular Value Decomposition [76] of the matrix $\mathbf{K}^Q = \left[\overline{f}_0\ \mathbf{C}\overline{f}_0\ \ldots\ \mathbf{C}^{Q-1}\overline{f}_0\right]$, it is possible to construct a smaller orthonormal basis for the Krylov subspace. Using the projection matrix $\mathbf{U}_P$ formed by the orthonormal basis vectors of the Krylov subspace, the dimension of the system matrix in (3.17) can be reduced to a size $P < Q \ll 4(2m+1)(2n+1)$ [73]:

$$\frac{\mathrm{d}\overline{f}_P}{\mathrm{d}z} \ = \ i\,\mathbf{U}_P^H \mathbf{C}\mathbf{U}_P\,\overline{f}_P \ = \ i\,\mathbf{C}_P\,\overline{f}_P \tag{3.33}$$

with

$$\overline{f}_P = \mathbf{U}_P\,\overline{f}_t. \tag{3.34}$$

Typical values for the size P of the matrix $\mathbf{C}_P$ are 4×4 to 6×6. Therefore, the transmission matrix is easily calculated as

$$\overline{f}_d \ = \ \mathbf{U}_P\, e^{i\,\mathbf{C}_P\, d}\ \mathbf{U}_P^H\ \ \overline{f}_0. \tag{3.35}$$

The strength of the Reduced Grating Method is that building the matrix $\mathbf{K}^Q$ does not require an explicit calculation of the large system matrix **C**, but is calculated directly from (3.13) and (3.16). This gives a serious reduction of the computer memory needed and allows a higher number of diffraction orders taken into account with an increased calculation speed compared to the Rigorous Coupled Wave Method. Drawback is however that the Reduced Grating Method is based on the **T**-matrix formalism and thus suffers from the same numerical instability. Unfortunately, there is no **S**-matrix equivalent of the Reduced Grating Method.

The version of the Reduced Grating Method available in our lab handles two-dimensional dielectric layers. It allows to use a large number of diffraction orders, without the need of excessive computer memory.

3.5 Simplified transmission model

General methods as described in sections 3.3 and 3.4 give good results, but are time consuming. Therefore a simplified transmission model is proposed which works for thin liquid crystal layers with slow lateral variations of the director.

3.5.1 Transmission model

The model starts from a two-dimensional liquid crystal medium, invariable along the y-axis with the director orientation given on a regular rectangular grid in the xz-plane. The grid must be sufficiently fine in order to assume that the liquid crystal properties are homogeneous inside each grid box. The goal is to calculate the propagation of an obliquely incident plane wave through the liquid crystal layer. The wave vector $\overline{k}_0$ of the incident wave in air, is determined by the inclination angle ϑ_0 (the angle between $\overline{k}_0$ and the z-direction) and the azimuthal angle φ_0 (the angle between the x-axis and the projection of $\overline{k}_0$ on the xy-plane) as indicated in Figure 3.7. (Note that this is different than the definition of the director tilt angle in Figure 2.2)

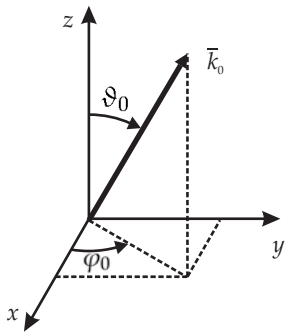

Figure 3.7: Definition of the inclination angle ϑ_0 and the azimuthal angle φ_0 of the wave vector $\overline{k}_0$ of an incident plane wave.

In two-dimensionally varying media, incident plane waves are diffracted. If the thickness of the layer measured along the surface normal is small compared to the lateral dimensions and not much larger than the wavelength λ of the light, the impact of diffraction is small. When the variation of the liquid crystal director inside the thin layer is relatively slow, the Extended Jones Matrix Method may be used as

an approximation [77]. In this case, the propagation through the liquid crystal is calculated only taking into account birefringence and neglecting diffraction inside the layer, as illustrated in Figure 3.8. The plane of incidence in Figure 3.8, which contains the wave vectors $\overline{k}$ and $\overline{k}_0$, coincides with the xz-plane ($\varphi_0 = 0°$), but in general φ_0 can vary freely.

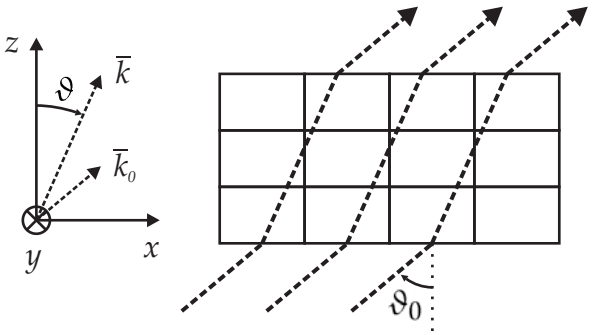

Figure 3.8: Basic principle of the simplified algorithm based on the Extended Jones Matrix Method for the optical transmission model through thin liquid crystal layers. A plane wave in air, represented by a number of parallel rays, is obliquely incident with inclination angle θ_0 on a liquid crystal medium of which the director distribution is given on a rectangular regular mesh.

The plane wave incident on the two-dimensional medium is handled with a technique similar to ray tracing. The plane wave is simulated as a large number of incident rays, shifted along the x-direction and parallel to $\overline{k}_0$. Refraction at the bottom and top surface of the liquid crystal layer is taken into account by changing the propagation direction to $\overline{k}$ according to Snell's refraction law. The ordinary refractive index n_o of the liquid crystal is used as an approximation for the liquid crystal medium to apply Snell's refraction law. This is in accordance with the the direction in which the transmission is calculated in the Extended Jones Matrix formulation by A. Lien [54]. From each of the grid boxes at the bottom of the layer, a ray propagates toward the other side. For each rectangle in which a ray passes on its way, a Jones matrix is calculated taking into account the length of the path that the ray makes through this box. By doing so, the variation of the liquid crystal in the x-direction is neglected. The propagation matrices are calculated according to the formula for the Extended Jones Matrix Method presented by A. Lien [54].

The result is a series of Jones vectors providing the electric field variation at the top surface. The intensity of the electric field provides the near field transmission which is roughly the observed intensity with a microscope. Combining the complex Jones vector representation of the electric field and diffraction theory gives an approximation of the far field. At a large distance of the surface Fraunhofer diffraction [50] can be used, which corresponds with the Fourier transform of the field at the surface [49]. For a periodically modulated wave at the surface, this can be evaluated quickly using the Fast Fourier Transform [40].

3.5.2 Simulations

The algorithm is illustrated using the in-plane switching mode of liquid crystals. The simulated liquid crystal layer has a thickness d of 4 μm, the width of the electrodes w is 6 μm and the gap g between them is 18 μm. The rubbed alignment layers keep the surface director at a pretwist ϕ_0 of 80° and a pretilt θ_0 of 1°. The liquid crystal material is ZLI-4792. The director simulations for the liquid crystal medium were performed using the software package 2dimMOS [31], commercial software for two-dimensional director calculations. Crossed polarizers are positioned at top and bottom, respectively parallel and perpendicular to the alignment ($\phi_p = \phi_0$ and $\phi_a = \phi_0 + 90°$).

First, the transmission of an obliquely incident unpolarized plane wave is examined. The field intensity near the top surface is investigated along the x-axis, after passing the analyzer. Figure 3.9 shows the variation of the intensity of the transmission at the top surface relative to the intensity of the incident unpolarized plane wave when voltages of 5, 10, 15, 20 and 25 V are applied. The plotted region starts and ends in the middle of two neighboring electrodes.

The incident plane wave is monochromatic with a wavelength λ of 632.8 nm and the incident wave vector $\overline{k}_0$ has an inclination angle $\vartheta_0 = 25°$ in air and azimuthal angle $\varphi_0 = 25°$ with the x-axis. The results of the Extended Jones Matrix Method (EJMM) are verified by comparison with those of the Reduced Grating Method (RGM). The variation of the intensity at $z = d$ for the Reduced Grating Method is calculated with the Poynting vector (3.28) using the near fields calculated with (3.14).

The graph shows that the overall correspondence between the Jones matrix algorithm and the Reduced Grating Method is good. At 5 V, the applied voltage is just above the threshold voltage and only above the

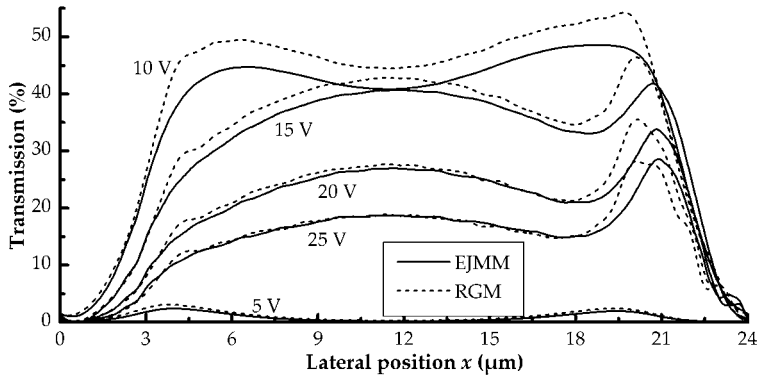

Figure 3.9: Simulated transmission at the top surface of the liquid crystal layer in the in-plane switching mode after passing the analyzer for an unpolarized, obliquely incident plane wave, between the center of two neighboring electrodes as a function of the lateral position for different applied voltages. (liquid crystal ZLI4792, $\phi_0 = 80°$, $\theta_0 = 1°$, $d = 4$ μm, $w = 6$ μm, $g = 18$ μm, $\vartheta_0 = \varphi_0 = 25°$, $\phi_p = \phi_0$, $\phi_a = \phi_0 + 90°$)

edges of the electrodes the electric field is strong enough to act on the director. The transmission reaches a maximum at 10 V and decreases for higher voltages. Between the two electrodes, the director is almost uniform and the correspondence between both methods is very similar. At higher voltages the director variations above the electrodes increase and diffraction within the liquid crystal becomes important. This explains the deviation at the right-hand side of the graph for higher voltages.

In display applications, the variation of the transmitted electric field at the top surface is interesting, however more important is the transmission seen by the human eye at a distance from the display. This far field can be calculated as the diffracted field of the electric field at the surface. The liquid crystal layer in the in-plane switching mode as described above is periodical, with a period $\Lambda_x = g + w = 24$ μm. The periodicity yields distinct diffraction orders and the Fraunhofer approximation of diffraction [50] can be implemented by a complex fast Fourier transform of the electric field components at the surface.

Figure 3.10 shows the intensity of the diffraction orders for the Jones matrix algorithm and the Reduced Grating Method for applied voltages of 5, 15 and 25 V. The graph shows a very good resemblance for the central diffraction order (order 0), which propagates along the di-

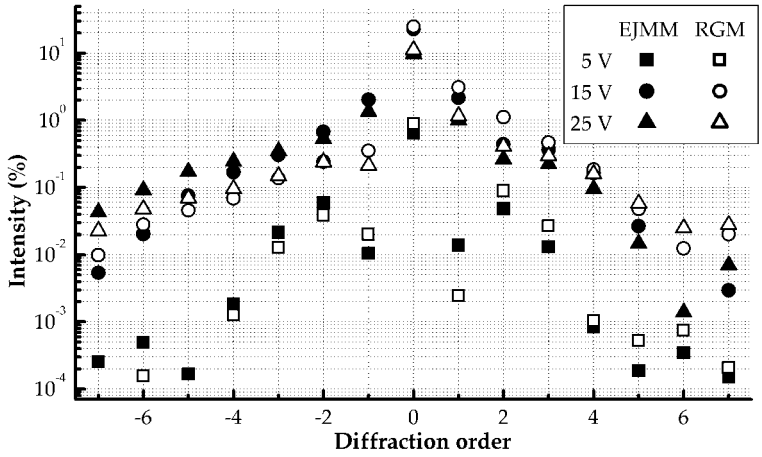

Figure 3.10: Intensity of the diffraction orders in the Fraunhofer diffraction pattern of an unpolarized plane wave, obliquely incident on a liquid crystal in the in-plane switching mode for different applied voltages. (liquid crystal ZLI4792, $\phi_0 = 80°$, $\theta_0 = 1°$, $d = 4$ µm, $w = 6$ µm, $g = 18$ µm, $\vartheta_0 = \varphi_0 = 25°$, $\phi_p = \phi_0$, $\phi_a = \phi_0 + 90°$)

rection $\overline{k}_0$ and corresponds with the average of the complex field at the top surface of the liquid crystal.

The intensity of the other orders does not correspond so well. This difference is caused by the phase of the electric field at the top surface. Figure 3.9 shows that the Jones matrix algorithm is accurate in predicting the amplitude of the electric field. However the phase variation of the electric field components δ_x and δ_y before propagating through the analyzer, as shown in Figure 3.11, is less good. To create this graph, the linear increasing phase $\delta_{obl} = x\, k_{0x}$ due to oblique incidence was omitted in both results. By doing so, the phase function becomes periodical. Even for quite low voltages as in Figure 3.11(a), there is a deviation in the phase variation and for increasing voltage this becomes worse. For the analysis of this imprecision, the phase of the electric field is divided in two parts, an absolute phase variation and a phase difference.

The phase difference $\delta_{dif} = \delta_y - \delta_x$ originates from the retardation between the ordinary and extra-ordinary mode. The retardation is responsible for the change of the polarization of the plane wave and is directly related to the transmission of a liquid crystal cell between crossed polarizers. Although the individual phases of δ_x and δ_y differ at high voltages, the phase difference δ_{dif} corresponds very well. This

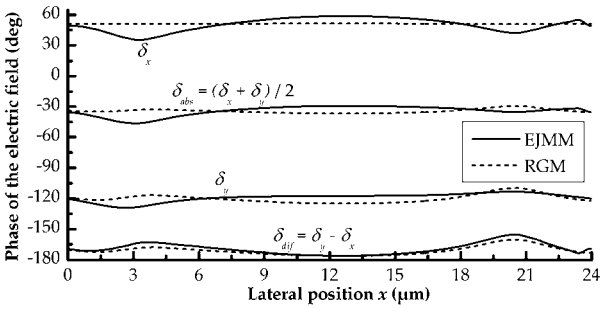

(a) Applied voltage 5 V

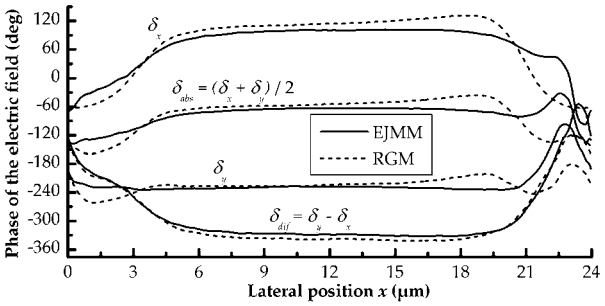

(b) Applied voltage 25 V

Figure 3.11: Variation of the phase of the electric field components δ_x and δ_y, the phase difference δ_{dif} and the absolute phase δ_{abs} before propagation through the analyzer at the top surface of the liquid crystal layer of the calculation in Figure 3.9 for an applied voltage of (a) 5 V and (b) 25 V.

agrees with the fact that birefringence is correctly taken into account by the Jones matrix algorithm and explains the good match between both methods in Figure 3.11.

The absolute phase variation of the electric field δ_{abs} is related to the propagation distance in the medium and is approximated by the average of δ_x and δ_y. Without lateral variations in the medium, the δ_{abs} is identical for all rays that propagate through the medium. On the right-hand side of Figures 3.11(a) and 3.11(b), larger deviations of δ_{abs} are visible between both methods due to the rapid director variations of the director. Focusing of the wave is mainly the result of this deviation.

Although the liquid crystal is nearly mirror symmetric toward the center between the electrodes, the transmission curves in Figure 3.9

show an asymmetry. Also the differences of the absolute phase δ_{abs} are mainly present on the right-hand side. The asymmetry in the curves is due to the oblique incidence of the light ($\vartheta_0 = \varphi_0 = 25°$). Because of the 1° pretilt of the molecules, a small asymmetry remains present for perpendicular light incidence. Therefore, a quantitative way to evaluate the lateral variations is necessary. In fact, not the variation of the liquid crystal director in the layer is important, but the variation of the experienced refractive index. For liquid crystals this is complex since the material is birefringent and a superposition of the ordinary and the extra-ordinary wave is made. The first one feels the ordinary refractive index n_o of the liquid crystal, which is constant. The extra-ordinary wave feels an effective refractive index n_{eff}, which depends on the angle between the direction of propagation $\overline{k}$ and the local orientation of the liquid crystal director.

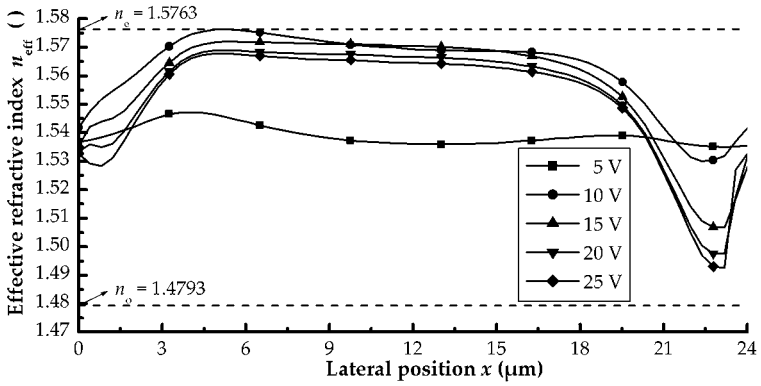

Figure 3.12: Variation of the effective refractive index of the extra-ordinary wave for the director in the midplane of the liquid crystal layer and propagation direction $\overline{k}$ used in the calculations of Figures 3.9 and 3.11.

Figure 3.12 represents the effective refractive index corresponding with the propagation direction $\overline{k}$ for the director in the midplane of the liquid crystal layer. For perpendicular incidence the curves are symmetric, but due to oblique incidence the variations of the refractive index are much larger at the right-hand side and there the largest differences in the transmission and the phase are expected.

3.5.3 Experiments

At the time of developing the algorithm, a detailed measurements using obliquely incident light was not possible. However, it was possible to reliably measure the intensity of the diffraction orders after propagation through the analyzer for normal light incidence. This measurement gives an idea of the accuracy of the calculations and the influence of the diffraction.

A first observation in these experiments is the diffraction occurring when no voltage is applied. The director pattern is then considered to be homogeneous with the director parallel to the rubbing direction. Since there is no lateral variation, the observed diffraction was rather unexpected. The occurring diffraction is due to the interdigitated parallel electrodes, which induce a periodical phase modulation. To obtain a good comparison with the measurements, the ITO structure should be included in the model by adding an additional layer at the bottom with either isotropic ITO for the electrodes or liquid crystal material parallel to the alignment direction for the regions in between.

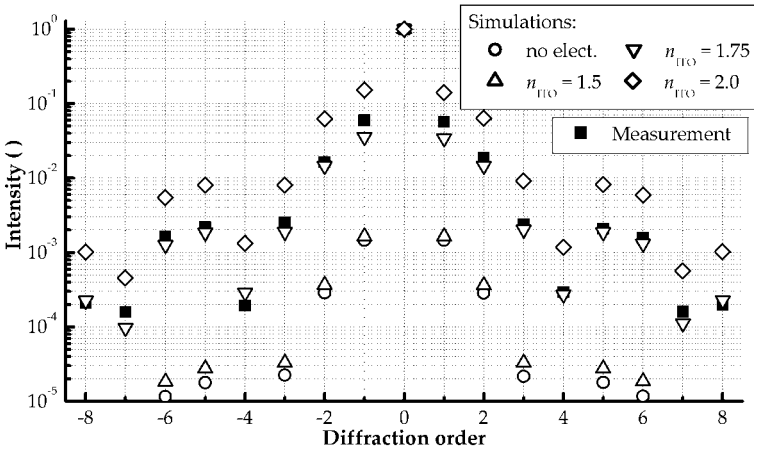

Figure 3.13: Measured intensity of the transmitted diffraction orders after propagation through the analyzer together with the simulated intensity for different values of the refractive index of the ITO electrodes (IPS-parameters : d = 4 μm, w = 18 μm, g = 6 μm, applied voltage 3 V).

According to the specifications of the manufacturer the thickness of the ITO is about 277 nm. The refractive index of the ITO is subject to deposition parameters. By choosing an appropriate value for the

refractive index, it is possible to obtain a good resemblance between the simulated intensity and the measured one as shown in Figure 3.13. The best fit is found for a refractive index of 1.77, which is within the range of values found in literature. The intensities in the graph are scaled by setting the intensity of the zero order equal to unity for every series.

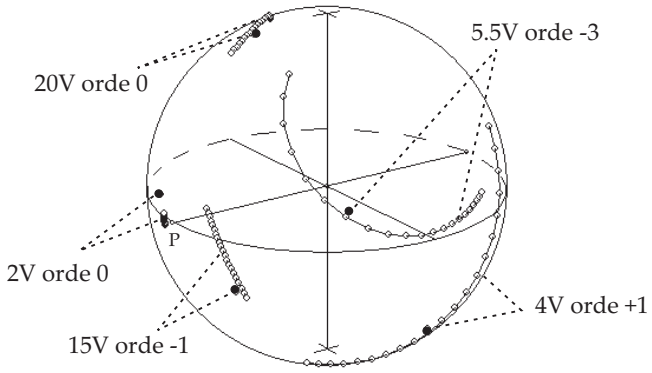

Figure 3.14: Measured and simulated polarization states (full and empty circles respectively) of the diffraction orders before propagation through the analyzer, represented on the Poincaré sphere. For the calculated polarization states, the thickness of the ITO electrodes is varied from 0 to 500 nm. (IPS-parameters : d = 4 μm, w = 18 μm, g = 6 μm)

The electrodes do not only influence the intensity of the diffraction orders, but also their polarization state before propagating through the analyzer. Figure 3.14 shows a few examples of the measured polarization states when the analyzer is omitted in the setup, together with the simulated polarizations for an electrode thickness varying from 0 to 500 nm, represented on the Poincaré sphere. The agreement between simulation and measurement is not perfect, which is expected since the simulated phase variation is not that accurate and this influences the polarization state. Nevertheless, for 3 of the 5 plotted diffraction orders, the best fit with the measured polarization state is close to the actual electrodes thickness of 277 nm. More important, the result illustrates that the polarization state of the diffraction orders is heavily influenced by the electrode thickness. If the electrode thickness is further increased, the calculated polarization states will describe circles on the Poincaré sphere.

To keep the influence of the electrodes on the in-plane switching

mode as small as possible, the electrodes should be as thin as possible with a refractive index close to the ordinary refractive index of the used liquid crystal. This is important for the application of the in-plane switching mode as a grating. Since the intensity of the diffraction orders is at least one order lower than that of order 0, the influence of the electrodes on the optical transmission in display applications is negligible.

To avoid the adverse effects on the contrast of transmission through the electrodes at oblique viewing angles, the electrodes are sometimes made of an opaque metal [60]. Also in experiments where one is only interested in the region between the electrodes, metals are often used to produce the electrodes. In this way, the gap easily observable with a microscope.

The discussion and results of the transmission model were presented at the International Display Workshop/Asia Display 2001 (Nagoya, Japan) [78] and the International Topical Meeting on Optics of Liquid Crystals 2003 (Aussois, France) [79]. A full paper describing the simplified optical transmission model was published in the SCI Journal *Molecular Crystals & Liquid Crystals* [80].

A similar ray-tracing technique has been demonstrated in [81] to calculate iso-transmission and iso-contrast plots of an electrically-induced optical compensation display mode, but in that reference the limitations of the method have not been discussed.

The simplified two-dimensional optical algorithm as explained above can easily be extended to three-dimensional anisotropic media, as will be demonstrated in the chapter on reconfigurable wave plates. Although calculations for oblique light incidence are very useful, only normal light incidence will be used in the next chapters.

Chapter 4

Surface Anchoring

The anchoring of the liquid crystal molecules at the surface is intended to control the alignment of the surface director. Therefore it is an important aspect when designing liquid crystal devices.

In this chapter, the phenomena related to anchoring are studied in more detail. As a preparation to the new device discussed in Chapter 5, a number of experiments on weak anchoring are described.

4.1 Weak and strong anchoring

Classic alignment layers hold the liquid crystal director at their surface tightly in a fixed orientation. This is referred to as strong anchoring and is widely used in lots of liquid crystal applications.

The nature of the anchoring process is the anisotropy of the surface in contact with the liquid crystal. The origin of this anisotropy can be very different. Some surfaces like crystalline solids or polymers have an inherent anisotropy, which results in molecular interaction between the liquid crystal and the surface. But also a surface topology like parallel grooves in an isotropic material can align the director.

Alignment layers are manufactured by a large variety of processes: rubbing [16, 82], photoalignment [13–15], structured surfaces [83–86], surfactants [87, 88], ... For a rubbed surface, the azimuth and pretilt of the surface director are determined by the rubbing parameters. For other processes like photo-alignment, the orientation of the surface director is not so strict. With a strong electric field or a torque on the liquid crystal director, the surface director can turn away from the pref-

erential direction. Therefore, the principle of weak anchoring is introduced.

Weak anchoring is a generic term for all situations where the surface director can be altered. Such surfaces exhibit one or more stable orientations of the surface director, but electric or mechanical torques can change the orientation of the surface director. In practice different surface conditions are possible:

- Monostable surfaces: a single stable orientation of the surface director [16, 89]
- Bistable or multistable surfaces: two or more stable orientations of the surface director [86, 90, 91]
- Degenerated anchoring surfaces: the director prefers to be oriented in a certain plane or on a cone [3, 92, 93]
- Surface gliding: by application of a strong temporary electric field and/or heating of the liquid crystal cell, the stable direction of the surface director can be modified permanently [13, 86, 94, 95].

The surface desired in the next chapter is a planar azimuthally degenerated anchoring surface. At such a surface, also referred to as a slippery surface, the director has a preference to lie in the plane parallel to the substrate, but can rotate freely in the azimuthal direction.

The applications of weak anchoring are situated in the field of multistable nematic liquid crystal devices, electrically controllable anchoring and reduction of the threshold voltage and power consumption of liquid crystal devices. The behavior of the surface anchoring is determined by the surface material, treatment or structure.

4.2 Modeling of weak anchoring

Modeling of liquid crystals involves minimizing the free energy of the system. For strong anchoring, the free energy has two parts: the Oseen-Frank distortion energy f_d due to the variation of the liquid crystal director in space and the electric energy f_e from the interaction of the electric field with the local director. The anchoring at the surface is handled by a Dirichlet boundary condition of the director $\overline{n}$.

For weak anchoring, the surface anchoring energy f_s is introduced to replace the Dirichlet boundary condition. On monostable surfaces,

the preferential direction is specified by the easy direction $\overline{\epsilon}$, with azimuthal angle ϕ_0 and tilt angle θ_0. This yields a free energy

$$F = \int_V \left[f_d\left(\overline{n}\right) - f_e\left(\overline{n}, \overline{E}\right) \right] \, dV + \int_S f_s\left(\overline{n}, \overline{\epsilon}\right) \, dS, \tag{4.1}$$

with an energy penalty f_s if the surface director $\overline{n}$ deviates from $\overline{\epsilon}$.

4.2.1 Expressions for the anchoring energy f_s

In general, f_s can be a complicated function of the surface director $\overline{n}$ and the easy direction $\overline{\epsilon}$. Many expressions have been introduced for f_s. All these expressions are approximations useful for numerical calculations and comparison with experiments, but valid only under certain conditions. In the following paragraphs, a number of popular expressions for f_s are given for monostable anchoring around the easy direction $\overline{\epsilon}$ specified by the pretwist ϕ_0 and the pretilt θ_0.

A. Rapini and M. Papoular [96] were the first to introduce a trigonometric expression of the anchoring energy for homeotropic alignment

$$f_s = \frac{W}{2} \sin^2(\theta), \tag{4.2}$$

with θ the director tilt angle. This expression yields an energy minimum if the surface director is perpendicular to the surface ($\theta = \theta_0 = \pi/2$).

Quite rapidly generalizations like

$$f_s = \frac{W}{2} \sin^2(\theta - \theta_0), \tag{4.3}$$

were introduced [97], which describe a tilted anchoring with pretilt θ_0. However in the expression, there is no assumption about the surface twist angle ϕ.

In general, both the surface twist and tilt angle can be altered by an applied torque. Therefore, the concept of polar and azimuthal anchoring must be introduced. Polar anchoring involves deviations of the surface tilt angle θ from the pretilt θ_0, while azimuthal anchoring is related to deviations of the surface twist angle ϕ from the azimuthal alignment ϕ_0. For that reason,

$$f_s = \frac{1}{2} \left[W_p \sin^2(\theta - \theta_0) + W_a \sin^2(\phi - \phi_0) \right] \tag{4.4}$$

is widely used in literature [11, 33, 38, 86, 98] as a generalization of the original Rapini-Papoular expression. The weight coefficients W_p and W_a are related to respectively the polar and the azimuthal anchoring around the easy direction (θ_0, ϕ_0).

For small variations of the director $\overline{n}$, close to the easy direction $\overline{e}$, this expression gives good results. For large deviations however, the expression shows some characteristics which are incompatible with the basic assumptions about the anchoring energy f_s [97, 99]:

- The director orientations $\overline{n}$ and $-\overline{n}$ which are physically equivalent, should yield the same energy contribution.
- Given the easy direction $\overline{e}$, there are two non-equivalent minimal energy solutions for the anchoring energy (θ_0, ϕ_0) and $(\theta_0, \phi_0 + \pi)$, which is inconsistent with the intended single easy direction.
- The anchoring is not properly defined along the surface normal, because ϕ is arbitrary.

Although the separation of the polar and azimuthal anchoring in equation (4.4) simplifies the mathematical analysis, polar and azimuthal anchoring are not entirely independent. Therefore a separation of the anchoring energy f_s in two terms, one dependent only on the twist angle ϕ, the other only on the tilt angle θ is not possible and weak anchoring should be modeled by a more complete form for the anchoring energy.

A first expression in which changes of the surface twist and tilt angle are included in the anchoring energy is [97]

$$f_s = -\frac{W}{2} \left(\overline{e} \cdot \overline{n}\right)^2 . \tag{4.5}$$

The expression gives a unique value of the anchoring energy f_s for all orientations of $\overline{n}$ and yields a single energy minimum for the director $\overline{n}$ parallel to the easy direction $\overline{e}$. However, the possibility for a difference in anchoring strength between polar and azimuthal anchoring lacks in this expression. Normally, the polar and azimuthal anchoring strength are different.

Therefore, Beica et al. [100] proposed

$$f_s = \frac{1}{2} \left[W_1 \left(\overline{n} \cdot \overline{n}_1\right)^2 + W_2 \left(\overline{n} \cdot \overline{n}_2\right)^2 \right] \tag{4.6}$$

with

$$\overline{n}_1 = \frac{\overline{\epsilon} \times \overline{1}_z}{\left|\overline{\epsilon} \times \overline{1}_z\right|} \text{ and } \overline{n}_2 = \overline{\epsilon} \times \overline{n}_1. \tag{4.7}$$

Equation (4.6) describes a symmetrical anchoring around the easy direction $\overline{\epsilon}$ which resolves the shortcomings of (4.4) and (4.5).

Although useful in most situations, a further improvement is still possible. First of all, homeotropic alignment is not included in the formulation since $\overline{n}_1$ and $\overline{n}_2$ are not defined for homeotropic alignment ($\overline{\epsilon} = \overline{1}_z$). Secondly, recent simulations [99, 101] have shown that asymmetrically modulated surfaces may exhibit a weak azimuthal anchoring which is azimuthally not symmetric around the easy direction $\overline{\epsilon}$.

Therefore, Zhao et al. [99, 102] introduced a new expression for the anchoring energy. The expression calculates a second order, spherical harmonic approximation of an arbitrary surface anchoring energy f_s, using the easy direction $\overline{\epsilon}$ as the polar axis. Based on the centrosymmetry of the anchoring energy $f_s(\overline{n}) = f_s(-\overline{n})$ and assuming two energy minima along $\overline{\epsilon}$ and $-\overline{\epsilon}$, the second order spherical harmonic approximation can be rewritten as

$$f_s = \frac{1}{2}\left[W_\xi (\overline{n} \cdot \overline{\xi})^2 + W_\eta (\overline{n} \cdot \overline{\eta})^2 \right]. \tag{4.8}$$

The vectors $\overline{\xi}$, $\overline{\eta}$ and $\overline{\epsilon}$ give the three principle axes of anchoring and form an orthonormal vector triplet. The anchoring strengths W_ξ and W_η give the cost for a deviation of the surface director away from the easy axis in the direction of $\overline{\xi}$ and $\overline{\eta}$. The anchoring energy is centrosymmetric, only yields a minimum along the equivalent directions $\overline{\epsilon}$ and $-\overline{\epsilon}$ and is unambiguously defined along all orientations of $\overline{n}$.

The subtle difference between (4.6) and (4.8) is that $\overline{\xi}$ does not necessarily lie in the xy-plane, in which case the anchoring energy f_s is azimuthally not symmetric about the easy direction. For most surfaces however, the anchoring is symmetric with respect to ϕ_0 and (4.7) is valid for calculating the vectors $\overline{\xi}$ and $\overline{\eta}$.

4.2.2 Examples

A first simple example is planar alignment along the x-axis. If the xz-plane is a mirror plane for the anchoring, the anchoring energy can be written as

$$f_s = \frac{1}{2}\left[W_p (\overline{n} \cdot \overline{1}_z)^2 + W_a (\overline{n} \cdot \overline{1}_y)^2 \right]. \tag{4.9}$$

In this case the polar and azimuthal anchoring force, W_p and W_a, are separated. Written as a goniometric expression, planar anchoring ($\theta_0 = 0$) along an azimuthal direction ϕ_0 can thus be written as

$$f_s = \frac{1}{2}\left[W_p \sin^2\theta + W_a \sin^2(\phi - \phi_0)\cos^2\theta \right] \tag{4.10}$$

An important difference with equation (4.4) is that in the term representing the azimuthal anchoring, also the tilt angle θ of the director appears. For small deviations around the easy direction however, $W_{a'} = W_a \cos^2(\theta) \approx$ const. and the expression in equation (4.4) is obtained.

Depending on the magnitude of W_p and W_a, the anchoring strength is presumed strong, medium or weak [16]. An overview of the typical ranges is given in Table 4.1.

Table 4.1: Ranges for weak, medium and strong anchoring for the azimuthal and polar anchoring energy.

	Azimuthal anchoring W_a	Polar anchoring W_p
Strong	$> 10^{-4}$ J/m^2	$> 10^{-3}$ J/m^2
Medium	$\approx 10^{-5}$ J/m^2	$\approx 10^{-4}$ J/m^2
Weak	$< 10^{-6}$ J/m^2	$< 10^{-5}$ J/m^2

For homeotropic alignment, (4.8) is converted to

$$f_s = \frac{1}{2}\left[W_1 (\overline{n}\cdot\overline{1}_x)^2 + W_2 (\overline{n}\cdot\overline{1}_y)^2 \right]. \tag{4.11}$$

For flat isotropic surfaces W_1 and W_2 are equal and the anchoring has circular symmetry, but due to material anisotropy or surface treatment the symmetry can be broken and different values are possible.

By special treatment of the surface, it is possible to obtain multiple stable orientations of the director [91, 103]. As it is not possible to describe this by (4.8), this requires a more complicated form of the anchoring energy.

In the three-dimensional simulation tool MonLCD, (4.8) is used to model weak anchoring. Planar azimuthally degenerated anchoring can be modeled by setting the azimuthal weight parameter W_a in (4.9) equal to zero:

$$f_s = \frac{W_p}{2}(\overline{n}\cdot\overline{1}_z)^2. \tag{4.12}$$

In this case, there is an energy penalty when the director is oriented out of the xy-plane, without any constraint on the azimuthal direction.

4.3 Weakly anchored in-plane switching mode

The one-dimensional approximation of the in-plane switching mode, as described in section 2.5, is limited to strong anchoring. In this section, an extension to weak anchoring is made.

In stead of a rigid surface director, the planar anchoring is now modeled by the surface anchoring energy (4.9). This yields a free energy

$$F = \frac{1}{2}\int_0^d \left[k_{22}\left(\frac{\mathrm{d}\phi}{\mathrm{d}z}\right)^2 - \varepsilon_0\,\Delta\varepsilon\,E^2\,\cos^2\phi\right]\mathrm{d}z + \frac{W_a}{2}\left[\sin^2\left(\phi(0)-\phi_0\right)+\sin^2\left(\phi(d)-\phi_0\right)\right]. \tag{4.13}$$

The integral consisting of the distortion and electric energy in the bulk is identical to that for strong anchoring. The two additional terms specify the azimuthal anchoring at the top and bottom surfaces. Since the tilt angle of the director is not changed by the applied field along the x-axis, θ remains equal to zero and the polar anchoring does not appear in the expression.

An analogous normalization is performed for the electric field E and the height z as was done for strong anchoring, using equations (2.7) and (2.8). After division by the common factor $k_{22}/2d$, the normalized expression of the free energy is

$$F_{\mathrm{norm}} = \int_0^1 \left[\left(\frac{\mathrm{d}\phi}{\mathrm{d}\zeta}\right)^2 - \pi^2 h^2\,\cos^2\phi\right]\mathrm{d}\zeta + \frac{\pi}{\rho}\left[\sin^2\left(\phi(0)-\phi_0\right)+\sin^2\left(\phi(1)-\phi_0\right)\right], \tag{4.14}$$

with

$$\rho \;=\; \frac{\pi\,k_{22}}{W_a\,d} \tag{4.15}$$

a dimensionless reduced surface-coupling parameter which is a measure for the azimuthal anchoring strength at the surface. h and ζ are the normalized electric field and height.

The principle of Calculus of Variations [40] yields that the minimum energy solution for the twist $\phi(\zeta)$ in equation (4.14) must fulfill the differential equation

$$\frac{\mathrm{d}^2\phi}{\mathrm{d}\zeta^2} - \pi^2 h^2 \sin\phi\cos\phi = 0, \tag{4.16}$$

with the boundary conditions

$$\left.\frac{\mathrm{d}\phi}{\mathrm{d}\zeta}\right|_{\zeta=0} + \frac{\pi}{2\rho}\sin\left[2\left(\phi(0)-\phi_0\right)\right] = 0 \tag{4.17a}$$

$$\left.\frac{\mathrm{d}\phi}{\mathrm{d}\zeta}\right|_{\zeta=1} - \frac{\pi}{2\rho}\sin\left[2\left(\phi(1)-\phi_0\right)\right] = 0. \tag{4.17b}$$

The differential equation (4.16) is identical to (2.12) that was obtained for strong anchoring, but the boundary conditions have changed. The differential system is again solved numerically, using the Matlab solver. Also for weak anchoring, the number of independent variables is strongly reduced. Besides the normalized electric field h and the azimuthal alignment direction ϕ_0, the reduced surface-coupling parameter ρ must be specified additionally.

As a first example, the one-dimensional simulation of the in-plane switching mode of liquid crystals in Figure 2.12 is repeated with weak anchoring instead of strong anchoring. The twist angle ϕ is given in Figure 4.1 as a function of the height ζ for $\phi_0 = 85°$, $\rho = 0.25$ and different equally spaced values of the applied field h.

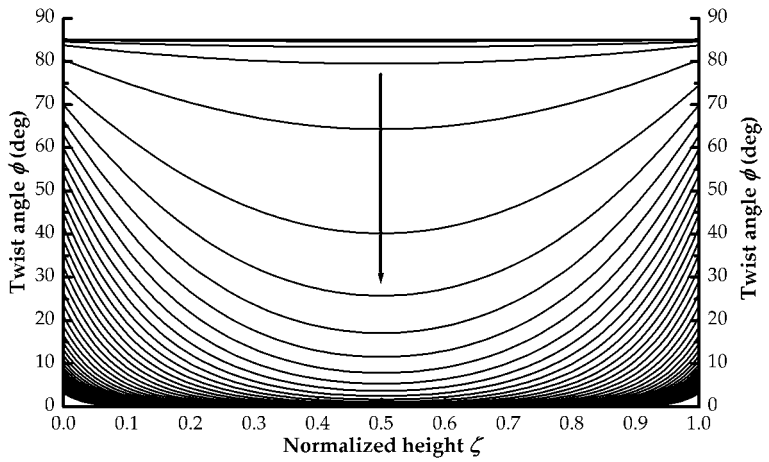

Figure 4.1: The twist angle ϕ in the weakly anchored one-dimensional approximation of the in-plane switching mode as a function of the relative height ζ, for different equally spaced values of the electric field $h = 0, 0.2, \ldots, 10$, $\rho = 0.25$ and $\phi_0 = 85°$. For $h = 0$, the twist ϕ is constant along the alignment $\phi_0 = 85°$ and for increasing h the midplane twist decreases toward 0. The arrow indicates the direction in which the field increases.

The plots of the twist as a function of the height ζ show a similar behavior as in Figure 2.12 for $\rho = 0$. For $h = 0$ the twist $\phi(\zeta)$ is a constant, equal to the alignment ϕ_0 of 85°. For increasing values of the normalized field h, the midplane director rotates toward the field along x-axis and the twist angle ϕ decreases. Because of the weak surface anchoring, not only the bulk director is reoriented, but also the surface director has rotated toward the electric field.

The influence of the anchoring strength ρ becomes clearer in Figure 4.2. The midplane and surface twist are plotted as a function of the applied field h for $\phi_0 = 85°$ and different values of the reduced surface-coupling parameter ρ. The largest influence of the anchoring strength ρ

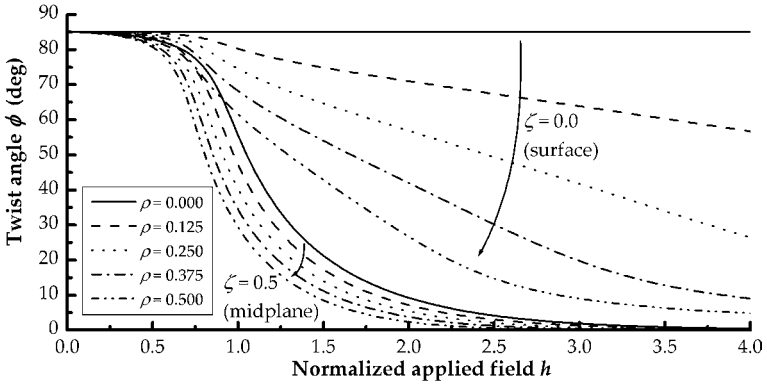

Figure 4.2: The midplane twist $\phi(1/2)$ and the surface twist $\phi(0)$ for weak and strong anchoring as a function of the applied field h for $\rho = 0,\ 0.125,\ \ldots,\ 5$ and $\phi_0 = 85°$.

is visible on the surface director. Above the threshold, the surface twist varies almost linearly toward zero. The midplane twist shows an analogous variation as in the strongly anchored case ($\rho = 0$), with a slight reduction of the threshold field.

The reduced surface-coupling parameter ρ is related to the extrapolation length [11, 94, 104]

$$\xi_a = \frac{k_{22}}{W_a} = \frac{\rho\, d}{\pi}, \tag{4.18}$$

which is the ratio of surface rotation of the director to the director gradient at the interface for small changes of the surface twist [94, 105].

The extrapolation length ξ_a is an equivalent way, often used in literature, to specify the anchoring strength. It is proportional to the di-

mensionless surface-coupling parameter ρ and inversely proportional to the weight parameter W_a. If both polar and azimuthal anchoring are important, separate extrapolation lengths ξ_a and ξ_p must be specified [11, 92].

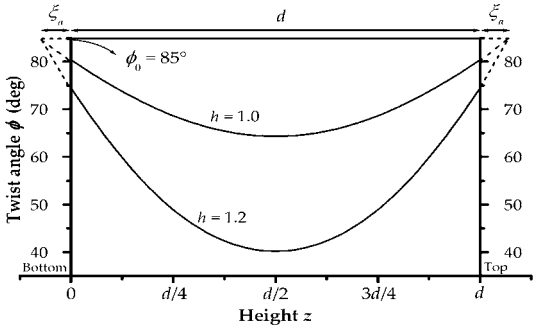

Figure 4.3: Twist ϕ as a function of the height z with indication of the extrapolation length ξ_a, for $h = 1.0$ and $h = 1.2$ in case $\phi_0 = 85°$ and $\rho = 0.25$.

Physically, ξ_a corresponds to an increment of the cell thickness d, as illustrated in Figure 4.3, in such a way that there is no change of the twist at the effective boundaries.

The effective cell thickness $d + 2\xi_a$ must be used for the calculation of the threshold voltage in the weakly anchored in-plane switching mode [3, 104]. Therefore, the threshold voltage V_{th} for alignment perpendicular to the electric field E is reduced to

$$V_{th} = \frac{\pi g}{d + 2\xi_a} \sqrt{\frac{k_{22}}{|\Delta\varepsilon|\,\varepsilon_0}}. \tag{4.19}$$

The electro-optic characteristic of the weakly anchored in-plane switching mode is given in Figure 4.4 for different values of the surface-coupling parameter ρ as a function of the applied field and $\phi_0 = 85°$. The calculations are carried out with the Jones Matrix Method using a layer thickness d of 2.1 µm, a wavelength λ of 600 nm and the parameters of the liquid crystal E7.

The influence of the anchoring strength is clearly visible. The threshold field is reduced and the rotation of the surface director increases the optical response at weaker fields compared to the strongly anchored case plotted in Figure 3.5. The steeper increase of the electro-

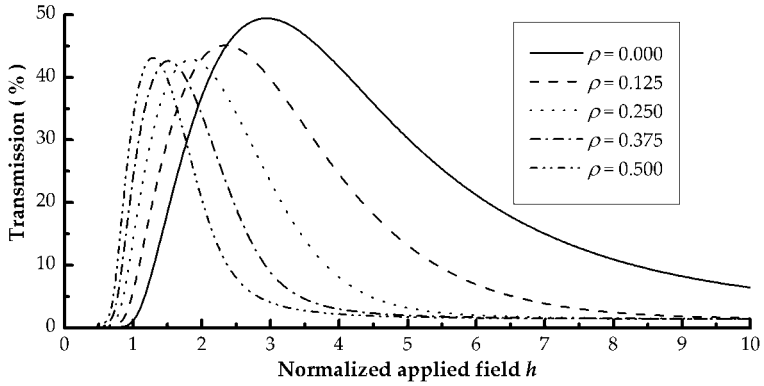

Figure 4.4: Electro-optic characteristic in the in-plane switching mode for different values of the anchoring strength ρ = 0, 0.125, ..., 5, ϕ_0 = 85° and crossed polarizers with the transmission axes parallel and perpendicular to the anchoring.

optic characteristic reduces drastically the switching voltage range needed for active matrix applications.

Drawback of weak anchoring, is the increase of the relaxation time when returning to the off-state [106]. The decrease of the anchoring strength weakens the torque which returns the director to its initial state after removing the applied voltage. Furthermore, the relaxation time becomes dependent on the time that the voltage was applied [14]. Especially in display applications with moving images, this limits the applicability of weak anchoring.

4.4 Measurement of the anchoring strength

Measurement of the anchoring strength is indispensable for comparing alignment methods and materials. In this section the approach is described for a number of measurement setups found in literature.

4.4.1 Field-off techniques

The measurement setups can be divided in two groups, depending on the way a torque is applied to the surface director. In field-off techniques, the anchoring strength is determined without the application of an external field. The elastic torque generated by the distortion of the

director distribution is used for determining the anchoring strength.

In the experiments, a liquid crystal layer is sandwiched between two surfaces. At one side a reference surface with strong anchoring is used and at the other side the weakly anchored surface under testing. After recording the anchoring onto the test surface, one substrate is rotated 90° around the surface normal compared to the other, keeping the distance between the surfaces constant. The twist distortion of the director generates a torque on the surface director.

The deviation of the weakly anchored surface director on the test surface is measured optically as a function of the distance between the substrates and allows to estimate the extrapolation length. Adjusting the distance between the substrates can be done mechanically [93] or can be avoided by using a spherical counter plate [86, 107] or a wedge cell [90].

The difficulty with these experiments is to simultaneously keep the substrates parallel, adjust the distance and measure the transmission. Therefore, other field-off techniques were developed which determine the anchoring strength directly by measuring the torque when rotating the substrates [108–110] or measuring the thickness of domains walls separating regions with different director orientations [111, 112].

4.4.2 Field-on techniques

In field-on techniques, an electric [113,114] or magnetic [115,116] field is used to generate a torque on the liquid crystal director. The anchoring energy is measured either by its influence on the Fréedericksz transition [11], the influence on the electro-optic characteristic [115] or the deviation of the surface director [113, 114].

Since the expertise to perform the described measurements was not available in our lab, I developed a new field-on measurement method, described in section 4.6.3.b, to experimentally estimate the azimuthal anchoring strength. The anchoring strength is estimated by detailed transmission measurements on liquid crystal cells using the in-plane switching mode.

4.5 Flow and memory anchoring

Against common sense, most flat surfaces which are not especially treated to orient the surface director along a certain direction, will still give rise to a fixed orientation of the surface director. This undesired anchoring is generally quite strong and depends heavily on the used surface material and liquid crystal. The two phenomena responsible for this are flow and memory alignment.

In a nematic liquid crystal cell with untreated surfaces, the director at the surface aligns along the filling direction. This is known as flow alignment [86, 93] and can be avoided by heating the cell above the nematic-isotropic transition temperature during the filling process.

After cooling to the nematic phase, a liquid crystal cell with isotropic surfaces not treated to obtain a preferential alignment, yields a Schlieren texture [3, 4, 117]. The director lies in the horizontal plane with a gradually varying orientation. Between crossed polarizers this gives a typical pattern with dark regions where the liquid crystal is oriented parallel with one of the polarizers and bright regions where the director makes an angle of 45° with them (see Figure 4.5). The director variation in the Schlieren texture is random, not induced by any surface anisotropy.

By symmetry, the isotropic surface should in principle yield a continuously degenerated azimuthal anchoring. In practice, this is the case only at the first contact of the liquid crystal with the surface, resulting in an initial random alignment.

A strong electric field can change the director distribution in the Schlieren texture. Yet, after removal of the electric field, the original Schlieren texture is restored. Even heating the sample above the clearing point does not destroy the Schlieren texture. This is known as memory alignment [86, 93, 118], which implies that the local orientation of the director is memorized onto the surface. The two responsible mechanisms for memory alignment are adsorption of the liquid crystal molecules at the surface [86,93] and anisotropic interactions of polymer molecules at the surface with the liquid crystal director [86].

Memory alignment is difficult to avoid and the residual anchoring can be rather strong. For intended weak anchoring, it can modify drastically the initial strength, the orientation and even the symmetry of the azimuthal anchoring. In this way memory alignment defines an inhomogeneous monostable anchoring. Under strong torques the adsorbed

layer can in some cases change its easy axis orientation (surface gliding) and its anchoring strength. The anchoring thus becomes strongly dependent on the sample history, which is harmful for almost any application.

4.6 Weak anchoring experiments

Planar azimuthally degenerated anchoring is prevented mainly by memory alignment. Many studies are devoted to the anchoring phenomenon of nematic liquid crystals [86,92,93,118,119] and complicated equipment is required to measure the anchoring strength. In this section, information will be obtained about the anchoring strength using a simple approach.

4.6.1 Cell preparation

To study the anchoring properties, a number of test cells with different surface layers are prepared. A test cell consists of a thin liquid crystal layer sandwiched between two glass substrates. The glass surfaces are covered with transparent electrodes and the different alignment materials under testing. Unlike typical liquid crystal cells, the surface of our test cells is not treated to obtain a preferential director orientation and thus yields a Schlieren texture. The goal is to find a material that allows a change of the surface director with a minimal azimuthal anchoring strength. In the experiments four different surface layers are compared:

- PI: A polyimide layer deposited by spin coating a 1 wt % solution of polyimide in n-methyl-2-pyrrolidone

  Polyimide is commonly used as an alignment layer for liquid crystals. After rubbing, a strong alignment along the direction of rubbing is obtained. Without rubbing, polyimide suffers from strong memory alignment [119]. In our experiments PI2610 of HD microsystems is used.

- FC4430: A combination of the polyimide layer with a surfactant layer FC4430 on top, deposited by dip coating the PI-coated substrate in a 1 wt % solution of FC4430 in water

Novec FC4430 fluorosurfactant is a non-ionic polymeric surfactant by 3M which imparts low surface tension in organic coating systems. FC4430 is used as a wetting, leveling and flow control agent in solder fluxes, inks and water borne or solvent based coatings. It is the improved version of the previous FC430 that was studied in reference [119], but opposite to the former experiments the material is not mixed in the liquid crystal but deposited as a Langmuir-Blodgett film [120] on top of a polyimide coating by dip coating.

– 3-GPS: A layer of (3-glycidoxypropyl)trimethoxysilane deposited by spin coating a 1 wt % solution of 3-GPS in 2-butoxyethanol

  Experiments in reference [93] demonstrated memory free anchoring with 3-GPS. Here the properties are studied in more detail.

– BCB: A layer of benzocyclobutene deposited by spin coating Cyclotene 3022-35.

  BCB is a polymer used as a dielectric in a wide range of microelectronic applications. The used BCB, is deposited with Cyclotene from the Dow Chemical Company.

For testing the azimuthal anchoring of the different materials, an electric field is needed that is able to change the azimuthal angle of the director. Therefore, the in-plane switching mode of liquid crystals is used. The in-plane switching substrates were produced in our lab and have a gap g and electrode width w of about 30 μm. The cell thickness d is 2.1 μm. This is rather thin for nematic liquid crystal cells, but ensures a high influence of the anchoring on the director reorientation. The liquid crystal used in the experiments is E7. The high birefringence of E7 ($\Delta n = 0.2269$) gives a retardation $\Delta nd > \lambda/2$, so that the thin cells yield a substantial electro-optic response.

4.6.2 Microscope observations

a) Static microscope observation

The first step in the experiments is the microscopic observation of the Schlieren textures of the cells between crossed polarizers. During the cooling process from the isotropic to the nematic phase, droplets of nematic liquid crystal grow in the isotropic liquid. If the initial anchoring

strength is low, the director orientation inside the droplets is homogeneous and the director in merging droplets is reoriented by the elastic torques toward a smooth continuous variation of the director. In this way the size of the homogeneous regions increases for weaker anchoring strengths [119].

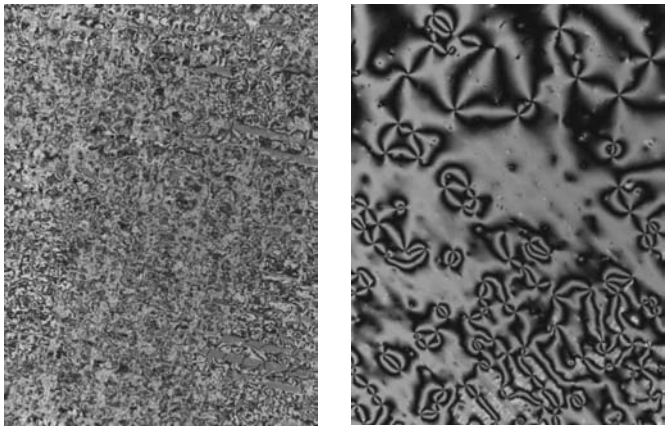

(a) PI (b) FC4430

(c) 3-GPS (d) BCB

Figure 4.5: Observation of the Schlieren texture of the liquid crystal cells between crossed polarizers for the four tested alignment materials. Image dimension 900 μm $\times$ 1200 μm.

Figure 4.5 shows the Schlieren textures of the four different liquid crystal cells between crossed polarizers, observed with a microscope. The axes of the polarizers are oriented along the horizontal

and vertical sides of the pictures. The observed region measures about 900 μm×1200 μm. The director is parallel to the substrate surfaces with a gradually varying twist angle. There is no variation of the director along the surface normal.

The observed liquid crystal area contains no line defects, only singular points [3,4,117]. These are topological defects which are assigned a certain strength s. The director distribution around the singular point is illustrated in Figure 4.6 for a number of frequently appearing examples. The strength s is determined by the number of dark brushes that cut a circle drawn around the singularity when it is positioned between crossed polarizers: $|s| = \#\,brushes/4$. The sign of the strength s is determined by the behavior of the brushes between rotating crossed polarizers. If the brushes rotate in the same direction as the crossed polarizers, the defect is assigned a positive sign.

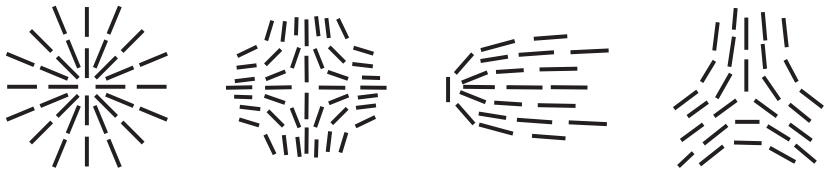

(a) $s = +1$ (b) $s = -1$ (c) $s = +1/2$ (d) $s = -1/2$

Figure 4.6: Director distribution in the different types of singular points which can appear in the director distribution of Schlieren textures.

Defects with opposite strength s can attract each other and eventually annihilate, to form a homogeneous director orientation. Defects with different strength can not cancel each other, but may form a new defect with the strength being the sum of the individual values. Generally, the sum of the strengths of all defects in a sample tends to go to zero.

For polyimide the regions with the same brightness where the director is more or less homogeneous, are very small in the order of a few μm. The director of the nematic droplets which are formed after cooling is immediately strongly anchored at the surface and movement of the singular points is not possible.

For FC4430, 3-GPS and BCB covered cells, the director is not yet anchored during the cooling process. Reorientation of the director and annihilation of singular points leads to the creation of large homoge-

neous regions with sizes up to 100 μm. These materials are thus candidates for planar azimuthally degenerated anchoring surfaces, but to obtain information about the memory alignment further experiments are necessary.

b) Influence of memory alignment

The effect of memory alignment is observed by comparing the Schlieren texture before and after applying an ac voltage over the electrodes. The memory effect tends to restore the original Schlieren texture after switching off the voltage. Without the memory effect, the final texture would be determined by the director configuration during the application of the voltage.

When applying a voltage of 100 V over the electrodes, the electric field rotates the director between the electrodes in a plane parallel to the surfaces. Above the electrodes, the electric field has a strong vertical component which yields a large tilt angle. Left and right of the center of the electrode, the director has tilted in opposite directions and a defect line is created above the center of the electrodes.

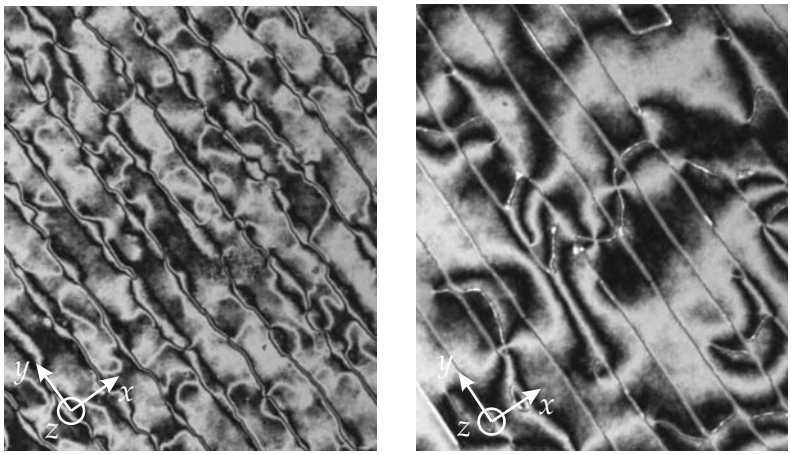

(a) 3-GPS (b) BCB

Figure 4.7: Line defects created in the liquid crystal cells above the center of the in-plane switching electrodes after applying a high voltage to the electrodes for the cells covered with 3-GPS and BCB. Image dimensions: 540 μm × 640 μm

After removal of the electric field, the Schlieren texture in the PI,

3-GPS and BCB cell is largely restored in less than one second, but the defects formed during switching remain visible in the liquid crystal as illustrated in Figure 4.7 for the 3-GPS and BCB cell. Thus although the anchoring was initially weak, the memory effect leads to stronger anchoring.

c) Memory alignment in the 3-GPS cell

The lines in the 3-GPS sample of Figure 4.7(a) are surface inversion walls, that correspond to a 180° rotation of the director in a plane parallel to the surface [4, 117]. The surface inversion walls are located above the centers of the in-plane switching electrodes. Figure 4.8 shows the director distribution in a surface inversion wall above an in-plane switching electrode. There is no variation of the director along the surface normal. While making the 180° in-plane rotation of the director, the director is at two locations parallel to one of the polarizer axes (indicated with P and A). Observed through a microscope, these locations will appear as dark lines as is visible in Figure 4.7(a) and are indicated with the gray regions in Figure 4.8. In the neighborhood of the double line, the transmitted color remains the same because the director is everywhere parallel to the substrate surfaces.

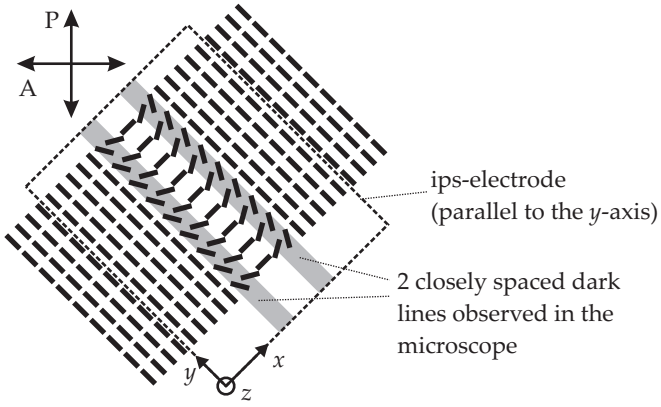

Figure 4.8: Director distribution inside the surface inversion wall located above the center of the in-plane switching electrodes in the 3-GPS cell and its appearance as two closely spaced dark lines when observed through a microscope with crossed polarizers along the axes A and P.

The width of the surface inversion wall is related to the strength of the azimuthal anchoring at the surfaces. In a thin inversion wall,

a large amount of elastic energy is present with strong elastic torques on the director. A reduction of the azimuthal anchoring strength at the surface will allow the inversion wall to spread out.

Using an approximation, it is possible to find a relation between the width of the surface inversion wall and the azimuthal anchoring strength. The director distribution described in Figure 4.8 is one-dimensional (only variations along x), the director is parallel to the xy-plane in the whole liquid crystal layer and characterized by the twist angle $\phi(x)$. If a weak azimuthal anchoring along the y-axis with anchoring strength W_a is assumed at both the top and bottom surface, the free energy of the liquid crystal layer with thickness d per unit length in the y-direction over a region with width L in the x-direction is:

$$F = \int_{-L/2}^{L/2} \left[\frac{d}{2} \left(k_{11} + (k_{33} - k_{11}) \cos^2 \phi \right) \left(\frac{\mathrm{d}\phi}{\mathrm{d}x} \right)^2 + W_a \cos^2 \phi \right] \mathrm{d}x. \quad (4.20)$$

Substitution of the integrand in the the Euler-Lagrange equation shows that the minimal energy solution of the twist $\phi(x)$ must satisfy the differential equation

$$\left(\frac{\mathrm{d}^2\phi}{\mathrm{d}x^2} \right) \left(k_{11} + (k_{33} - k_{11}) \cos^2 \phi \right) + \left(\frac{\mathrm{d}\phi}{\mathrm{d}x} \right)^2 \frac{(k_{33} - k_{11})}{2} \sin 2\phi + \frac{W_a}{d} \sin 2\phi = 0. \quad (4.21)$$

This differential equation is solved numerically with boundary equations $\phi(-L/2) = -90°$ and $\phi(L/2) = 90°$ with $L >> d$. The twist angle ϕ as a function of the lateral position x in the surface inversion wall is plotted in Figure 4.9. The results were calculated for the liquid crystal material E7, a cell thickness $d = 2.1$ µm and different values values of the azimuthal anchoring strength W_a.

The variation of the twist ϕ in Figure 4.9 shows that for increasing values of the anchoring strength W_a, the 180°in-plane rotation of the twist is confined to a narrower region as expected. Figure 4.10 shows the transmission through the surface inversion wall as a function of the lateral position x, calculated with the Jones Matrix Method. The polarizers are oriented at ±45° with the alignment as in Figure 4.8.

For low values of the azimuthal anchoring strength W_a, the distance Λ between the two minima of the transmission increases. The width

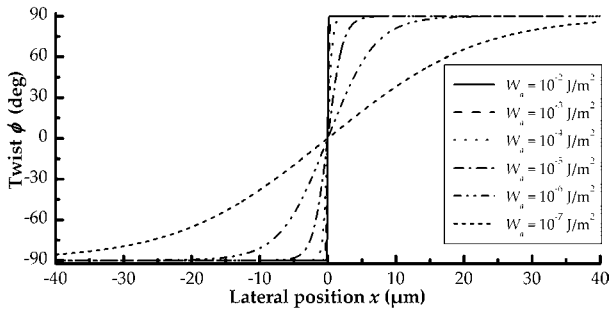

Figure 4.9: Variation of the twist ϕ as a function of the lateral position x in a surface inversion wall for different values of the azimuthal anchoring strength W_a.

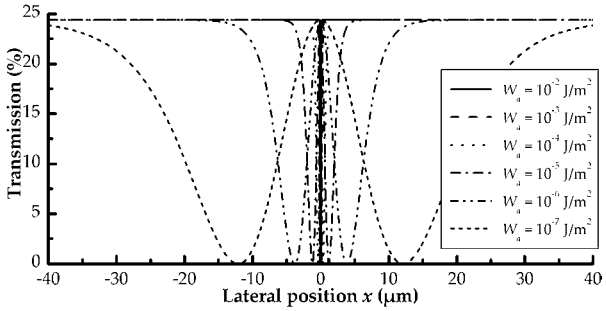

Figure 4.10: Variation of the transmission through a surface inversion wall between crossed polarizers as a function of the lateral position x for different values of the azimuthal anchoring strength W_a.

Λ is plotted as a function of the azimuthal anchoring strength W_a in Figure 4.11. The plot shows that the width Λ decreases proportionally to the square root of the azimuthal anchoring strength W_a

More generally, an inspection of the parameters in equation (4.21) shows that

$$\Lambda^2 \sim \frac{d}{W_a}. \tag{4.22}$$

A variation of the azimuthal anchoring strength W_a or the thickness d leads to a proportional variation of Λ^2. The proportionality constant in (4.22) depends on the elastic constants k_{11} and k_{33}.

The surface inversion walls observed in Figure 4.7(a) have a width Λ of approximately 2.5 μm. Using Figure 4.11, this allows to estimate the anchoring strength W_a. The value found for W_a is approximately

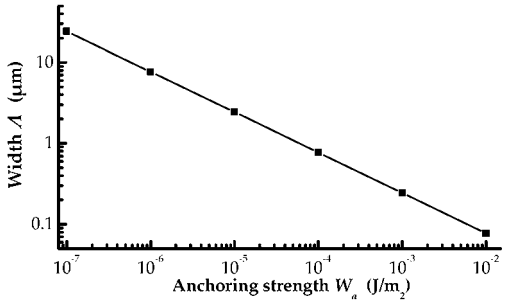

Figure 4.11: Width of the inversion wall Λ as a function of the anchoring strength W_a.

5×10^{-6} J/m^2. According to Table 4.1, this is in the range of medium anchoring. Thus 3-GPS indeed lowers the azimuthal anchoring strength, but the value of W_a is still considerable.

The relation between the width of surface inversion walls Λ and the azimuthal anchoring strength W_a can be used to understand the observed Schlieren textures in Figure 4.5. For weak initial azimuthal anchoring, the homogeneous regions are large because the anchoring allows the regions with large elastic torques to spread out, resulting in a homogenizing of the director distribution.

For strong initial anchoring, as was the case for PI, this reasoning doesn't hold. The anchoring strength W_a is large and the directions ϕ_0 at top and bottom can very well be different. This leads to fast lateral variations along x and y in the color of the observed Schlieren texture because ϕ varies in the z-direction.

d) Memory alignment in the BCB cell

The defects observed in the BCB cell in Figure 4.7(b) are disclination lines [117], line singularities that appear as a single dark line and either form closed loops, or connect two $s = \pm1/2$ singular points. Since the singularity lies close to one surface, the director distribution is not influenced. Therefore, it seems as if the Schlieren texture is not affected by the lines. In the neighborhood of the line, the director is oriented out of the horizontal plane and a change in color is observed around the line.

Optically, it is not possible to determine which type of disclination

line is present. By observation of the Schlieren texture it is only possible to gain information about their origin.

In Figure 4.12, four highly magnified pictures of the same area of the BCB cell are shown. The cell is positioned between crossed polarizers with the polarizer transmission axes parallel to the edges of the pictures. In Figure 4.12(a), the in-plane switching electrodes, indicated with the shaded areas, are oriented parallel to the horizontal edge of the picture. The visible defect lines are mainly horizontal, situated above the center of the electrodes. At the endpoints of the straight segments, the defect lines are either interrupted (area 1) or cross the gap to a neighboring electrode (area 3). One can notice that such endpoints always occur in a dark region.

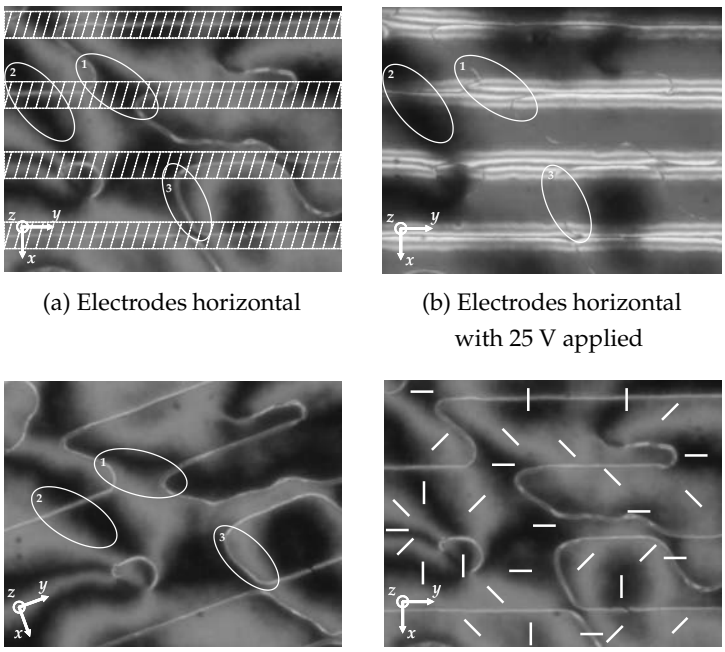

(a) Electrodes horizontal

(b) Electrodes horizontal with 25 V applied

(c) Electrodes at 20°

(d) Electrodes horizontal with the director distribution indicated

Figure 4.12: Transmission images of the in-plane switching BCB cell with defects between crossed polarizers. The transmission axes of polarizer and analyzer are oriented along the horizontal and vertical edges of the pictures. Image dimensions: 290 μm × 225 μm

On the other hand, in other dark regions as in area 2, the defect line

is undisturbed. The reason is the orientation of the director in the dark region. If the director is parallel to the electrodes, the defect line above the electrode disappears as in areas 1 and 3. If it is perpendicular to the line, the defect line remains as in area 2. This is confirmed by Figure 4.12(b). This picture shows the same cell area, with 25 V applied over the electrodes. The picture was strongly overexposed in order to have different shades in the regions between the electrodes. A further increase of the applied voltage would make the whole area in between the electrodes homogeneously black. In area 2 where the director was already perpendicular to the electrodes, the director is unaffected and the area remains perfectly black despite the high intensity of the incident light. In the areas 1 and 3, the director is rotated toward the electric field and the dark area changes intensity. Only above the center of the electrodes in area 1, a thin dark region is still present where the director is along its original direction.

By now, the director orientation can be distinguished in the dark regions (horizontal or vertical). To determine the director orientation in the bright regions, the sample must be rotated with respect to the crossed polarizers as shown in Figure 4.12(c). By following the direction in which a dark brush moves, it is possible to determine the director distribution in the intermediate regions. The director orientation in a particular brush remains the same with respect to the polarizers. In area 1 of Figure 4.12(a), the dark brush contains horizontal directors. After a rotation of 20° the dark brush is shifted to the edge of area 1, which means that at this new location the director is now horizontal. By rotating back, the original director distribution at this location is obtained. In this way, the director distribution in the whole cell can be determined as shown in Figure 4.12(d).

In area 3 of Figure 4.12(a), a defect line is created that crosses between two neighboring electrodes. To understand why, we have a closer look at the director distribution around the defect line. Before any voltage was applied to the cell and the defect line was not yet created, the director in the dark region of area 3 was oriented horizontal as represented in Figure 4.13(a). To the left and the right the director is rotated 45° in opposite directions.

When applying a voltage over the electrodes, an electric field $\overline{E}$ is generated which forces the director at the left and the right to rotate toward the electric field. At the center, the director is perpendicular to the electric field and does not feel a torque. At both sides of the

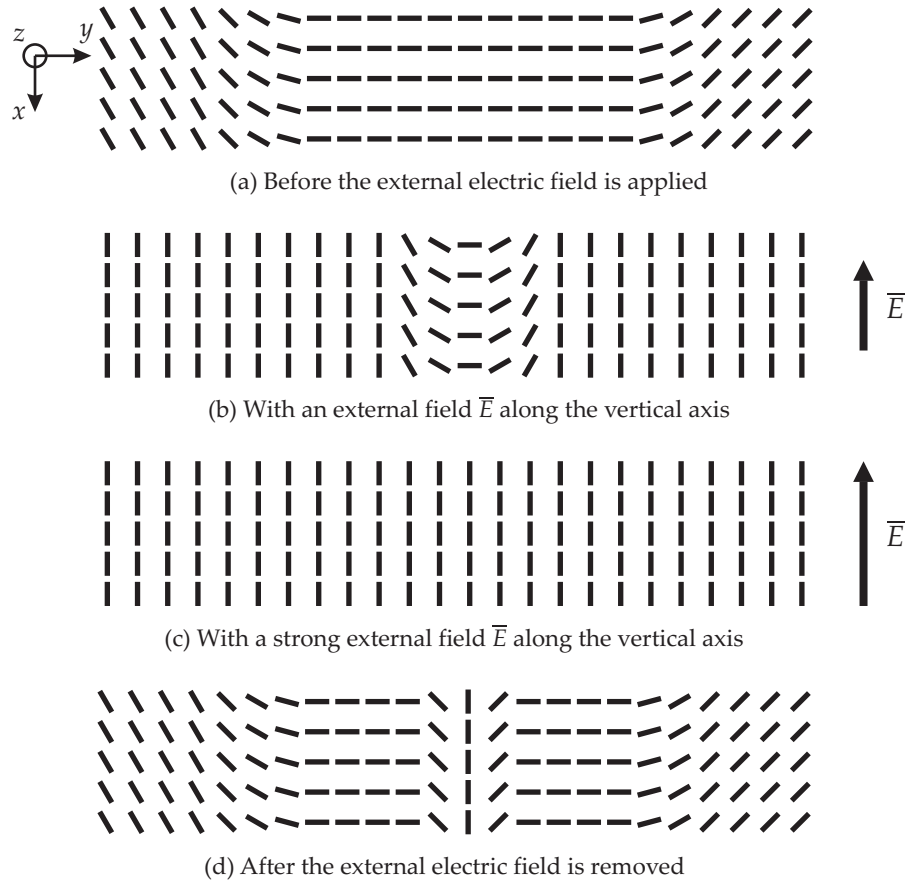

(a) Before the external electric field is applied

(b) With an external field $\overline{E}$ along the vertical axis

(c) With a strong external field $\overline{E}$ along the vertical axis

(d) After the external electric field is removed

Figure 4.13: Origin of the defect line in area 3 of Figure 4.12, by observing the effect of an externally applied electric field $\overline{E}$ on the director distribution in the plane parallel to the substrate.

center, the rotation toward the electric field $\overline{E}$ occurs in opposite directions. When the applied voltage is increased, the two side regions grow at the expense of the center region as shown in Figure 4.13(b), leaving a narrow region where the director is still horizontal. Finally with a strong electric field, the high distortion energy in the center region is dissolved by flipping the director in the middle 90°, forming a homogeneous distribution with the two neighboring regions as is illustrated in Figure 4.13(c).

After switching off the applied voltage, the director in the side regions rotates back to the original orientation. Only near the center, the

director remains vertical as represented in Figure 4.13(c), due to the opposite elastic torques at both sides. This creates a high energy region since the center director is perpendicular to its anchoring direction and causes the creation of a defect line that crosses between the two neighboring electrodes.

e) Switching and relaxation for FC4430

To test the memory alignment on FC4430, four photographs were taken of the same area in a cell covered with FC4430. Before taking a picture, a 1 kHz / 100 V square wave is applied to the in-plane switching electrodes during 1 min, followed by a short circuit during 3 min. In this way, four consecutive pictures were taken of the cell, with each time in between a high voltage applied during 1 min and a short circuit of 3 min. The four resulting images are shown in Figure 4.14.

Comparing the four pictures shows that the Schlieren texture is changed after each step. The change in the director distribution obtained after 3 min of short circuit is stable. Unless another voltage is applied to the electrodes, it remains unchanged. This indicates that the memory effect is lowered seriously if the surfaces of the cell are covered with FC4430. Moreover, unlike the BCB and 3-GPS cells discussed in the previous section, the obtained director distribution in the FC4430 cell is free of defect lines.

The change in the Schlieren texture in Figure 4.14 and the absence of defect lines requires a more detailed treatment. In Figure 4.15, the FC4430 cell is shown between crossed polarizers with 100 V applied. In Figure 4.15(a), the electrodes are oriented parallel to the horizontal edge of the picture and to one of the polarizer axes. Because of the high voltage applied, a strong electric field is present which rotates the director in the plane perpendicular to the electrodes. Therefore the director is oriented perpendicular to the axis of one of the polarizers and for the greater part of the cell area, the transmission is dark. Only two closely spaced gray lines are visible above center of the in-plane switching electrodes. In Figure 4.15(b), the electrodes are oriented at 35° with the polarizer transmission axis and the picture edge. Between the electrodes, the image is bright while the area above the electrodes is darker with a line above the center.

In Figure 4.16, the transmission profile above the electrodes is plotted for Figures 4.15(a) and 4.15(b). Three regions can be distinguished:

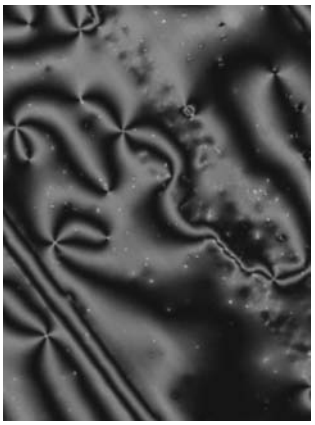

(a) Initial image before applying a voltage

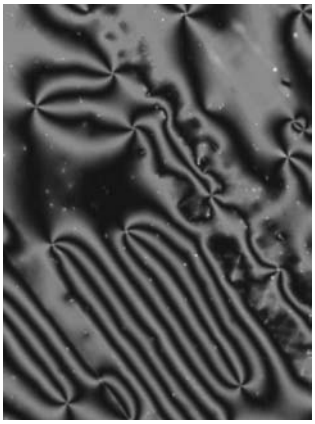

(b) Image after application of a square wave and a short circuit

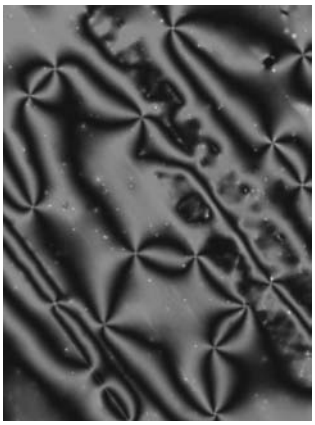

(c) Image after the second square wave and short circuit

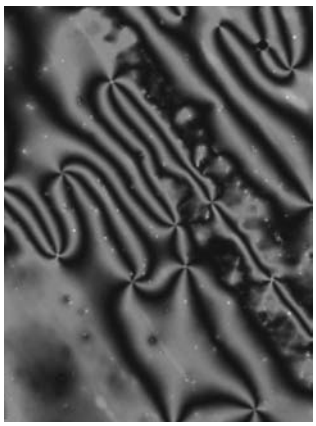

(d) Image after the third square wave and short circuit

Figure 4.14: Transmission image of the FC4430 cell between crossed polarizers with the polarizer axes along the horizontal and vertical edge of the pictures. Between each picture a 100 V square wave has been applied over the electrodes for 1 min, followed by 3 min of short circuit. The in-plane switching electrodes are oriented at 53° with the horizontal edge of the pictures. Image dimensions: 450 μm × 600 μm

a homogeneous region C between the electrodes, a region A above the center of the electrodes with a rapid variation in intensity and a homogeneous region B at both edges of the electrodes. A similar transmis-

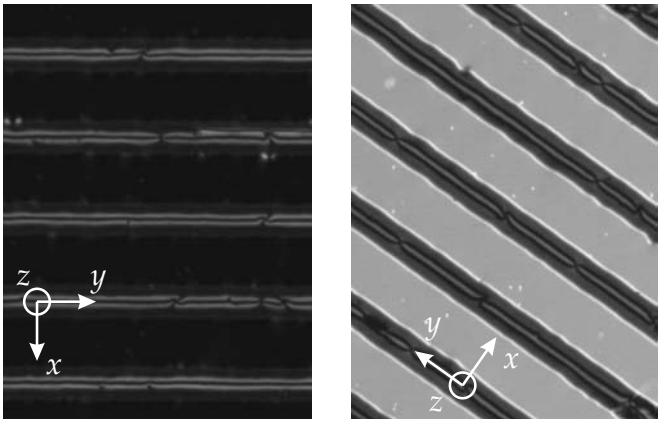

(a) Electrodes parallel to the horizontal edge of the picture

(b) Electrodes at 35° with the horizontal edge of the picture

Figure 4.15: Transmission image between crossed polarizers of the FC4430 cell with a voltage of 100 V applied. The polarizer axes are for both images oriented parallel to the edges of the pictures. Image dimensions: 225 μm $\times$ 300 μm

sion profile was observed above the electrodes of the strongly anchored in-plane switching mode in references [72, 121].

Taking into account the electric fields generated in the liquid crystal while applying a voltage over the electrodes, the director distribution can be estimated. The director between the electrodes (region C) lies along the x-axis, parallel with the electric field. For the electrodes parallel with the polarizer, regions B is dark. Thus, the director lies in the xz-plane, but not along the z-axis since rotating the polarizer orientation with respect to the electrodes yields light transmission in this region.

The line above the center of the electrodes in Figures 4.15(a) and 4.15(b) gives the impression that there is a defect line present in region A. But since after switching off there is no remaining disclination line visible, the director rotation from one side of region A to the other should be continuous.

Although the electric field in region A lies in the xz-plane, almost parallel to the z-axis, the director in region A does not remain in the xz-plane. For the electrodes parallel with one of the polarizer axes, two thin bright lines are visible in Figure 4.15(a), which is only possible if the director sticks out of the xz-plane. Moreover, in Figure 4.15(b) there

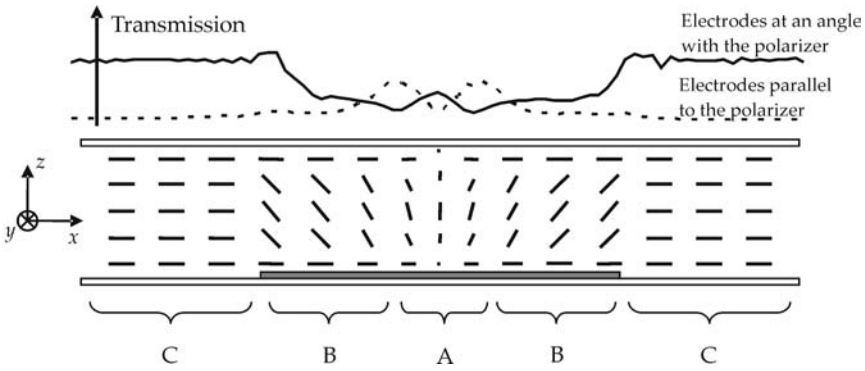

Figure 4.16: Schematic director distribution in an in-plane switching liquid crystal cell with the director weakly anchored at the surface, while a high voltage applied. Above, the transmitted intensity profile is shown, measured with a CCD-camera for the electrodes parallel or at an angle with the polarizers (electrode width w = 24 μm).

is a bright line at the center. Therefore the director in the center does not lie along the z-axis.

A combination of observations and two-dimensional simulations leads to the director distribution represented in Figure 4.16. The lines symbolize the projection of the director distribution on the xz-plane. At the surfaces, the anchoring forces keep the director horizontal. In region A, from left to right, the bulk director rotates on a cone around the z-axis. Two-dimensional simulations with the MonLCD-tool have shown that for a weakly anchored surface, the surface director can make a continuous rotation around the x-axis over the center. Moreover, the midplane tilt angle decreases with lower values of the surface anchoring strength W_a.

The director distribution in Figure 4.16 is confirmed by observation of the behavior after switching off. Shortly after removal of the applied voltage in Figure 4.15(b), the surface anchoring aligns all directors parallel to the substrate surfaces everywhere in the cell. As shown in Figure 4.17(a), the director in region B is now parallel with the x-axis, forming a homogeneous region with region C.

The director rotation on a cone in region A induced by the voltage that was applied is, after switching off the voltage, transformed into a narrow surface inversion wall. This is shown in Figure 4.17(a) which is taken 50 ms after switching off the applied voltage of Figure 4.15(b).

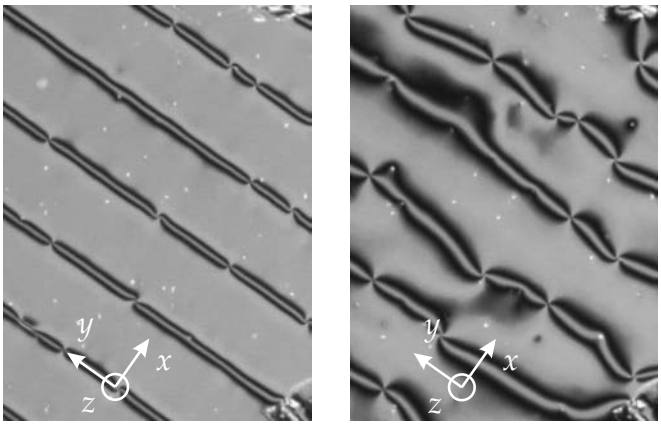

(a) after 50 ms (b) after 1.75 s

Figure 4.17: Transmission image for crossed polarizers (parallel tot the edges of the pictures) after switching off the applied voltage of 100 V of the observation in Figure 4.15(b). Image dimensions: 225 μm × 300 μm

The bright line in the center of the surface inversion wall has a director orientation perpendicular to the director orientation in regions B and C and therefore the same intensity. The location of the wall in Figure 4.17(a) is still above the center of the electrodes, as can be seen by comparing with Figure 4.15(b). The strong torque on the liquid crystal director in the surface inversion wall in combination with the weakly anchored director a the surface, forces the inversion wall to broaden and move in order to lower the elastic energy as can be seen in Figure 4.17(b), taken 1.75 s after switching off the voltage. Eventually, the defect points can attract each other and annihilate, leading to a random director distribution as in one of the pictures of Figure 4.14.

The director in region A of Figure 4.16 lies out of the xz-plane. The rotation on a cone around the z-axis from left to right in this region can be clockwise or counterclockwise. When two domains with opposite rotation approach each other, regions B and C join together without defects. In region A, the two approaching domains create a singular point with strength $s = +1$ or $s = -1$ depending on the orientation of the approaching domains. Figures 4.14 and 4.17 show indeed only fourfold singular points ($s = \pm 1$). In Figure 4.5(b) on the other hand, which was taken on the same cell before any voltage was applied, also twofold singular points ($s = \pm 1/2$) can be observed.

4.6.3 Transmission measurements

The above experiments indicate that the surface covered with FC4430 is a good candidate for true memory-free weak anchoring. To obtain a better idea of the anchoring properties, electro-optic measurements are performed on the different cells.

a) Average electro-optic measurements

A first measure for the anchoring strength is the threshold voltage. For the parameters of the prepared test cells, the threshold voltage V_{th} according to equation (2.10) which is valid for strong anchoring in a direction perpendicular to the electrodes, is 14.6 V. If the strength of anchoring is reduced, switching in the experiments should occur at lower voltages [39, 106].

Figure 4.18 shows the measured electro-optic characteristic, averaged over the regions A, B and C for the four types of cells at a wavelength λ of 600 nm. The electrodes are oriented parallel to one of the

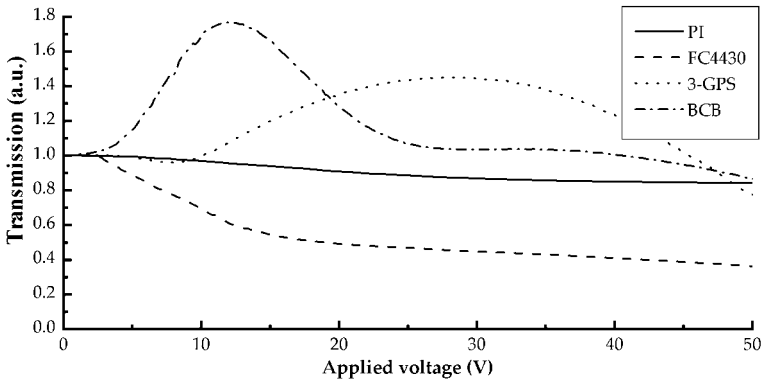

Figure 4.18: Measured average electro-optic characteristic of the non-rubbed in-plane switching liquid crystal cells between crossed polarizers, with the polarizer axes parallel and perpendicular to the electrodes.

crossed polarizers and the applied voltages are square waves with a frequency of 1 kHz. The measured transmission is normalized to an initial value of 1 for all materials.

Because the measured transmission is averaged over the three regions A, B and C and the director without any voltage applied varies randomly over the surface, the transmission curves are shaped differ-

ently than those calculated with the one-dimensional approximation of the in-plane switching mode in Figure 4.4. At 0 V, the transmission is not zero due to the variation of the director on the surface. The maximum applied voltage is not high enough to reach zero transmission.

A clear difference is visible between the measurement of PI and the other materials. For PI, there is no distinct threshold and at 50 V, the transmission is decreased with only 15 %. Due to the strong memory anchoring, the material in the bulk layer has changed its director over a small angle toward the applied electric field, while the director at the surface is kept in its original direction. Since the prepared liquid crystal cells are very thin, the surface layer is important and prevents a complete rotation of the director. This results in a limited electro-optic response.

As expected the weaker anchoring of the other materials decreases the threshold voltage. Already at voltages of about 5 V, which is far below V_{th}, the transmission starts changing. Moreover, not only the liquid crystal in the bulk is able to rotate, also the director at the surface is reoriented. Therefore the change in transmission is larger.

Observation of the graphs shows sometimes two thresholds. The lowest threshold arises from the horizontal rotation of the director between the electrodes, while the second one stems from the reorientation above the electrodes.

b) Estimation of the azimuthal anchoring strength

For an estimation of the anchoring strength, transmission calculations of the in-plane switching mode of liquid crystals as a function of the applied voltage are compared with detailed microscope measurements.

In a region with a uniform director over an area larger than the gap between the electrodes, $g = 36$ µm in the prepared cells, the one-dimensional approximation of the in-plane switching mode of the liquid crystals as described in section 4.3 is valid. Electro-optic measurements in that region can be used for comparison with one-dimensional calculations. The optical transmission through the one-dimensional liquid crystal layer is calculated using the Jones Matrix Method.

The measurements are performed with a 10-bit CCD-camera on top of a polarizing microscope using a narrow bandpass filter for a wavelength of 600 nm. A uniform region of about 5×5 µm between two neighboring electrodes is selected in a LabView-program and for differ-

ent orientations of the crossed polarizers, the transmission is measured as a function of the applied voltage in the selected area.

For the prepared cells, the unknown parameter in (4.13) is the anchoring strength W_a. The anchoring directions $\phi(0)$ and $\phi(d)$ in the selected region are assumed equal and are obtained by rotation of the liquid crystal cell until a perfect black state is obtained. The corresponding surface coupling parameter ρ is found by fitting the calculated with the measured transmission characteristic.

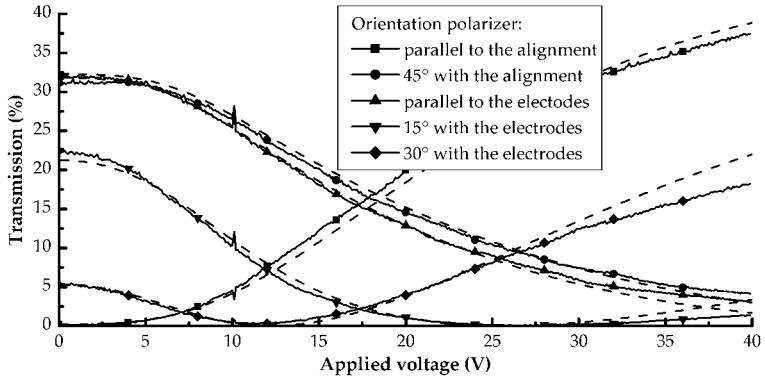

Figure 4.19: Electro-optic characteristic in a uniform region between neighboring electrodes of the BCB cell, measured (full lines) and calculated (dashed lines).

In Figures 4.19 the measured transmission curves are shown together with the calculated transmission curves for BCB. The alignment direction in the measured region makes an angle of $\phi_0 = 42°$ with the electric field and the best agreement between measurement and calculation is obtained for strong alignment $\rho = 0$, which corresponds with the expectations.

For the cell covered with PI and 3-GPS, the uniform regions are too small to perform a reliable measurement. Therefore, the anchoring strength can not be estimated with this method.

Although high voltages change the alignment of the FC4430 cell as shown in section 4.6.2, when using a limited voltage range the cell returns to its original state. This means that the azimuthal anchoring is not entirely degenerated. By measuring the electro-optic characteristic over a limited voltage range, the anchoring can thus be estimated. Figures 4.20 shows the measured and calculated electro-optic characteristics for the cell covered with FC4430. The alignment direction for

the measured region made an angle of 53.5° with the x-axis.

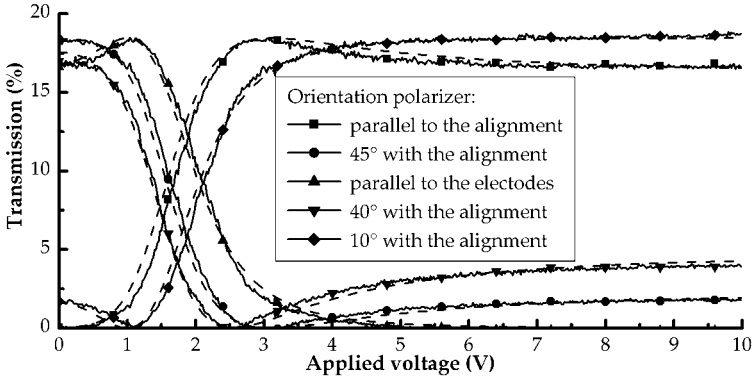

Figure 4.20: Electro-optic characteristic in a uniform region between neighboring electrodes of the FC4430 cell, measured (full lines) and calculated (dashed lines).

In in-plane switching liquid crystal devices, the threshold voltage scales linearly with the distance between the electrodes g. Although the electrode distance g is 36 μm, the threshold voltage for in-plane rotation of the cell covered with FC4430 is below 1 V and reaches a final distribution after only 5 V.

Electro-optic measurements were carried out for several regions in the FC4430 cell, with different directions of the alignment ϕ_0. The best comparison between the calculated and the measured characteristics is found for a reduced surface-coupling of $\rho = 40$, as illustrated for one measured region in Figure 4.7. This value of ρ corresponds with an azimuthal anchoring strength W_a of 3.6×10^{-7} J/m^2. This is in the range of weak anchoring (see Table 4.1) and is low compared to typical values found in literature [16, 93, 119]. Substitution of W_a in (4.19) gives a threshold voltage of 0.5 V, which corresponds with the threshold voltage observed in the measured transmission characteristics in Figure 4.20.

Although the measurement of the anchoring strength is demonstrated on non-rubbed surfaces exhibiting Schlieren textures, it is also applicable to surfaces with a homogeneous weak alignment. The threshold is the main parameter in the fitting procedure. In order to maximize the influence of the anchoring and increase the accuracy of the measurement, it is important to work with thin liquid crystal layers.

The simple one-dimensional method explained above with only one fitting parameter has been presented on the "XVI Conference on liquid crystals: Chemistry, Physics and Applications" (18-21 September 2005, Stare Jabłonki, Poland) [122] and is accepted for publication in proceedings of SPIE [123].

A similar technique is presented in [115]. In this paper, the average transmission is measured for a rubbed in-plane switching cell with narrow electrodes and gap ($w = g = 1$ μm). The measured data is compared with two-dimenional director and optical calculations. A two-parameter fitting procedure gives the final anchoring strength. Our method, as explained above, only needs one fitting parameter and uses much faster one-dimensional calculations of the director distribution and transmission.

Chapter 5

Liquid Crystal Device with a Rotatable Director

The in-plane switching mode of liquid crystal displays is based on the principle of a controllable wave plate. The director in the in-plane switching mode is originally oriented homogeneously along the rubbing direction with a small pretilt. The positive and negative electrodes form a pattern of parallel interdigitated stripes on the bottom glass substrate at a small angle with the rubbing direction. Applying a voltage to the electrodes generates an electric field that rotates the director in the plane parallel to the surface.

A wave plate is a commonly used item to control the polarization state of light in optical setups. Typical examples are a quarter-wave and a half-wave retardation plate. Extra functionality is added to the wave plate by a variable orientation of the optical axis. For classic wave plates, this requires a rotational stage. In devices, mechanical parts are a weak point and should therefore be avoided. Liquid crystals have unique features which make them the ideal candidate for electrically controllable wave plates. The orientation of the uniaxial axis of the birefringence can be controlled by an external electric field. This allows the implementation of a reconfigurable wave plate without the need of mechanical moving parts.

Although the in-plane switching mode has excellent characteristics for use in displays, its application as a controllable wave plate is limited due to some intrinsic features:

– At the top and bottom surface of the liquid crystal layer, the di-

rector is kept along the alignment direction. Therefore, the layer does not behave as a homogeneous layer rotated around the surface normal.

- In the area above the electrodes a strong vertical field is present, resulting in an inhomogeneous director distribution and loss of intensity due to diffraction.

- The rotation of the director in the in-plane switching mode is restricted between the rubbing direction and the electric field. The maximum change of the director twist angle is thus 90°.

- Removal of the applied electric field causes the director to return to its original orientation. Therefore, during operation the driving field must be applied continuously.

- The return to the ground state is relatively slow due to the absence of a field.

Only a few devices have been demonstrated in which the drawbacks of the in-plane switching mode as a reconfigurable wave plate were wholly or partly solved. Examples are the tristable nematic liquid-crystal device [103] which uses a patterned surface to obtain three stable alignments, the cartwheel cell [49, 124–126] in which electrode patterns are used to change the direction of the applied electric field and a device based on smectic layer reorientation in ferroelectric liquid crystals [127–129].

In this chapter a new multistable device is presented in which both switching and switching back are driven by an electric field. The device is based on patterned electrodes which allow to control the direction of the applied field. Switching is possible to three different directions and enables a 360° in-plane rotation of the director. The presented device can serve as a reconfigurable wave plate or as a pixel in display applications. The description of the device in the following sections will be mainly related to its function as a reconfigurable wave plate.

5.1 Structure of the reconfigurable wave plate

The new reconfigurable wave plate consists of a layer of hexagonal electrode pads below a stack of a dielectric layer with thickness d_0 and a

liquid crystal layer with thickness d, sandwiched between two glass substrates (Figure 5.1).

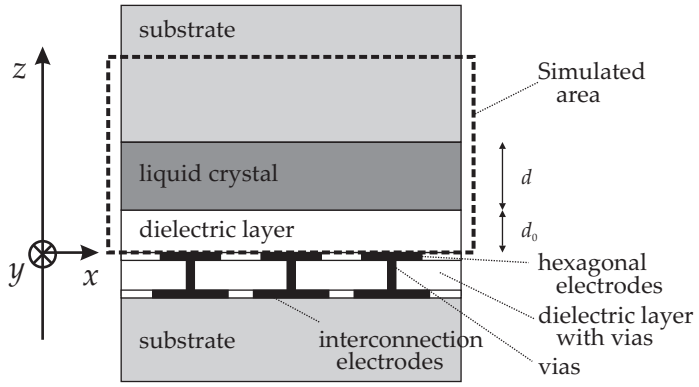

Figure 5.1: Setup of the reconfigurable wave plate with indication of the used coordinate axes. The area used in the three-dimensional director simulations is indicated with the dashed rectangle and contains the hexagonal electrodes (situated in the xy-plane) with on top a dielectric layer, a liquid crystal layer and the top substrate.

The hexagonal electrode pads are arranged in a two-dimensional array in the xy-plane as illustrated in Figure 5.2. The hexagons in the simulated device are of regular shape and have a side length a of 3 μm. The distance between two neighboring hexagons b is 5 μm. The electrodes are grouped in four sets, marked with different gray levels in Figure 5.2. The individual electrodes of each set are connected to a lower interconnection level through vias (metalized holes) in an insulating dielectric layer. An electric potential can be applied separately to each of the four groups.

At the top and bottom surface of the liquid crystal layer an azimuthally degenerated planar anchoring surface is used. This enables free in-plane rotation of the director.

5.2 Operating principle

The electrode topology described above, arranged in four sets of separately driven hexagonal pads, allows the implementation of a large variety of possible driving configurations. Here the study is restricted to the case in which the four sets are driven in pairs of two by two, so only

three driving configurations are obtained. The three cases are shown in Figure 5.3 and will be referred to as the driving configurations C_1, C_2 and C_3. The two gray levels in Figure 5.3 indicate different potentials. The electrodes with the same potential form parallel lines, comparable with the parallel electrodes of the in-plane switching mode of liquid crystals. Changing the driving configuration rotates the electrode lines and this rotates the liquid crystal director.

The local electric field can be decomposed into two components. A horizontal field, parallel to the xy-plane and a vertical field parallel to the z-axis. Between the parallel sides of two neighboring electrodes with different potential levels, the local horizontal electric field will be oriented approximately in the direction perpendicular to the parallel

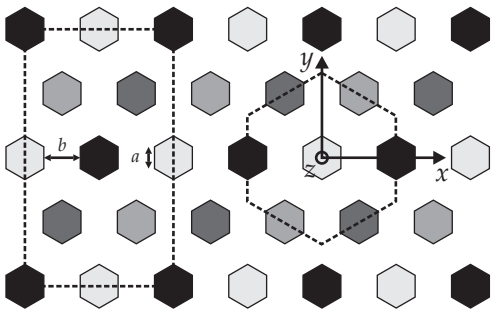

Figure 5.2: The hexagonal electrode pattern situated in the xy-plane. The four groups of electrodes are marked with different gray scales, with indication of a rectangular and a hexagonal building block.

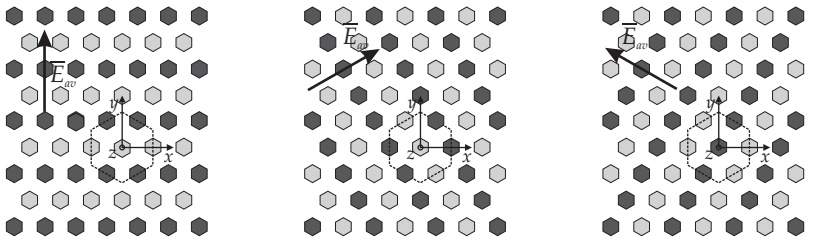

Figure 5.3: Three possibilities for driving the electrode sets two by two. The electrodes are situated in the xy-plane and the gray levels indicate different voltage levels. In each driving configuration, the direction of the average horizontal electric field $\overline{E}_{av}$ is indicated.

sides as represented in Figure 5.4. Taking into account that a liquid crystal makes no distinction between a positive or a negative electric field, it is clear from Figure 5.4 that the average horizontal electric field $\overline{E}_{av}$ is parallel to the y-axis. The liquid crystal director will therefore align on average in this direction. The direction of the average horizontal electric field $\overline{E}_{av}$ in driving configurations C_2 and C_3 can be found in a similar way and is indicated on Figure 5.3. The azimuthal direction of the average electric field $\overline{E}_{av}$ will be indicated with ϕ_{av} and is equal to 90°, 30° and 150° in respectively driving configuration C_1, C_2 and C_3.

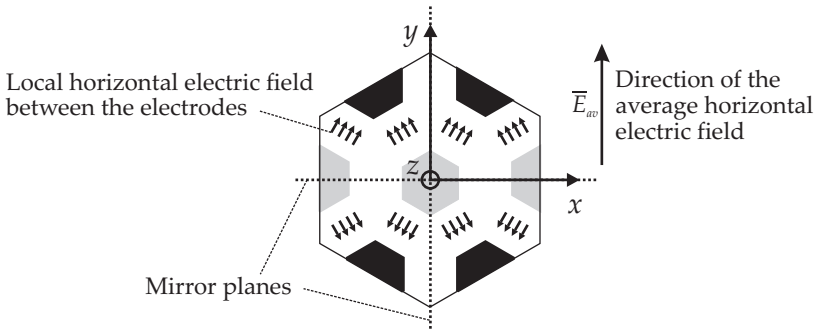

Figure 5.4: Indication of the approximate direction of the horizontal component of the local electric field between neighboring electrodes (represented by small arrows) and the average horizontal electric field $\overline{E}_{av}$ for driving configuration C_1. The mirror planes xz and yz are drawn as dotted lines.

Figure 5.4 also reveals that in the case of driving configuration C_1, the xz-plane and the yz-plane are mirror planes. For driving configurations C_2 and C_3, the mirror planes rotate compared to those shown in Figure 5.4 by ±60° around the z-axis. The mirror plane xz which contains the centers of the hexagonal electrodes at the same potential level, will be referred to as the equipotential mirror plane.

Due to the hexagonal configuration, the angle between the average electric field in two driving configurations is always 60°. Consequently, horizontal director rotation through an angle of 360° is possible, as shown schematically in Figure 5.5.

Consider for example the situation when C_2 is applied to a starting configuration with the director aligned in the y-direction at t_0. Applying C_2, causes the director to rotate clockwise toward the situation at t_1, making an angle of 60° with the positive y-axis. Now applying driv-

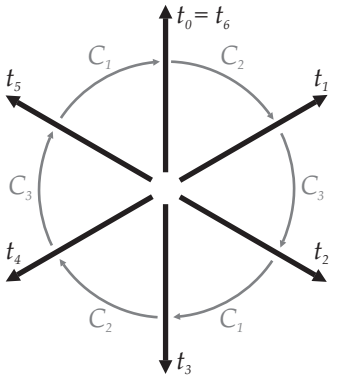

Figure 5.5: Illustration of the three directions along which the director can be aligned (opposite directions are physically equivalent) and the principle of a 360° director rotation by successive application of the three driving configurations.

ing configuration C_3 will rotate the director further toward t_2, another rotation of 60°. Finally, applying C_1 aligns the director again along the y-axis, but its orientation has undergone a 180° rotation. Successive application of C_2, C_3 and C_1 a second time results in the orientation at t_6. The director has returned to its original position after a 360° in-plane rotation.

5.3 Director simulations

Director simulations of the device have been performed using the dynamic three-dimensional Liquid Crystal Director Simulation tool MonLCD as described in section 2.3. Since the device is periodic, only a single building block needs to be used for three-dimensional simulations. The minimum modeling window is a hexagonal prism with a base as represented on Figure 5.2. Periodic boundary conditions are used on the opposing faces for the director and potential distribution. The side length of the base of the hexagonal building block is $2(a + b/\sqrt{3}) = 11.77$ μm.

In the simulations, it is assumed that the electric field due to the interconnection electrodes has a negligible influence on the director distribution. This is acceptable if the dielectric layer with vias is sufficiently thick. Therefore only the dashed rectangle in Figure 5.1 has

been simulated. The simulated volume contains the hexagonal electrode pads in the xy-plane, the uniform isotropic dielectric layer with thickness d_0, a liquid crystal layer with thickness d and a second thicker dielectric layer on top of the liquid crystal. The calculations are executed on an irregular mesh with 23066 tetrahedral elements and 4675 nodes, constructed with the commercial mesh generator GiD.

The nematic liquid crystal used in the simulations is E7 with the physical parameters as represented in Tables 2.2 and 3.1. The thickness d of the liquid crystal layer is chosen to be 2.1 μm. The top and bottom surfaces of the liquid crystal layer are modeled as planar azimuthally degenerated anchoring surfaces. The surface anchoring energy in the simulation tool is represented by equation (4.12) with the polar anchoring strength W_p equal to 5×10^{-6} J/m^2. For this thickness and the wavelength of a HeNe-laser (λ = 632.8 nm), the total retardation of the liquid crystal layer is about $3\lambda/4$. The liquid crystal layer acts thus as a quarter-wave retardation plate when used in transmission and a half-wave retardation plate when used in reflection.

The bottom dielectric layer used in the simulations has a thickness d_o of 1.3 μm and a dielectric constant ε = 3.5. The purpose of the bottom dielectric layer will be pointed out in the following sections.

At the top and bottom surface of the modeling window, the simulation tool MonLCD assumes a mirror plane for the potential distribution. The calculated local electric field is thus horizontal in the top and bottom plane. In the xy-plane containing the hexagonal electrodes, this is a good approximation. At the top surface of the liquid crystal layer on the other hand, the obtained fields are not horizontal. Therefore, a sparsely meshed dummy dielectric layer is added above the liquid crystal layer. At the top of the dummy layer, the calculated electric fields deviate from the real electric fields, but in the liquid crystal layer the electric field is calculated correctly. The dummy dielectric layer has a thickness of 4 μm and the dielectric constant of the top glass substrate ε = 8. It is present in all simulations, but left out of consideration in the discussions.

5.3.1 Simulated director distribution

Figure 5.6 illustrates the operation of the device, showing a 180° rotation of the director by successively applying the driving configurations C_1, C_2, C_3 and once again C_1, each for 250 ms. Originally at t = 0 ms,

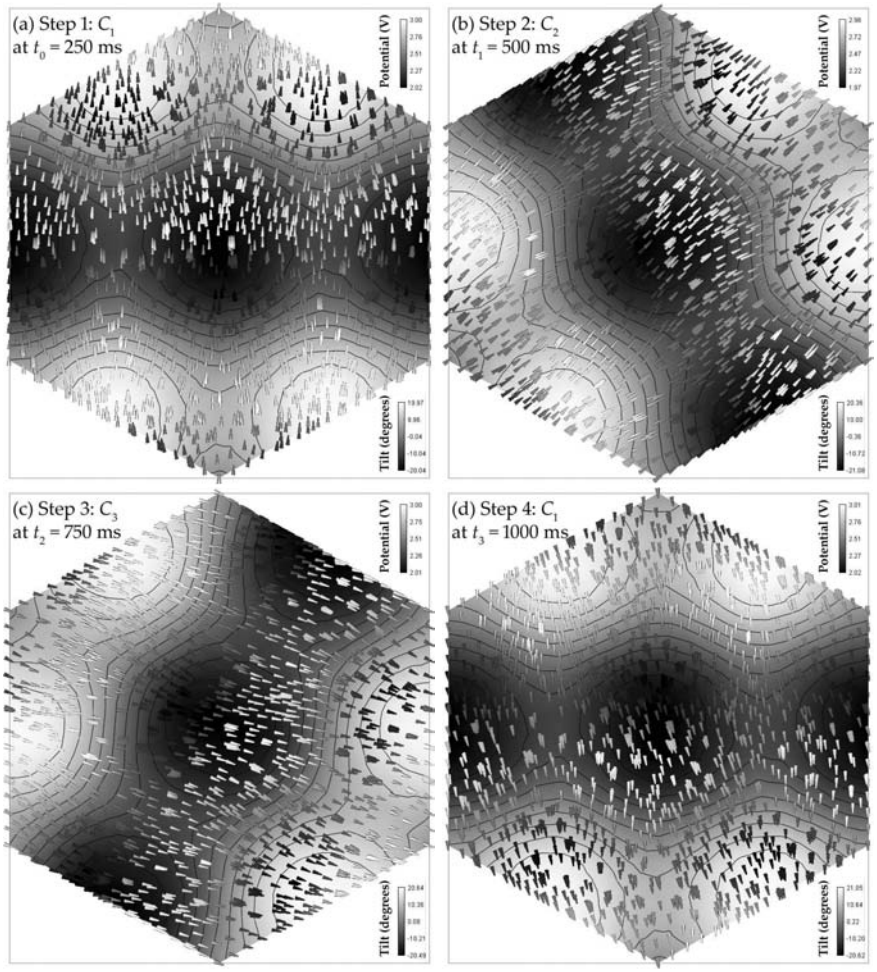

Figure 5.6: Simulation of a 180° director rotation by application of 4 consecutive driving configurations. The plots show the director and the potential distribution in the midplane of the liquid crystal layer (z = 2.35 μm in the coordinate system defined in Figures 5.1 and 5.2). The background color gives the potential variation (top right legend) with the equipotential lines. The small cones indicate the director distribution. The azimuth of the cones is an indication of the local director twist angle. The length and the color of the cones (bottom right legend) indicate the tilt angle. Plotted area: 20.4 × 23.5 μm.

the director is oriented parallel to the y-axis. The voltage applied to an electrode is 0 V or 5 V depending on the desired driving configuration.

The pictures show the orientation of the director as well as the electric potential distribution in the midplane of the liquid crystal layer, z = 2.35 μm, at the end of each time step in the sequence. The background shade indicates the potential distribution. Although the director orientations $\overline{n}$ and $-\overline{n}$ are physically equivalent, the director distribution is represented by cones. The shade and length of the cones indicate the director tilt angle, the azimuth corresponds with the twist angle. In this way, the difference between the director distribution in Steps 1 and 4 becomes visible. The director distributions in Step 1 at t_0 = 250 ms and Step 4 at t_3 = 1000 ms both show an average director orientation parallel to the y-axis. However, in step 4 the director is rotated over an angle of 180°. At the intermediate steps t_1 = 500 ms and t_2 = 750 ms, the average director orientation makes an angle of respectively 30° and -30° with the positive x-axis. Reapplying the sequence of driving configurations C_2, C_3 and C_1 results in reorientation of the director to the original direction at t_6 after a 360° rotation of the director.

Switching from one driving configuration to another only requires a rotation over an angle of 60°. Physically there is no difference between step 1 and 4. However, a limitation of the maximum rotation angle below 180° would, in certain cases, require a larger and more time consuming rotation. For example, a rotation from step 3 via step 2 back to step 1 would require a rotation of 120°.

Figure 5.7 shows the potential and director distributions across several horizontal cut planes through the hexagonal unit. In Figures 5.7(a) and 5.7(b) the potential distribution is shown in respectively the xy-plane at the bottom of the dielectric layer (coincident with the electrode pads) and the midplane of the dielectric layer. Figures 5.7(c) and 5.7(d) show the director profile at the bottom and the top of the liquid crystal layer. The distribution in the midplane of the liquid crystal layer was illustrated in Figure 5.6(b).

It is important to note that the local horizontal electric field (parallel to the xy-plane), given by the negative gradient of the potential distribution is not homogeneous and makes an angle with the average horizontal electric field. At first sight, the local horizontal electric field between two electrodes on different potential levels appears to orient along the normal to the hexagonal electrode edges, with an angle of

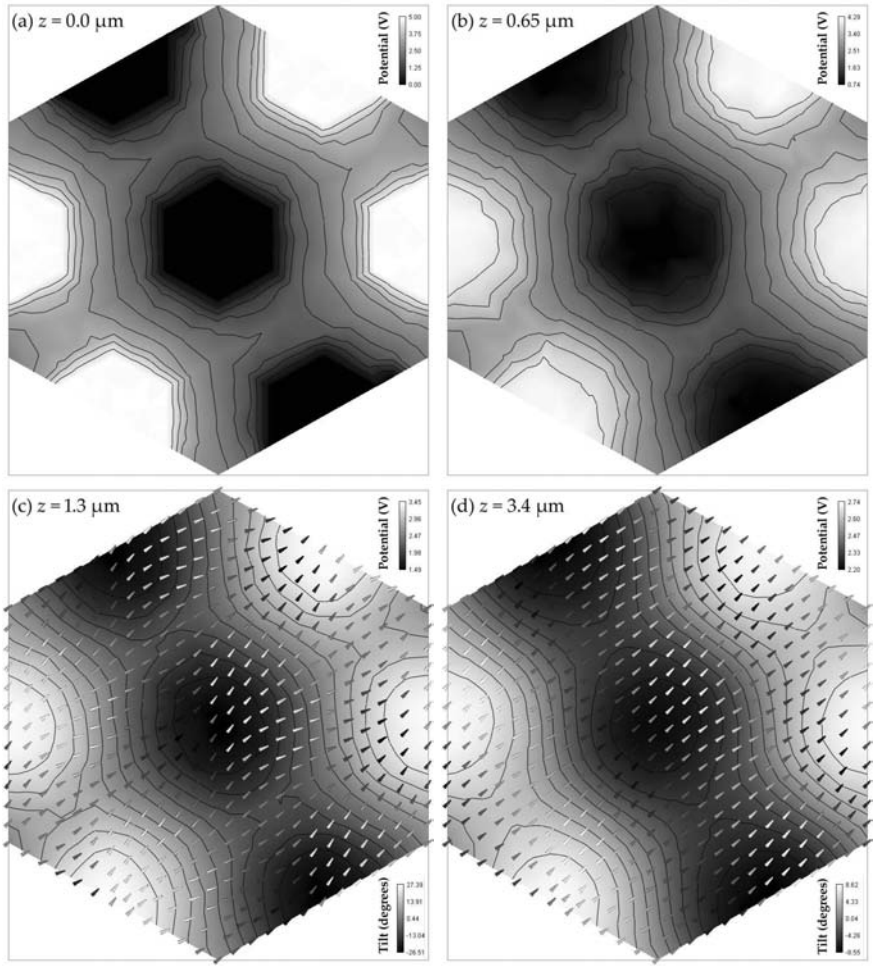

Figure 5.7: Director and potential distribution in different horizontal planes in the device at t_1 = 500 ms and driving configuration C_2 applied. Coordinate axes as defined in Figures 5.1 and 5.2. Indication of the potential and director distribution as in Figure 5.6. (a) z = 0.0 μm: the xy-plane containing the electrodes at the bottom of the dielectric layer (b) z = 0.65 μm: the plane in the middle of the dielectric layer (c) z = 1.3 μm: the bottom plane of the liquid crystal layer (d) z = 3.4 μm: the top plane of the liquid crystal layer. Plotted area: 20.4 × 23.5 μm.

±30° with respect to the average electric field as schematically drawn in Figure 5.4. After closer inspection of Figures 5.7(a) to 5.7(d) however, it is found that the angle between the local horizontal electric field and the average orientation is less than 30° at the bottom of the liquid crystal layer and decreases with increasing z. At the bottom of the liquid crystal layer the twist angle of the local director is spread across a range of almost ±30° about the desired direction, while in the volume above, the local director is aligned almost homogeneously along the average direction of the horizontal electric field.

5.3.2 Purpose of the dielectric layer

Near the electrodes, the vertical component of the electric field is strong. Figure 5.8(a) shows the director and the potential distribution in case the dielectric layer is absent and the liquid crystal layer is deposited directly on top of the hexagonal electrodes. The plot shows that without the dielectric layer, the director above the electrodes tilts to angles of almost 90°. When the applied voltage is removed, a tilt of 90° can result in the formation of domains separated by a defect line if the director in the adjoining regions relaxes in opposite directions.

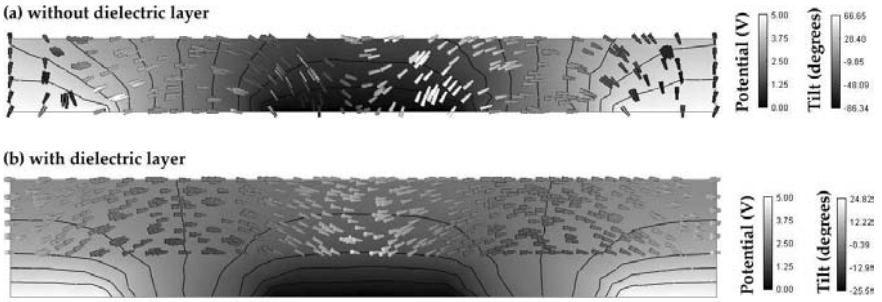

Figure 5.8: Distribution of the director and the potential in the xz-plane ($y = 0$ in Figure 5.2) at $t_1 = 500$ ms when driving configuration C_2 is applied. (a) without the dielectric layer (the liquid crystal layer is positioned directly above the electrodes, plotted area: 20.4×2.1 μm), (b) the device as described above with a dielectric layer of 1.3 μm inserted between the electrodes and the liquid crystal layer (plotted area: 20.4 × 3.4 μm).

Furthermore, the non-uniformity in the optical thickness of such a layer prevents its intended use as wave plate. In order to favor lateral

rotation instead of tilting, a dielectric layer is inserted between the electrodes and the liquid crystal layer. This layer shields the liquid crystal from the regions above the electrodes with strong vertical electric fields. Figure 5.8(b) shows that a more homogeneous distribution of the liquid crystal director is achieved when a dielectric layer is included. In the following, a dielectric layer is always included unless specified otherwise.

a) Simplified model for the influence of the dielectric layer

To illustrate the effect of the thickness and dielectric constant of the dielectric layer on the electric field in the liquid crystal, a simplified two-dimensional model with isotropic media is used, shown in Figure 5.9. An isotropic dielectric layer with dielectric constant ε_{d} is sandwiched between two infinite isotropic media with dielectric constant $\varepsilon_{\mathrm{lc}}$. Since the director tends to orient along the electric field, $\varepsilon_{\parallel}$ is used for the liquid crystal layer. In the middle of the dielectric layer, electrodes lines are present with alternating potential as in the in-plane switching mode of liquid crystals.

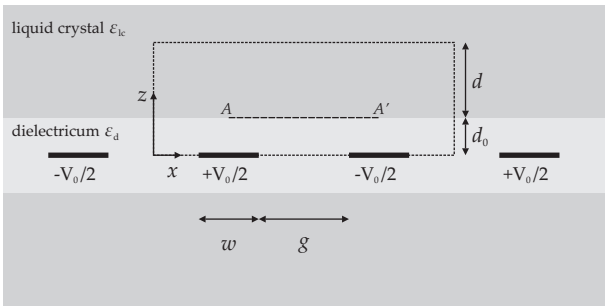

Figure 5.9: Simplified two-dimensional configuration which allows an analytic approximation of the field for the in-plane switching mode. Electrode stripes in a dielectric layer with thickness $2d_o$ between liquid crystal media.

Analytical calculation of the potential distribution in this configuration is not possible, but a simplification is possible by approximating the potential between two neighboring electrodes along the x-axis by a linear function as represented in Figure 5.10. In this case, separation of variables [130] can be used to solve the potential problem. The obtained

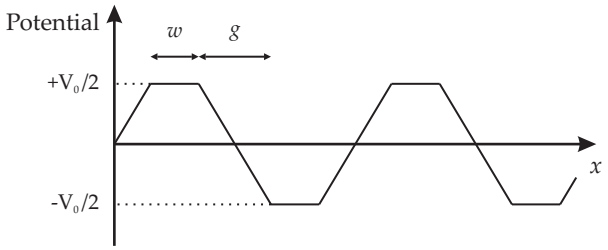

Figure 5.10: Potential variation along the x-axis in Figure 5.9 if the potential between neighboring electrodes is approximated by a linear function.

expression of the potential distribution is

$$z < d_o: \; V(x,z) = \sum_{n=1,3,\ldots}^{\infty} \left[A_n\, e^{\frac{n\pi z}{w+g}} + B_n\, e^{-\frac{n\pi z}{w+g}}\right] sin\left(\frac{n\pi x}{w+g}\right) \quad (5.1a)$$

$$z > d_o: \; V(x,z) = \sum_{n=1,3,\ldots}^{\infty} C_n\, e^{-\frac{n\pi z}{w+g}}\, sin\left(\frac{n\pi x}{w+g}\right) \quad (5.1b)$$

with

$$A_n = \alpha_n\,(\varepsilon_{\mathrm{d}} - \varepsilon_{\mathrm{lc}}) \quad (5.2a)$$

$$B_n = \alpha_n\, e^{\frac{2n\pi d_o}{w+g}}\,(\varepsilon_{\mathrm{d}} + \varepsilon_{\mathrm{lc}}) \quad (5.2b)$$

$$C_n = 2\alpha_n\, e^{\frac{2n\pi d_o}{w+g}}\,\varepsilon_{\mathrm{d}} \quad (5.2c)$$

$$\alpha_n = \frac{4\,V_0\;(w+g)\;sin\left(\frac{n\pi g}{2(w+g)}\right)}{g\,\pi^2\,n^2\left[(\varepsilon_{\mathrm{d}} - \varepsilon_{\mathrm{lc}}) + e^{\frac{2n\pi d_o}{w+g}}\,(\varepsilon_{\mathrm{d}} + \varepsilon_{\mathrm{lc}})\right]} \quad (5.2d)$$

Note that for $z = 0$, this expression is independent of the dielectric constants ε_{d} and $\varepsilon_{\mathrm{lc}}$ and $V(x,0)$ results in the function plotted in Figure 5.10. From the potential distribution $V(x,z)$, the electric field can be calculated as $\overline{E} = -\nabla V$.

The potential and electric field distribution, calculated in the dotted rectangle of Figure 5.9, is shown in Figure 5.11. The background color shows the potential distribution, with indication of the equipotential lines. The thick dashed lines represent the electric field lines. The width and spacing of the electrodes correspond with the width and spacing of the hexagonal electrodes: $w = \sqrt{3}a = 5.2$ μm and $g = b = 5$ μm. The

thickness of the dielectric layer is chosen the same as in the simulated hexagonal device of Figure 5.6: d_o = 1.3 μm. For the liquid crystal layer, only a layer with thickness d = 2.1 μm is represented in Figure 5.11. In Figure 5.11(a), the liquid crystal layer is positioned directly on top of the electrodes (d_o = 0 μm). In Figures 5.11(b) and 5.11(c), the dielectric layer is inserted.

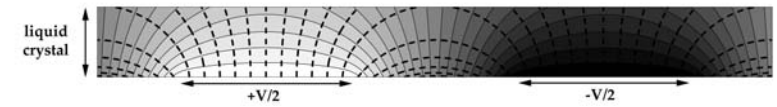

(a) without dielectric layer

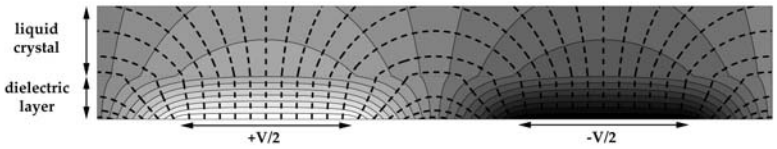

(b) with dielectric layer (ε_d = 3.5, ε_{lc} = 19.6)

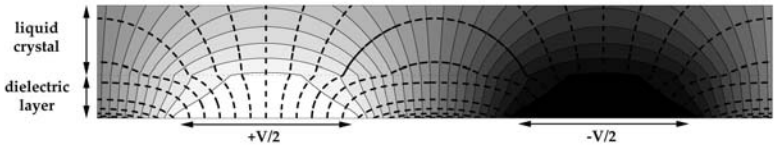

(c) with dielectric layer (ε_d = 19.6, ε_{lc} = 3.5)

Figure 5.11: Analytic approximation of the electric field lines (dashed) and equipotential lines (full) in the in-plane switching configuration for isotropic media. (a) liquid crystal directly deposited on the electrodes without dielectric layer (plotted area: 20.4×2.1 μm), (b) with a dielectric layer between the liquid crystal and the electrodes (plotted area: 20.4 × 3.4 μm), (c) with a high ε_d dielectric layer between the liquid crystal and the electrodes (plotted area: 20.4 × 3.4 μm).

The field lines which start or end at an electrode in Figure 5.11(a) are oriented perpendicularly to the surface. In the liquid crystal layer, this will lead to high tilt angles of the director. If the dielectric layer is inserted between the liquid crystal and the electrodes, the electric field at the bottom surface of the liquid crystal is no longer perpendicular. In Figure 5.11(b), ε_d = 3.5 and $\varepsilon_{lc} = \varepsilon_{||}$ = 19.6 is used as an approximation of the simulated device. Figure 5.11(c) represents a hypothetic case in which ε_d and ε_{lc} are interchanged compared to Figure 5.11(b).

Since $|\varepsilon_d - \varepsilon_{lc}|$ is large, the change in direction of the electric field

at the interface is quite large. Nevertheless, closer inspection of Figures 5.11(b) and 5.11(c) reveals that the direction of the electric field at the bottom surface of the liquid crystal layer looks similar, although ε_{d} and $\varepsilon_{\mathrm{lc}}$ were interchanged. Therefore, the electric field at the bottom of the liquid crystal layer is further inspected. From (5.1a), the electric field just above the interface between the two materials can be calculated as

$$\begin{aligned}\overline{E}\,(x, d_{o+}) \;=\; & \sum_{n=1,3,\ldots}^{\infty} \frac{-n\,\pi}{w+g}\, C_n\, e^{-\frac{n\,\pi\,d_o}{w+g}}\; cos\left(\frac{n\,\pi\,x}{w+g}\right) \overline{1}_x \\ & + \sum_{n=1,3,\ldots}^{\infty} \frac{n\,\pi}{w+g}\, C_n\, e^{-\frac{n\,\pi\,d_o}{w+g}}\; sin\left(\frac{n\,\pi\,x}{w+g}\right) \overline{1}_z. \end{aligned} \tag{5.3}$$

The magnitude $|\overline{E}|$ and the direction θ_e of the electric field $\overline{E}(x, d_{o+})$ just above the interface are plotted in Figure 5.12 as a function of the lateral position x for the three cases of Figure 5.11 and an applied voltage of 5 V. The direction of the field is given by its angle θ_e with the positive x-axis. The plot starts and ends above the centers of neighboring electrodes, illustrated by the line AA' in Figure 5.9. The location of the two halve electrodes below the line AA' is indicated with the thick black lines on the x-axis in Figure 5.12.

Between the electrodes, the three curves of the direction θ_e as a function of the lateral position x are almost identical. On the electrodes, the electric field for $d_0 = 0$ µm is perpendicular to the surface as expected. If a dielectric layer is inserted between the electrodes and the liquid crystal, the direction of the electric field just above the interface is not heavily influenced by the dielectric constant ε_{d}. The two plots with a dielectric layer in Figure 5.12 show an almost linear variation from +90° to -90°, but the strength of electric field in the liquid crystal layer decreases when lowering ε_{d}.

In Figure 5.13 the magnitude $|\overline{E}|$ and the direction θ_e are plotted for different values of the thickness d_o for an applied voltage of 5 V and the dielectric constants $\varepsilon_{\mathrm{d}} = 3.5$ and $\varepsilon_{\mathrm{lc}} = \varepsilon_{\parallel} = 19.6$. From the plots it is clear that the thickness d_o influences mainly the magnitude of the electric field. Once a dielectric layer is inserted, the direction of the electric field θ_e is hardly modified.

From Figures 5.12 and 5.13 follows that a low value of the thickness d_o and a high value of the dielectric constant ε_{d} are favorable for a high electric field in the liquid crystal layer.

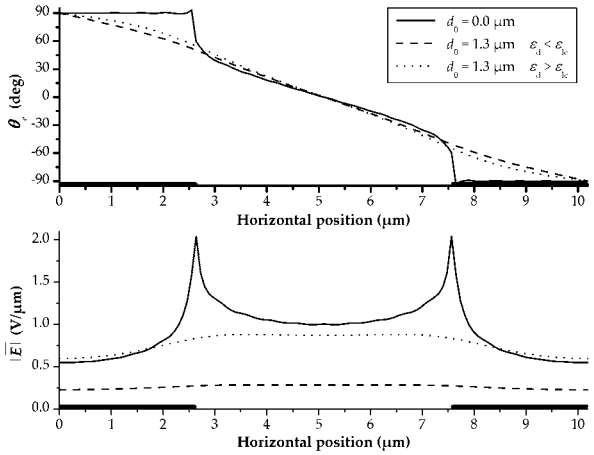

Figure 5.12: The angle θ_e with the x-axis (top) and the magnitude $|\overline{E}|$ (bottom) of the electric field $\overline{E}(x, d_{o+})$ just above the interface between the dielectric and the liquid crystal layer for the three cases of Figure 5.11.

The influence of the width w of the electrodes and the gap g is visible in Figure 5.14, which was calculated using an applied voltage of 5 V, a thickness $d_o = 1.3$ μm and dielectric constants $\varepsilon_{\mathrm{d}} = 3.5$ and $\varepsilon_{\mathrm{lc}} = \varepsilon_{\|}$. In the different plots the gap g between the electrodes is varied from 1 to 4 μm, but the distance $w+g$ is kept constant at 10 μm. The direction and strength of the electric field above the electrodes is hardly influenced, but in the center between the electrodes the strength of the the electric field increases for smaller gaps. Therefore, a small value of the gap g is favorable.

In the simulated hexagonal device of the previous section, a rather thick dielectric layer with a low dielectric constant is used. This seems unfavorable, since it reduces the strength of the electric field in the liquid crystal. The motivation to use a material with these properties was the easy and fast processing of the polymer BCB used in the experiments. The minimal reachable thickness by spinning without additional process steps is about 1 μm.

b) Mirror plane perpendicular to the average electric field

As explained in section 5.2, the orientation of the mirror planes depends on the driving configuration. Due to symmetry, the local elec-

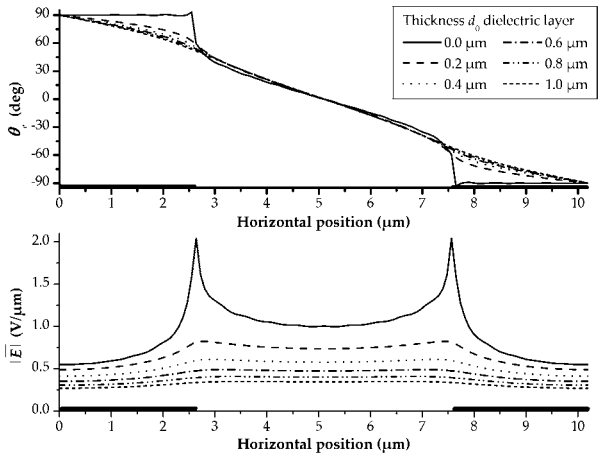

Figure 5.13: The angle θ_e with the x-axis (top) and the magnitude $|\overline{E}|$ (bottom) of the electric field $\overline{E}(x, d_{o+})$ just above the interface between the dielectric and the liquid crystal layer for different thicknesses of the dielectric layer, $\varepsilon_{\mathrm{d}} = 3.5$ and $\varepsilon_{\mathrm{lc}} = \varepsilon_{\parallel} = 19.6$.

tric field in the equipotential mirror plane (containing the centers of the hexagonal electrodes at the same potential level in Figure 5.4) should be parallel with the plane and thus perpendicular to the average horizontal electric field $\overline{E}_{av}$ of the driving configuration. To achieve a consistent director distribution, it is important that the director orientation does not follow the local electric field lines, but is determined by the elastic forces exerted by the liquid crystal director away from the plane.

In Figure 5.15, the director and potential distribution are shown in the equipotential mirror plane for different device configurations at $t_0 = 250$ ms with driving configuration C_1 applied. In Figure 5.15(a), the liquid crystal is positioned directly on top of the electrodes as in Figure 5.8. The director above the electrodes is almost perpendicular to the surface due to the strong vertical electric field in the mirror plane, only between the electrodes the director is oriented along the average electric field.

Introducing the dielectric layer in Figure 5.15(b) shows that the director becomes perpendicular to the mirror plane as desired. Since the director is perpendicular to the observed plane, only the white tips of the cones which represent the director are visible. Increasing the electrode width at the expense of the gap between them, increases the

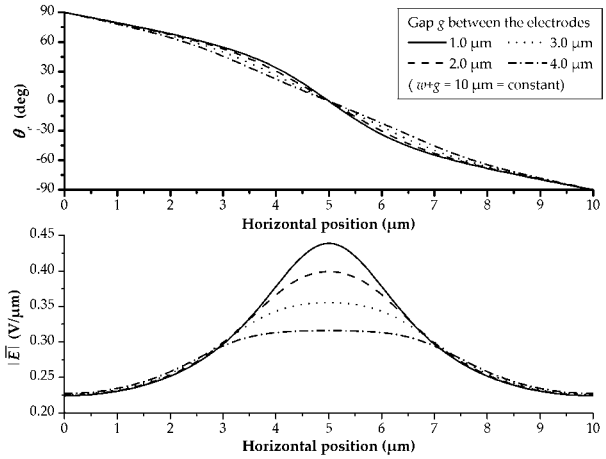

Figure 5.14: The angle θ_e with the x-axis (top) and the magnitude $|\overline{E}|$ (bottom) of the electric field $\overline{E}(x, d_{o+})$ just above the interface between the dielectric and the liquid crystal layer for different widths of the gap g between the electrodes, keeping the distance between the center of neighboring electrodes $w + g$ constant. (d_o = 1.3 μm, $\varepsilon_{\rm d}$ = 3.5 and $\varepsilon_{\rm lc} = \varepsilon_{\parallel}$ = 19.6)

strength of the electric field between the parallel rows of electrodes at equal potential that rotates the director in the plane parallel to the surfaces. Larger hexagons with reduced spacing are also favorable for a homogeneous director. They lower the horizontal variation of the potential in the equipotential mirror plane as shown in Figure 5.15(c) and thus weaken the horizontal electric field parallel in this plane. Therefore, the director is encouraged to follow the average horizontal electric field $\overline{E}_{av}$, perpendicular to the mirror plane.

For a dielectric layer with increased dielectric constant, the electric fields in the liquid crystal are stronger. As a result, the local director will follow closer the local electric field instead of the average electric field $\overline{E}_{av}$. Inside the equipotential mirror plane, the horizontal variation of the potential is larger as can be seen in Figure 5.15(d). At the same time, the electric fields away from the equipotential mirror plane are stronger and less along the average electric field. As a result, the director in the mirror plane follows less good the average director.

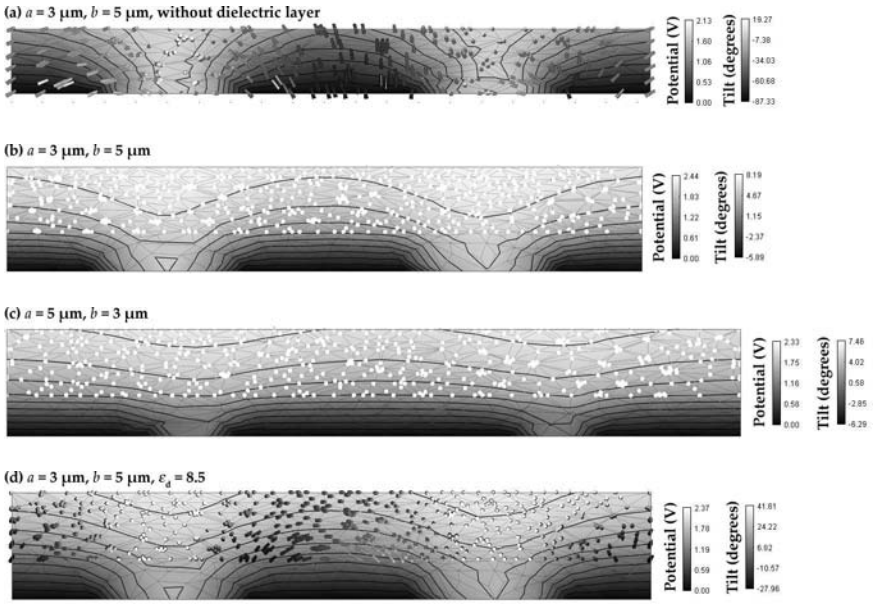

Figure 5.15: Distribution of the potential and the director in the equipotential mirror plane (xz of Figure 5.2), at $t_0 = 250$ ms with driving configuration C_1 applied. (a) without dielectric layer (plotted area: 20.4×2.1 μm), (b) with a dielectric layer ($d_0 = 1.3$ μm, plotted area: 20.4×3.4 μm), (c) with the same dielectric layer but larger electrode dimensions (plotted area: 23.3×3.4 μm), (d) with a dielectric layer with higher dielectric constant (plotted area: 20.4×3.4 μm)

5.3.3 Switching times of the device

In Figure 5.16 the evolution of the average twist ϕ_d is plotted versus time for a range of applied voltages from 1 to 10 V. The average twist ϕ_d is the mean value of the director twist angle at all nodes of the irregular mesh. The initial director orientation is chosen parallel to the y-axis (a twist of 90°) and the succeeding driving configurations $C_1-C_2-C_3-C_1-C_2-C_3-C_1$ were applied, each for a duration of 250 ms. The first period with C_1 applied is not strictly necessary since the director is already aligned along the y-direction. It is added to illustrate that the azimuthal angle of the average director in this configuration remains along the y-direction. The minimum voltage required to rotate the director over an angle of 360° is 4 V. Near the rotation threshold the total switching time is larger than 250 ms, but with increasing voltage the switching time

decreases.

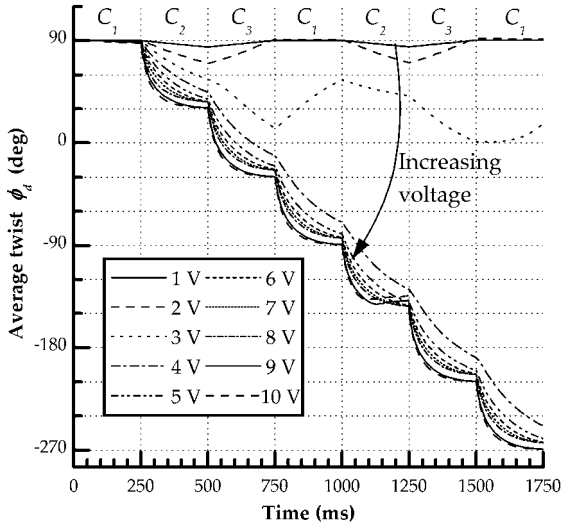

Figure 5.16: Variation of the average twist ϕ_d versus time for different voltages when applying the following sequence of driving configurations: C_1−C_2−C_3−C_1−C_2−C_3−C_1. Each driving configuration is applied for 250 ms, starting with the director aligned along the y-direction.

The evolution of the average twist ϕ_d from one driving configuration to the next follows approximately an exponential decay. Table 5.1 gives the time constant of the exponential decay, which is a measure of the device speed. In the top row of the first column, the time constant is given for the device with an applied voltage of 5 V. The reported time constant is quite large. However, a reduction of the time constant can be achieved by several means, as illustrated in the table. Increasing the driving voltage, as shown in the bottom row of the table, is an obvious means to lower the time constant. The stronger electric field results in a faster response of the liquid crystal. The dielectric layer lowers the electric field strength in the liquid crystal layer. Therefore reducing the thickness of the dielectric layer brings the liquid crystal closer to the electrodes and increases the field strength inside the liquid crystal layer, as illustrated in the second column. In the third column, the thickness of the dielectric layer d is kept the same as in the default case, but its dielectric constant ε is increased. In section 5.3.2.a was shown that this increases the strength of the electric field in the liquid crystal layer and thus leads to a faster response of the director.

Table 5.1: Time constant of the exponential decay of the average twist ϕ_d with 5 and 10 V applied. Column 1 gives the time constant for the proposed device (default): thickness of the liquid crystal layer $d = 2.1$ µm, thickness $d_o = 1.3$ µm and dielectric constant $\varepsilon_d = 3.5$ of the dielectric layer, dimensions and spacing of the hexagons $a = 3$ µm and $b = 5$ µm. Column 2 shows the effect of reducing the thickness of the dielectric layer and column 3 of increasing its dielectric constant. Column 4 shows the effect of a change in the dimensions of the hexagonal electrodes and their spacing.

	default	$d = 1.0$ µm	$\varepsilon_d = 8.5$	$a = 5$ µm $b = 3$ µm
5 V	117 ms	94 ms	49 ms	62 ms
10 V	36 ms	33 ms	24 ms	22 ms

With the default device configuration of Table 5.1, the tilt angle of the director is lower than 30° in the whole liquid crystal layer. For higher voltages, a higher dielectric constant or a thinner dielectric layer the tilt increases up to angles of 60° in certain regions. This has a profound effect on the homogeneity of the liquid crystal layer and thus on the applicability of the device as a reconfigurable wave plate. An alternative approach is to change the size and spacing of the hexagonal electrodes. In this case the time constant can be reduced without a significant increase in the average tilt angle as shown in the fourth column of Table 5.1. The polar anchoring parameter W_p practically does not influence the switching time, but it limits the tilt angle near the surface.

Table 5.2: Time constant of the exponential decay of the average twist ϕ_d for different thicknesses of the liquid crystal layer and applied voltages of 5 and 10 V. (All other parameters as in the default case of Table 5.1).

	1.0 µm	2.1 µm	3.0 µm
5 V	80 ms	117 ms	166 ms
10 V	33 ms	36 ms	56 ms

Changing the liquid crystal layer thickness also affects the switching speed. The electric field is the strongest at the bottom of the liquid crystal. For a thicker liquid crystal layer the time constant is expected to increase due to the weaker driving fields at the top. This agrees with the time constant behavior of other liquid crystal devices driven by horizontal electric fields [35]. Table 5.2 details the influence of the liquid

crystal layer thickness on the speed of the device. For operation as a wave plate, a certain optical phase retardation is required and changing the thickness of the liquid crystal layer is then not an option.

Finally it is interesting to note that the liquid crystal parameters are not critical to the device operation. In Table 5.3 the switching time constant is compared for a number of different liquid crystal materials. The parameters of these liquid crystals differ over a broad range [10, 11, 32], but the time constants remain similar. The dominant influence on the time constant is the rotational viscosity γ_1. For the liquid crystals 6CHBT and 5CB, γ_1 is significantly lower, leading to smaller time constants.

Table 5.3: Time constant of the exponential decay of the average twist ϕ_d for different liquid crystals and applied voltages of 5 and 10 V. (All other parameters as in the default case of Table 5.1).

	E7	ZLI-4792	5PCH	6CHBT	5CB
5 V	117 ms	115 ms	112 ms	88 ms	82 ms
10 V	36 ms	45 ms	37 ms	33 ms	30 ms

5.3.4 Multistable wave plate

Figure 5.17 illustrates the multistable behavior when the applied voltage of 5 V is removed after driving configurations C_1, C_2 or C_3 are applied. The variation of the average twist ϕ_d together with the variation of the maximum and minimum twist angle of the liquid crystal layer is plotted as a function of time. The time is measured relative to the instant where the driving voltage is removed. After 100 ms the director distribution relaxes to an orientation parallel to the surface along the average direction of the last driving configuration that was applied. The average direction of the director ϕ_d remains almost constant, however this direction is not exactly at an angle of $\pm 30^\circ$ as expected. Figure 5.16 shows that a final direction closer to the desired angle is achieved by increasing the applied voltage or driving for a longer time. The evolution of the maximum and minimum twist gives an indication of the speed of the relaxation process and the homogeneity of the twist.

Relaxation is the most critical process in the device. In the simulations, azimuthally degenerated anchoring surfaces have been used to model the director alignment at the top and bottom surface of the liq-

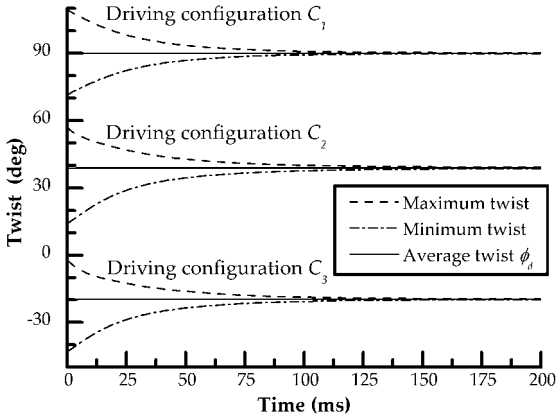

Figure 5.17: Evolution of the maximum, minimum and average twist as a function of time after removing the applied voltages in the driving configurations C_1, C_2 and C_3.

uid crystal layer. In practice, some residual azimuthal anchoring can be present due to memory alignment. Relaxation after switching of the applied voltages will in this case not result in a homogeneous layer along the average twist ϕ_d, but in a return to the direction specified by the alignment ϕ_0. Simulations have shown that with a weak azimuthal anchoring strength along the y-axis ($W_a = 1 \times 10^{-6}$ J/m^2), in-plane rotation is still possible but the threshold voltage and the time constant for rotation are increased.

5.4 Optical simulations

5.4.1 General considerations

In this section the optical characteristics of the proposed reconfigurable wave plate are examined. Before discussing the results, two side aspects of the optical simulations are treated.

a) Director distribution on a regular rectangular mesh

The optical algorithms explained in chapter 3 require a regularly meshed, rectangular prism as building block. This mesh is created by interpolating the director twist and tilt distribution on the irregularly

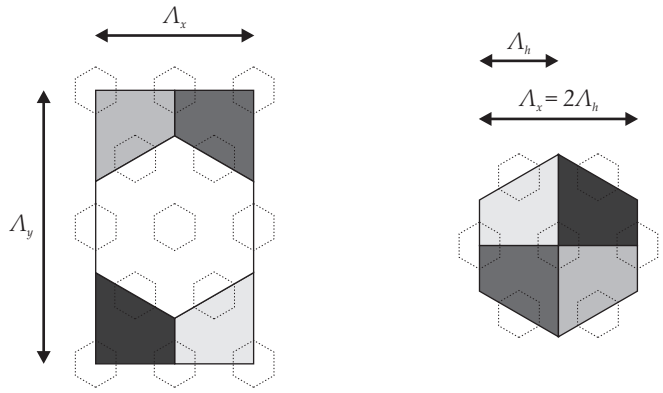

(a) Base of the rectangular building block

(b) Base of the hexagonal building block

Figure 5.18: Relation between the rectangular and hexagonal building block of Figure 5.2. The location of the hexagonal building block is indicated with a white background in the rectangular period, the other matching areas are indicated with the same gray level.

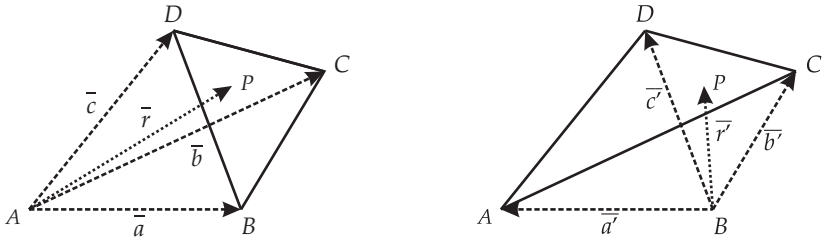

(a) Non-orthogonal basis ($\overline{a}$,$\overline{b}$,$\overline{c}$) inside the tetrahedron *ABCD* with *A* as origin

(b) Non-orthogonal basis ($\overline{a'}$,$\overline{b'}$,$\overline{c'}$) inside the tetrahedron *ABCD* with B as origin

Figure 5.19: Construction of two non-orthogonal bases inside each tetrahedron of the irregularly meshed hexagonal building block.

meshed hexagonal building block. The base of both the rectangular and the hexagonal building block are represented in Figure 5.2. Their relation is illustrated in Figure 5.18. Depending on the location in the rectangle, a different region inside the hexagon must be chosen. The dimensions of the rectangular period in the x and y-direction are respectively $\Lambda_x = 2(\sqrt{3}a + b)$ and $\Lambda_y = 4(a + b/\sqrt{3})$.

The hexagonal prism used as building block in the director simulations is constructed by filling the volume with tetrahedrons. To

find in which tetrahedron a point P of the regular mesh is located, two local non-orthogonal bases are chosen for each tetrahedron. The two bases use a different corner point of the tetrahedron as origin. In Figure 5.19(a), basis $(\overline{a}, \overline{b}, \overline{c})$ for tetrahedron $ABCD$ is drawn using A as origin. The second basis $(\overline{a'}, \overline{b'}, \overline{c'})$, illustrated in Figure 5.19(b), is constructed on the same tetrahedron but with B as origin. The basis vectors are calculated by subtraction of the coordinates of their endpoints.

Finding in which tetrahedron a point P is located, requires checking the position of P with respect to all the tetrahedron bases, one by one. Each point P in space has two place vectors $\overline{r}$ and $\overline{r'}$ with respect to the two different bases of the considered tetrahedron. The place vectors can be decomposed as a linear superposition of the respective basis vectors. If the obtained coefficients α, β and γ for the first basis and α', β' and γ' for the second basis are all positive, it is sufficient to conclude that P lies inside the considered tetrahedron. In that case the twist ϕ_P and tilt θ_P in P are approximated by a linear combination of the tilt and twist in the tetrahedron corners.

$$\phi_P = \phi_A + \alpha(\phi_B - \phi_A) + \beta(\phi_C - \phi_A) + \gamma(\phi_D - \phi_A) \quad (5.4a)$$

$$\theta_P = \theta_A + \alpha(\theta_B - \theta_A) + \beta(\theta_C - \theta_A) + \gamma(\theta_D - \theta_A) \quad (5.4b)$$

b) Diffraction orders on a rectangular and a hexagonal lattice

Although the device exhibits a hexagonal lattice, the optical calculations are executed on rectangular period. The directions of the diffraction orders in air are given by their wave vector. The components of the wave vector in the xy-plane are given by the Bloch-Floquet theorem [4]: $\overline{k}_{xy,mn} = m\overline{K}_x + n\overline{K}_y$ with $|\overline{K}_x| = 2\pi/\Lambda_x$, $|\overline{K}_y| = 2\pi/\Lambda_y$ and $m, n = 0, \pm1, \pm2, \ldots$ The loci of the vectors $\overline{k}_{xy,mn}$ are represented in the xy-plane on Figure 5.20. The zero diffraction order ($m = n = 0$) corresponds with the large filled circle in the center.

Due to the symmetry in the rectangular period (Figure 5.2) and the existence of a smaller hexagonal unit cell, lots of diffraction orders vanish. The hexagonal lattice is determined by the periodicity of the director distribution. Note that this periodicity is determined by the distance $\Lambda_h = \Lambda_x/2 = \sqrt{3}a + b$ between the center of two neighboring hexagonal electrodes in the xy-plane. The appearing diffraction orders can be found by using the wave vectors of the hexagonal lattice $\overline{K}_{h,x}$ and $\overline{K}_{h,xy}$, respectively parallel to and at an angle of 60° with the x-

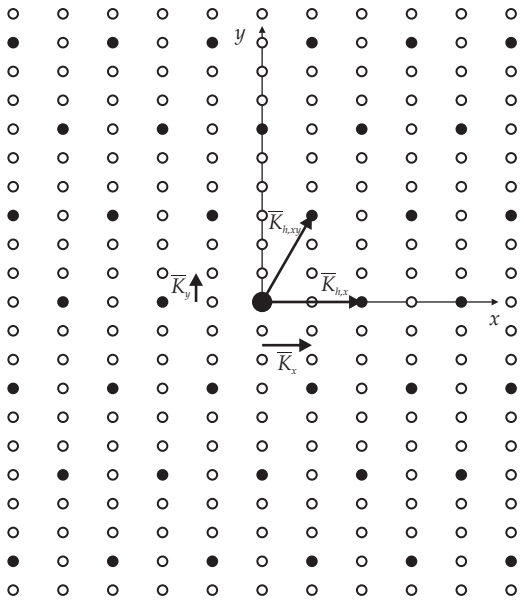

Figure 5.20: Wave vectors of the diffraction orders used in the optical calculations of the Rigorous Coupled Wave Method (all circles) and the diffraction orders of the hexagonal lattice (only the filled circles), represented in the xy-plane.

axis as indicated in Figure 5.18 and with $|\overline{K}_{h,x}| = |\overline{K}_{h,xy}| = 2\pi/\Lambda_h$. The non-disappearing diffraction orders are located at $\overline{K}_h = m\overline{K}_{h,x} + n\overline{K}_{h,xy}$ with $m, n = 0, \pm 1, \pm 2, \ldots$ and are indicated with the filled circles in Figure 5.20.

The angle between the propagation direction of the zero order diffraction (parallel to the z-axis) and the propagation direction of the first appearing order of the hexagonal lattice in air is 5.8° for the electrode dimensions $a = 3$ μm and $b = 5$ μm used in the previous sections.

In the optical simulations, the results of the Rigorous Coupled Wave Method will be compared with those of the simplified optical simulation algorithm based on the Jones Matrix Method. The number of diffraction orders used in the optical calculations using the Rigorous Coupled Wave Method for the x and y-direction is respectively 5 and 10, which corresponds with all 231 orders represented in Figure 5.20. Additional calculations have shown that an increased number of diffraction orders does not change the result.

c) Transmissive and reflective mode

The goal of the device is to act as a wave plate. In principle, it can be used in transmission as well as in reflection. Therefore, the optical transmission of the layer placed between crossed polarizers as well as the reflection with a single polarizer on top are examined. The transmissive mode, represented in Figure 5.21(a), is discussed first. The aim is to give an idea of the influence of the inhomogeneity of the liquid crystal layer on the optical properties. Afterward the reflective mode as represented in Figure 5.21(b) is treated.

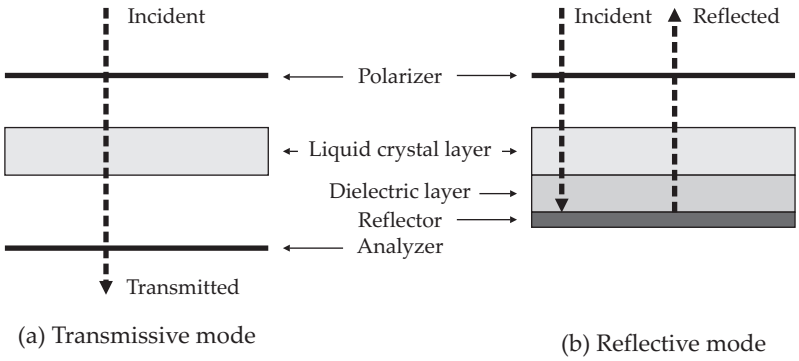

Figure 5.21: Different layers in the optical simulations of the reconfigurable wave plate. (a) transmissive mode, (b) reflective mode.

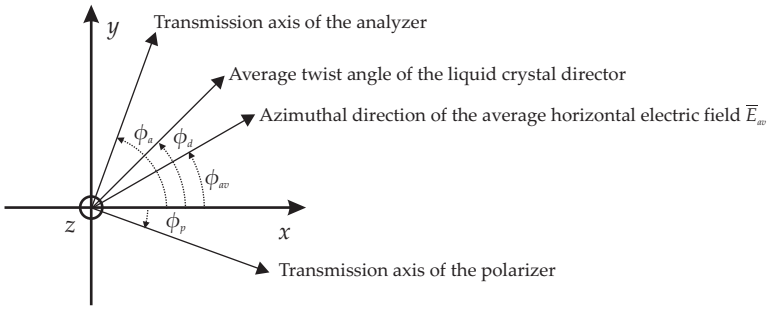

Figure 5.22: Definition of the different azimuthal angles ϕ_d, ϕ_{av}, ϕ_p and ϕ_a used during the optical simulations.

During the optical calculations, different azimuthal directions will be important. Therefore, the occurring angles are briefly recapitulated and indicated on Figure 5.22:

- ϕ_{av} is the azimuthal angle of the average horizontal electric field $\overline{E}_{av}$ (Figure 5.3). In the driving configurations C_1, C_2 and C_3, the angle ϕ_{av} is respectively equal to 90°, 30° and 150°.

- The average twist angle ϕ_d is the mean value of the director twist angle in the liquid crystal layer and indicates the azimuthal orientation of the average director. Ideally, after applying a driving configuration for a sufficiently long time, ϕ_d should become equal to ϕ_{av}.

- ϕ_p is the azimuthal angle of the polarizer transmission axis.

- In case a second polarizer is used, ϕ_a indicates the azimuthal angle of the transmission axis of the analyzer.

5.4.2 Transmissive mode

For the optical calculations in the transmissive mode, the electrodes are assumed to be transparent. The reconfigurable wave plate is positioned between crossed polarizers as illustrated in Figure 5.21(a). The orientation of the crossed polarizers in the calculations will be indicated by the azimuthal angle of the polarizer transmission axis ϕ_p. The orientation of the analyzer ϕ_a is then assumed $\phi_p + 90°$. The unpolarized incident light, with a wavelength λ of 632 nm, is normally incident on the top of the liquid crystal layer. The isotropic layers, such as the dielectric layer and glass substrates are not taken into account during the calculations.

To avoid the influence of interference and reflection in the polarizers, the polarizers are idealized in the calculations. In the Rigorous Coupled Wave Method, ideal polarizers are handled as a birefringent layer with complex refractive indices $n_o = 1.0$ and $n_e = 1.0 - i\,1.5\ 10^{-3}$ and thickness 1 mm. Since $n_o \approx n_e \approx 1$, interference and reflection at the polarizers surfaces are negligible. The large thickness of the polarizer layer d/λ in combination with the small imaginary part of the refractive index n_e ensures a complete absorption of the extra-ordinary wave.

a) Transmission through the wave plate between crossed polarizers

In Figure 5.23, the transmission is plotted as a function of the polarizer orientation ϕ_p for the director distributions illustrated in Figure 5.6 at time steps t_0, t_1, t_2 and t_3 with 5 V applied. The optical calculations are

performed using the Rigorous Coupled Wave Method. The transmission is given relative to the intensity of the incident unpolarized light.

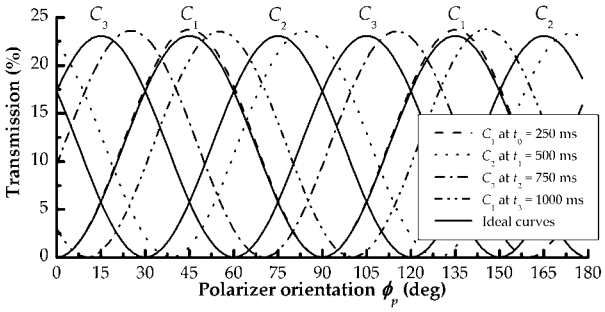

Figure 5.23: Transmission through the reconfigurable wave plate between crossed polarizers as a function of the polarizer orientation ϕ_p. calculated with the Rigorous Coupled Wave Method at $t_n = n\,250$ ms with $n = 0, 1, 2, 3$ in Figures 5.6 and 5.16 with 5 V applied.

The zero order transmission as well as the ideal transmission are plotted. The ideal transmission assumes a homogeneous birefringent layer, with the uniaxial axis horizontal at the azimuthal direction $\phi_{av} = 90°$, 30° and 150° for respectively driving configuration C_1, C_2 and C_3. The plots of the ideal transmission are sinusoidal and the different driving configurations are indicated by C_1, C_2 or C_3 at the polarizer orientations where their transmission should reach a maximum.

The incident light is unpolarized, therefore 50 % of the intensity is absorbed at the polarizer. The retardation of the homogeneous liquid crystal layer is approximately $3\lambda/4$, if the polarizer orientation ϕ_p makes an angle of 45° with the uniaxial axis at ϕ_{av}, the linear polarization is transformed into circularly polarized light and half of the remaining intensity is absorbed in the analyzer. This leaves a maximum transmission of 25 %. The ideal plots in Figure 5.23 reach a maximum transmission of approximately 23 %. The remaining difference of 2 % is due to the Fresnel reflections, calculated by equation (3.10), at the interfaces between the air and the liquid crystal.

The zero order transmission corresponds with the sum of the intensity of the modes that propagate further along the surface normal. The plots for the zero order transmission are also sinusoidal as a function of ϕ_p. The curve at t_0 follows closely the ideal plot, while the others are shifted about 9° to the right compared to the plots of the ideal transmission. The deviation of the polarizer orientation with maximum

transmission for the curves at t_1, t_2 and t_3 rises from the rotation process of the director. When switching to another driving configuration, the average director ϕ_d should make a clockwise rotation of 60°. For the sinusoidal transmission curves of Figure 5.23, this implies a shift of 60° toward the negative x-axis. At t_1, t_2 and t_3, the reorientation of the director to the driving configuration did not yet reach the desired orientation, as was previously shown in Figure 5.16. Only at t_0, the average director twist ϕ_d is equal to the desired value $\phi_{av} = 90°$. The average director twist ϕ_d at $t_1 = 500$ ms for the 5 V plot in Figure 5.16 is 39°, thus still 9° above the desired value ϕ_{av} of 30° in driving configuration C_2. The value of ϕ_d at $t_1 = 500$ ms corresponds with the location of the first minimum of the transmission at $\phi_p = 39°$ of the plot for t_1 in Figure 5.23. This indicates that for the zero order transmission, the reconfigurable wave plate acts as a homogeneous wave plate with the uniaxial axis oriented along the average director twist angle ϕ_d.

For further optical calculations, a director simulation is used in which the three different driving configurations are applied during a longer time, to ensure an equilibrium state for the director with the average twist angle ϕ_d along the desired direction ϕ_{av}. The transmission obtained for the three driving configurations in the equilibrium state with applied voltages of 5 and 10 V are plotted in Figure 5.24 together with the ideal transmission as a function of the polarizer orientation ϕ_p. In this new plot, the positions of the minima and maxima coincide. All further optical calculations will use the equilibrium director distributions, unless specified otherwise.

The transmission as a function of the polarizer orientation ϕ_p in Figure 5.24 is calculated for both the Rigorous Coupled Wave Method and the Jones Matrix Method. Comparison of both shows a very good agreement between the two algorithms. It seems strange that the ideal transmission for both methods is not identical, but this small deviation comes from neglecting internal Fresnel reflections in the Jones Matrix Method.

The plotted results look very promising. In the three driving configurations, the reconfigurable wave plate acts as a homogeneous layer between crossed polarizers. For each of the three driving configurations, the zero order transmission is a sinusoidal function of ϕ_p. The maxima for the three driving configurations are located at the expected locations, 60° apart. In between, total extinction is obtained for the zero order transmission if the average director twist ϕ_d is oriented parallel

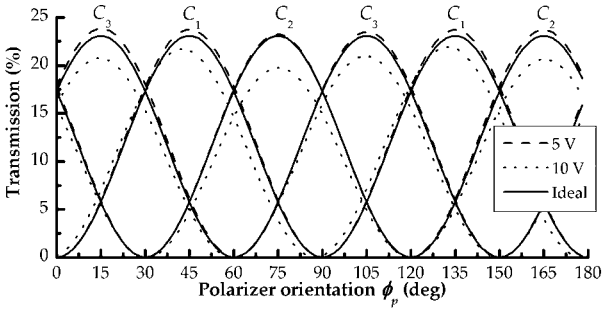

(a) Calculated with the Rigorous Coupled Wave Method

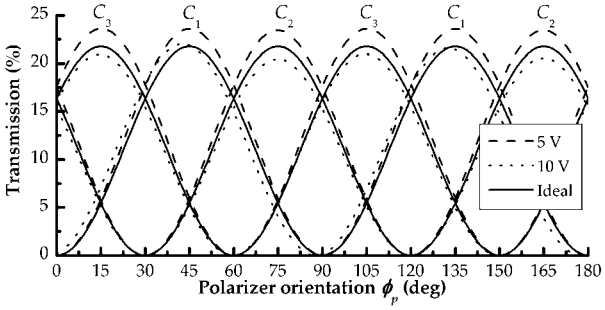

(b) Calculated with the Jones Matrix Method

Figure 5.24: The zero order transmission through the reconfigurable wave plate positioned between crossed polarizers, as a function of the polarizer orientation ϕ_p in the three different driving configurations.

or perpendicular to ϕ_p.

The plots for 5 V follow almost exactly the ideal curve, while the plots for 10 V have a slightly lower transmission. The reduced transmission for 10 V is caused by diffraction. The influence of diffraction is investigated for driving configuration C_2 in Figures 5.25 and 5.26. The result for the other driving configurations is similar and therefore omitted for the clearness of the graph.

The four curves show the ideal transmission, the zero order transmission, the total transmission and the overall intensity of all non-zero diffraction orders as a function of the polarizer orientation ϕ_p. The total transmission is the sum of the intensity of all diffraction orders, including those responsible for the zero order transmission. The overall intensity of all non-zero diffraction orders is calculated as the difference between the total and the zero order transmission.

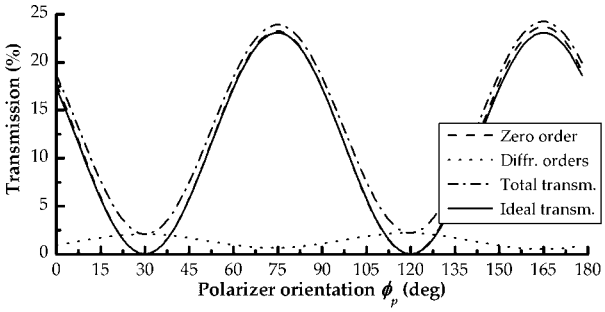

(a) Calculated with the Rigorous Coupled Wave Method

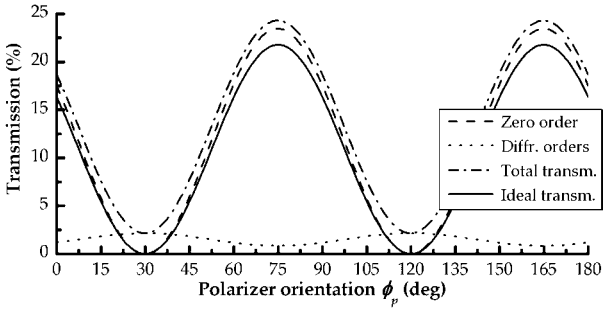

(b) Calculated with the Jones Matrix Method

Figure 5.25: Transmission through the reconfigurable wave plate positioned between crossed polarizers as a function of the polarizer orientation ϕ_p for driving configuration C_2 and an applied voltage of 5 V.

While the zero order transmission reaches full extinction when the polarizer transmission axis is oriented parallel or perpendicular to the average twist ϕ_d, the total transmission still has some light leakage from the non-zero diffraction orders. This is inevitable since the director is not perfectly along the desired orientation. Due to the limited variation of the liquid crystal director in the layer, the total intensity of all non-zero diffraction orders stays below 2.5 % for an applied voltage of 5 V.

With 10 V applied as in Figure 5.26, the influence of diffraction is certainly not negligible. The total intensity of the diffraction orders varies from 5 to 10 %. Though, extinction is still obtained at the polarizer orientations parallel and perpendicular to the average twist. Thus for the zero order transmission, the layer still behaves as a homogeneous birefringent layer.

A last important thing to note is that although the layer is not ho-

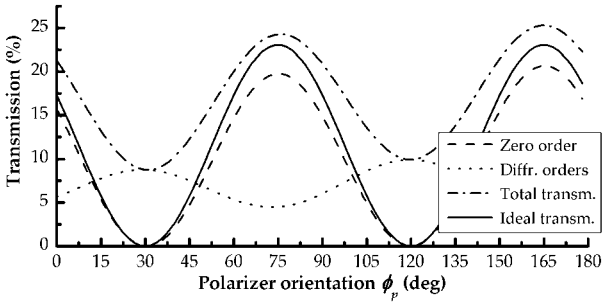

(a) Calculated with the Rigorous Coupled Wave Method

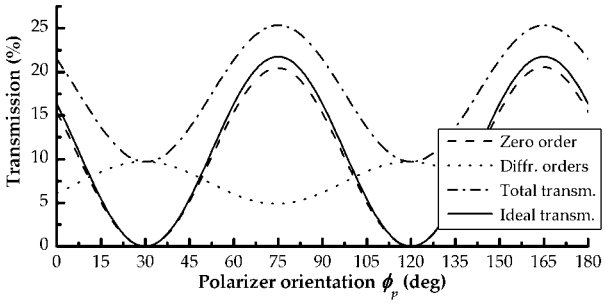

(b) Calculated with the Jones Matrix Method

Figure 5.26: Transmission through the reconfigurable wave plate positioned between crossed polarizers as a function of the polarizer orientation ϕ_p for driving configuration C_2 and an applied voltage of 10 V.

mogeneous and diffraction is important, the results of the Jones Matrix Method and the Rigorous Coupled Wave Method agree very well when applying 10 V. Not only, the plot for the average corresponds very well, but also the other curves. This again shows the usefulness of the simplified optical transmission algorithm based on the Jones Matrix Method.

b) Influence of the applied voltage

In a homogeneous birefringent layer, an increasing tilt angle causes a decrease of the retardation for normally incident light. For the homogeneous liquid crystal layer in the simulations above, the retardation is about $3\lambda/4$. A decrease in retardation would mean changing toward a half wave plate and thus, for the polarizer transmission axis oriented at an angle of 45° with the director, the transmission increases.

It was shown in the previous section that for the zero order transmission, the inhomogeneous liquid crystal of the reconfigurable wave plate behaves as a homogeneous layer with the director horizontally along the average twist. Higher voltages applied to the reconfigurable wave plate diminish the homogeneity of the liquid crystal layer by creating regions with larger tilt angles. Therefore, it is expected that the retardation experienced by the zero order transmission would decrease with increasing voltage and consequently the maximum of the zero order transmission should increase.

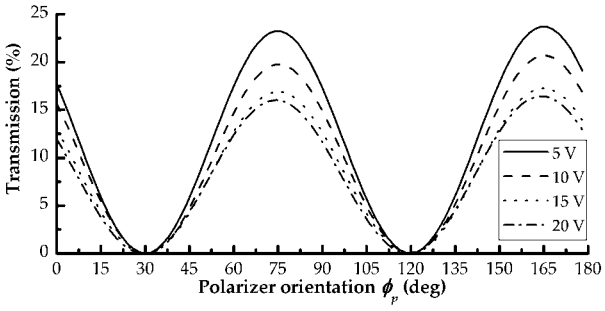

Figure 5.27: The zero order transmission through the reconfigurable wave plate positioned between crossed polarizers, calculated with the Rigorous Coupled Wave Method as a function of the polarizer orientation ϕ_p for driving configuration C_2 with applied voltages of 5, 10, 15 and 20 V.

This is in contradiction with the results of the simulated zero order transmission in Figure 5.27. The zero order transmission is plotted as a function of the polarizer orientation ϕ_p for applied voltages varying from 5 to 20 V in driving configuration C_2. For the polarizer orientation ϕ_p at 45° with the average twist angle ϕ_d, the zero order transmission decreases for increasing voltages. The inhomogeneity of the director distribution increases the amount of light that is coupled into the diffraction orders as was already shown in Figures 5.25 and 5.26.

To show that nevertheless the device acts as a homogeneous birefringent layer with a reduced retardation, the polarization state of the transmitted light is studied in case the analyzer is removed. Figure 5.28 shows the polarization state of the transmitted zero order diffraction on the Poincaré sphere, as a function of the azimuthal angle ϕ_d of the incident linear polarization for driving configuration C_2. Linear polarizations parallel to the x and y-axis are indicated on the Poincaré sphere

with respectively H and V. The right and left-handed circular polarizations located in the poles are indicated with R and L.

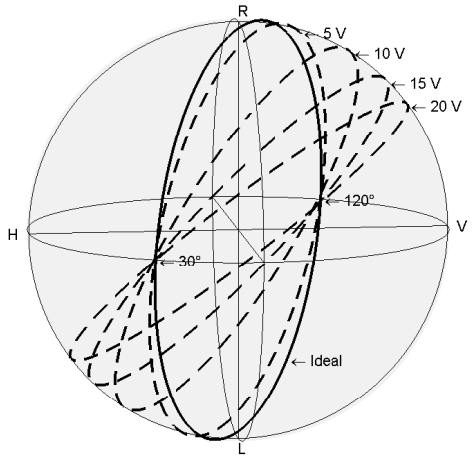

Figure 5.28: The polarization state of the zero order transmission as a function of the polarizer orientation ϕ_p represented on the Poincaré sphere, calculated with the Rigorous Coupled Wave Method with driving configuration C_2 for the ideal case (solid) and the applied voltages 5, 10, 15 and 20 V (dashed).

For a homogeneous liquid crystal the curve, plotted as a full line, describes a circle on the sphere. The circle starts on the equator in the point indicated with 30°, which corresponds with a linear incident polarization parallel the liquid crystal director ($\psi = \phi_p = \phi_d = 30°$, $\chi = 0°$). For this polarization and for the one orthogonal to it (120°), the linear incident polarization is unchanged after propagation through the layer and the polarization is indicated by a pointer on the equator. For polarizer orientations ϕ_p at ±45° with the director, the linear polarization is transformed into almost circularly polarized light and the curve approaches the poles as expected for a retardation of about $3\lambda/4$.

For a reconfigurable wave plate with an inhomogeneous director distribution, the plots (dashed lines) also describe large circles on the sphere. For the incident linear polarizations parallel and perpendicular to the average director, the linear polarization remains unchanged after propagation through the layer. This results in an intersection of all curves on the equator in the points 30° and 120° and shows that for the zero order transmission, the layer acts indeed as a homogeneous birefringent plate.

With increasing voltages, the highest point of the circle descends toward the equator. Thus, the effective retardation, which is the retardation experienced by the zero order transmission, decreases. For a retardation of $\lambda/2$, the curve would coincide with the equator.

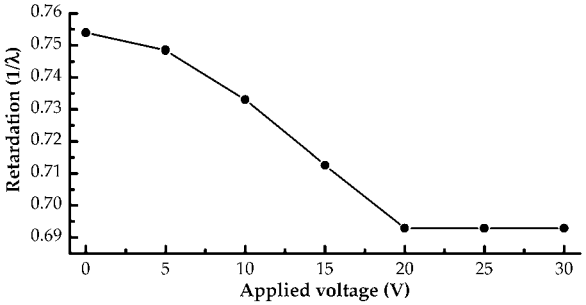

Figure 5.29: Effective retardation of the reconfigurable wave plate as a function of the applied voltage, normalized in wavelengths for λ = 632 nm.

Figure 5.29 shows the calculated effective retardation normalized to the used wavelength as a function of the applied voltage. Initially, the retardation is about $3\lambda/4$. For increasing voltages, it decreases and saturates at about 0.7λ. For voltages higher than 20 V, the director distribution does not change further with the applied voltage and the effective retardation remains the same.

If the reconfigurable wave plate is used to transform the incident polarization, the applied voltage can be used to tune the effective retardation of the layer. The range over which the incident polarization can be tuned depends on the thickness of the layer and the spacing of the hexagonal electrodes. Drawback is however that at high voltages, more light is lost due to diffraction.

c) Transmission as a function of time

In section 5.3, the director distribution was calculated as a function of time when the sequence of driving configurations $C_1 - C_2 - C_3 - C_1 - C_2 - C_3 - C_1$ was applied, each step during 250 ms starting from an initial director orientation along the y-axis. In Figure 5.30, the transmission as a function of time is plotted for the resulting director distributions as a full line for an applied voltage 5 V and as a dashed line for 10 V, calculated with the Rigorous Coupled Wave Method. The re-

configurable wave plate is positioned between crossed polarizers with fixed transmission axes along the x and y-axis. To illustrate that the reconfigurable wave plate really acts as a homogeneous layer for the zero order transmission, two plots are added (indicated with symbols) which are calculated with a homogeneous anisotropic layer oriented along the average twist ϕ_d which is plotted in Figure 5.30.

Although during the switching from one driving configuration to the next the liquid crystal layer is very inhomogeneous, the plots calculated with the average twist follow closely those calculated with the actual director distribution. The plots also confirm that the switching time for an applied voltage of 5 V is larger than 250 ms, while for 10 V switching is practically completed at 250 ms.

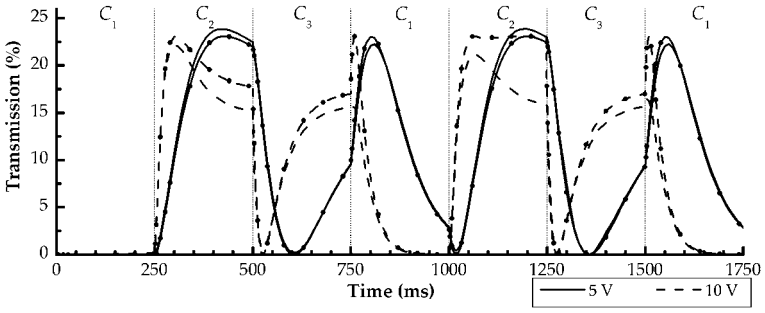

Figure 5.30: The zero order transmission as a function of time for 5 and 10 V when applying the sequence of driving configurations $C_1 - C_2 - C_3 - C_1 - C_2 - C_3 - C_1$, each for 250 ms and starting with the director aligned along the y-direction. The layer is positioned between crossed polarizers along the x and y-direction. Calculated with the Rigorous Coupled Wave Method using the simulated director distribution as a function of time (lines) or the average twist as a function of time (lines with symbols).

The overall conclusion of the optical transmission simulations is that the device works as expected in transmissive mode, but care should be taken to avoid light coupling in the diffraction orders. Therefore it is better to use high voltages to rotate the device quickly to the desired driving configuration. Afterward, the applied voltage can be lowered to homogenize the layer.

On the other hand, if an efficient way is found to filter out the unwanted diffraction orders (with a diaphragm for example) and if the zero order transmission continues to function as that of a homogeneous

layer, varying the applied voltage for a given driving configuration can be used to fine tune the retardation of the layer.

5.4.3 Reflective mode

When working in reflective mode, the simulated stack is different as illustrated in Figure 5.21(b). The analyzer is removed and the electrodes are represented by a reflector at the bottom. In the actual device, light that is incident in the area between the hexagonal electrodes will reflect at the lower interconnection electrodes. This is neglected in the calculations by assuming a homogeneous reflector in the xy-plane covering the whole surface. In the algorithm based on the Jones Matrix Method a perfect mirror, which reflects all light without absorption, is used as reflector. In the Rigorous Coupled Wave Method, a homogeneous metal layer with a thickness of 100 nm and the refractive index of titanium $n_{\mathrm{ti}} = 2.59 - i\,3.56$ is used as reflector.

The dielectric layer between the electrodes and the liquid crystal is no longer negligible in reflective mode because of multiple reflections and interference in the transparent dielectric layer. The inserted layer has a thickness of 1.3 µm as in the simulated device above and a refractive index $n_{\mathrm{d}} = 1.6$. The normally incident light is again assumed unpolarized, with a wavelength of 632 nm.

a) Improvement of the Jones Matrix Method algorithm

Before investigating the reflection at the reconfigurable wave plate, a closer look is taken at the ideal reflection when the director is uniformly oriented along the orientation $\phi_d = 30°$ of driving configuration C_2. The reflection of the total device as a function of the polarizer orientation ϕ_p is plotted in Figure 5.31 for the Jones Matrix Method (JMM original) and the Rigorous Coupled Wave Method (RCWM).

The total retardation in reflection is approximately one and a half wavelength. A polarizer orientation parallel and perpendicular to the director ($\phi_p = \phi_d$ or $\phi_p = \phi_d + 90°$) should give a reflection of 50 %. For $\phi_p = \phi_d \pm 45°$, the reflection should be almost zero.

Although the simulated device is a simple stack of one-dimensional layers, the two methods give quite different results. The Jones Matrix Method gives a result as expected. The maximum of 50 % is not reached due to losses by Fresnel reflections at the interface. The results of the

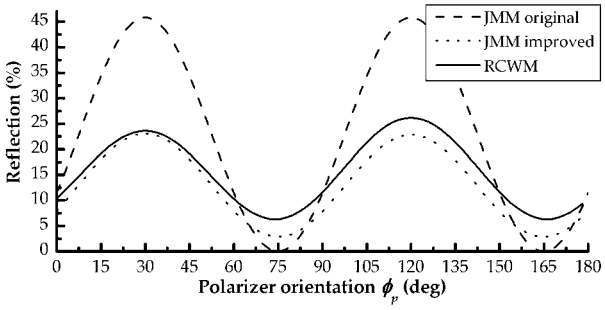

Figure 5.31: Reflection at an ideal wave plate (homogeneous liquid crystal layer) as a function of the polarizer orientation ϕ_p for driving configuration C_2 with $\phi_d = 30°$.

Rigorous Coupled Wave Method on the other hand, looks completely different. First of all, the maximum reflection is much lower than the ideal 50 % and the polarizer orientations parallel ($\phi_p = 30°$) or perpendicular ($\phi_p = 120°$) to the director give a slightly different reflection. Secondly, at a polarizer angle of 45° with the director, the Jones Matrix Method reaches almost complete extinction as expected, whereas the Rigorous Coupled Wave Method still has a reflection of 6 %.

The differences between both calculations arise from approximations used in the Jones Matrix Method. Therefore, some modifications must be made to the Jones Matrix Method algorithm to obtain a correct result when working in reflection:

– An ideal reflector has a reflectivity of 100 %. The metallic reflector with complex refractive index n_{ti} absorbs partly the incident light. Therefore, the correct reflection should be approximated with the Fresnel reflection coefficient [49]

$$r = \frac{n_{\mathrm{ti}} - n_{\mathrm{d}}}{n_{\mathrm{ti}} + n_{\mathrm{d}}}. \tag{5.5}$$

Since $|r|^2 \approx 45$ %, this results in a lowered maximum reflection.

– The Fresnel reflections at the interfaces between the liquid crystal and the polarizer are pure losses when working in transmissive mode. In reflective mode, the reflection of the incident plane wave at the interface propagates back in the same direction as the light that is reflected at the reflector and should therefore be

added to the result. The undesired reflected wave can be calculated from the continuity of the tangential component of the electric field at the interface

$$\overline{E}_i + \overline{E}_r = \overline{E}_t. \tag{5.6}$$

The intensity of $\overline{E}_r$ is approximately 5 % of the intensity of the incident light and will cause a non-zero reflection at the polarizer orientations ϕ_p of 75° and 165°.

– When a plane wave is incident on a birefringent medium from air, the ordinary and extra-ordinary wave sense a different refractive index. Therefore, the Fresnel transmission coefficients should be calculated separately for the ordinary and extra-ordinary wave. This leads to the following Jones matrix representation of the insertion losses

$$\mathbf{T}_{in} = \mathbf{R}\left(-\phi\right) \begin{bmatrix} \frac{2}{1+n_{\text{eff}}} & 0 \\ 0 & \frac{2}{1+n_{\text{o}}} \end{bmatrix} \mathbf{R}\left(\phi\right), \tag{5.7a}$$

$$\mathbf{T}_{out} = \mathbf{R}\left(-\phi\right) \begin{bmatrix} \frac{2n_{\text{eff}}}{1+n_{\text{eff}}} & 0 \\ 0 & \frac{2n_{\text{o}}}{1+n_{\text{o}}} \end{bmatrix} \mathbf{R}\left(\phi\right), \tag{5.7b}$$

which replace the Fresnel transmission coefficients (3.10) in the Jones matrix representation of equation (3.9). The angle ϕ is the local director twist at the interface. The result of this adaption is a small difference between the reflection for a polarizer orientation parallel or perpendicular to the director.

The result of the improvements is plotted in the curve "JMM Improved". The comparison between the Rigorous Coupled Wave Method and the Improved Jones Matrix Method in Figure 5.31 is much better. The maximum reflection is of the same magnitude and total extinction is never obtained.

The effect of the dielectric layer can only be seen in the Rigorous Coupled Wave Method. Varying the thickness of the layer changes the magnitude of the maximum reflection due to interference. In the Jones Matrix Method, the backward reflection at the interface is added incoherently. Therefore, the thickness of the dielectric layer has no influence there.

From this simple example it is clear that the behavior of the reconfigurable wave plate in reflective mode is subjected to effects which influence its functionality. In order to obtain a larger contrast, additional

effort should be made to optimize the design. The main objectives for dealing with those difficulties would be anti-reflection coatings and an improved reflectivity at the reflector.

b) Reflection at the reconfigurable wave plate

Figure 5.32 shows the zero order reflection in the three driving configurations for an applied voltage of 5 and 10 V. The result for 5 V agree well with the ideal curves. A closer look at the plots for 10 V shows that

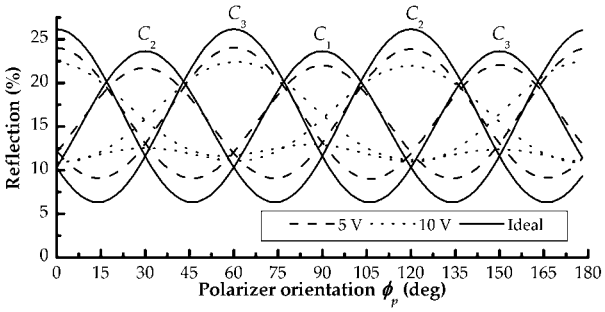

(a) Calculated with the Rigorous Coupled Wave Method

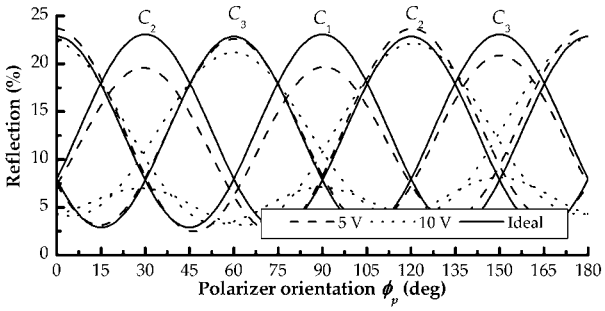

(b) Calculated with the Improved Jones Matrix Method

Figure 5.32: The zero order reflection at the reconfigurable wave as a function of the polarizer orientation ϕ_p in the three different driving configurations.

there is a large intensity difference between the polarizer orientation ϕ_p parallel or perpendicular to the average director ϕ_d. With the polarizer perpendicular to the director, the curve follows the ideal curve. Oriented parallel to the director, the maximum reflection is 15 % lower. The results of the Improved Jones Matrix Method show the same behavior.

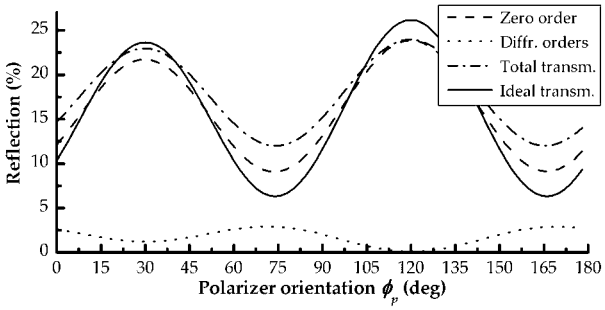

(a) Calculated with the Rigorous Coupled Wave Method

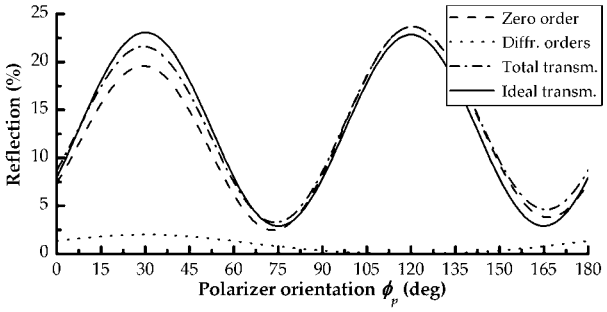

(b) Calculated with the Improved Jones Matrix Method

Figure 5.33: Reflection at the reconfigurable wave as a function of the polarizer orientation ϕ_p for driving configuration C_2 with an applied voltage of 5 V.

Figure 5.33 shows the reflection in more detail for driving configuration C_2 and an applied voltage of 5 V. Because of reflections and absorption at the reflector, the obtained contrast ratio of the zero order reflection is much lower as explained in the previous section. As in the transmissive mode, the effect of diffraction is negligible with a contribution below 2 %.

Comparison of the Improved Jones Matrix Method and the Rigorous Coupled Wave Method shows that the overall resemblance is good, but less good than in the transmissive mode. This is to be expected since the total layer thickness in reflection of 6.8 μm, is no longer small compared to the wavelength and therefore, the influence of diffraction is more important. Although the intensity of the diffraction orders is lower than 2 %, the curves for the Improved Jones Matrix Method and the Rigorous Coupled Wave Method are already different.

In Figure 5.34, the reflection for an applied voltage of 10 V is detailed. The first striking observation is the large difference in reflection between the polarizer orientations parallel and perpendicular to the average director. To understand how this is possible, the director distribution must be studied more closely. 10 V is a rather high voltage. Therefore, the twist angle ϕ is almost homogeneous and equal to the average twist $\phi_d = 30°$. The tilt angle θ on the other hand, reaches values as high as 60° in certain regions and the tilt angle of the liquid crystal layer is thus very inhomogeneous.

A plane wave with a linear polarization parallel to the average twist will excite the extra-ordinary wave in the liquid crystal. Because of the inhomogeneity of the tilt angle, the effective refractive index experienced by the extra-ordinary wave and the resulting phase of the exiting beam is inhomogeneous. Therefore, the extra-ordinary wave will be subject to diffraction and a lot of light is coupled into the diffraction orders. This is visible in Figure 5.34 at a polarizer orientation ϕ_p of 30°.

A plane wave with the incident linear polarization perpendicular to the average twist, will excite mainly the ordinary wave. The ordinary wave experiences the ordinary refractive index, which is independent of the director tilt angle. Because of the homogeneity of the director twist angle, the ordinary wave is not subject to diffraction and only very little light is coupled into the non-zero diffraction orders. This is visible in Figure 5.34 at a polarizer orientation ϕ_p of 120°. The zero order reflection reaches a high maximum, while the intensity of the diffraction orders stays below 2 %.

In transmissive mode the intensity of the diffraction orders was also about 10 %, but the zero order transmission still behaved as expected. In reflective mode, the non-homogeneity of the liquid crystal layer has a strong influence on the zero order reflectivity. Therefore, when using high voltages for fast switching of the device, the applied voltage should be lowered afterward in order to homogenize the liquid crystal layer.

5.5 Experiments

5.5.1 Production process of the reconfigurable wave plate

The realization of the reconfigurable wave plate was carried out in collaboration with partners of the European Research Training Network

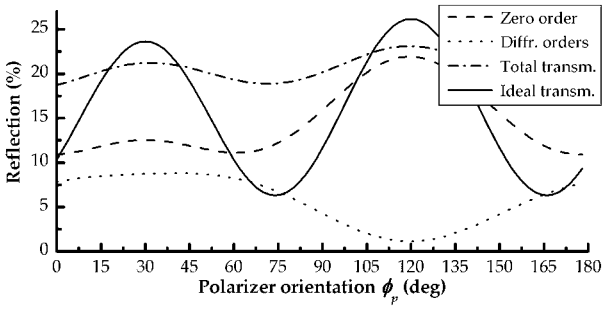

(a) Calculated with the Rigorous Coupled Wave Method

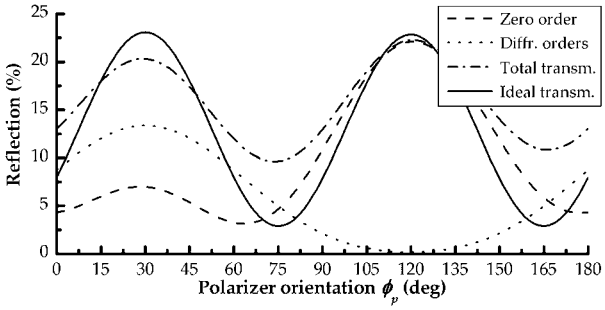

(b) Calculated with the Improved Jones Matrix Method

Figure 5.34: Reflection at the reconfigurable wave as a function of the polarizer orientation ϕ_p for driving configuration C_2 with an applied voltage of 10 V.

SAMPA and the Belgian IAP V/18 Photon-Network. Due to the long time cycle for the realization of a cell, the design of the cell was made before the results of the simulations was known. Therefore, the realized device is not completely optimized.

a) Device design

A scheme of the device design is given in Figure 5.35. The design contains 25 cells on a 3×3 inch substrate. The individual cells measure 12×12 mm. Each cell has 5 contact pads at the side and a square area of 4×4 mm in the center containing the hexagonal electrode pads (Figure 5.35(b)). Four contacts are used to address the four sets of interconnected hexagonal electrodes, the fifth applies its potential to the electrode surrounding the square area in the center. In the different cells, the spacing b between the electrodes and the side length a of the

hexagonal electrodes is varied. The dimension of the hexagons and the spacing are specified as a/b at the top of each cell.

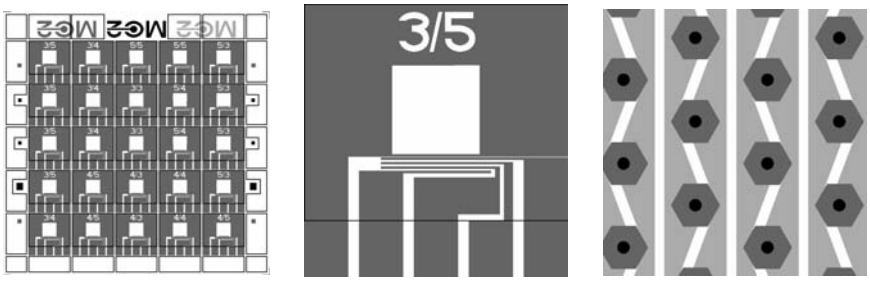

(a) The whole design with 25 cells

(b) One individual cell with 5 contacts

(c) Detail of the square area in the center

Figure 5.35: Scheme of the device design. (a) The whole design on a 3×3 inch substrate with 25 individual cells, (b) One 12×12 mm cell of the design with 5 contact pads at the side and a square are in the center containing the hexagonal electrodes, (c) a 31×31 μm detail of the square area with indication of the interconnection level (light gray), the vias (black) and the hexagonal electrodes with $a = 3$ μm and $b = 5$ μm (dark gray).

Figure 5.35(c) shows the hexagonal electrode pads, the vias and the interconnection electrodes of the cell with $a = 3$ μm and $b = 5$ μm. In the design phase is decided to cover most of the bottom glass substrate with the interconnection electrodes (light gray), to obtain a top surface which is as much as possible flat. The interconnection electrodes are long parallel lines with one flat edge and one sawtooth, so that the via (black) can be placed in the center of each hexagon (dark gray).

b) Device processing

The device with the different layers as described in Figures 5.1 and 5.35 requires four different masks to create the patterns in the different layers on the bottom substrate. The masks are designed and produced in collaboration with Koen D'havé in the framework of SAMPA at Chalmers University of Technology (Göteborg, Sweden).

The processing of the substrates was carried out in the Elintec clean room of Universiteit Gent in Zwijnaarde by Steven Verstuyft and Dries Van Thourhout of Intec (members of the IAP Photon-network). The production process of the substrates consists of the following steps:

– In the first step of the process, the interconnection electrodes are defined on the glass substrates.

  A homogeneous layer of titanium with a thickness of 100 nm is sputtered on the glass substrate. By photolithography using a first mask, the interconnection electrodes are defined. Afterward, the metal in the regions between the defined electrodes is removed by dry etching.

– In the second step, the dielectric layer between the interconnection electrodes and the hexagonal electrodes is formed, which holds the vias that allow to interconnect the two electrode layers in the device.

  A homogeneous layer of the polymer BCB with a thickness of approximately 0.8 µm is deposited by spin coating Dow Cyclotene 3022-35 on the substrate. The location of the vias is defined on the dielectric layer by a photolithography process with a second mask. Afterward, the holes for the vias are created in the dielectric layer by dry etching.

– In step three, the top electrode layer is formed on the bottom dielectric layer.

  In this step, the whole substrate surface is covered by a second layer of titanium with a thickness of 100 nm by sputtering. The holes in the bottom dielectric layer, that were created in the previous step, are filled with the metal during the sputtering process. This provides the required interconnections between the top and bottom metal layer. In a subsequent photolithography step, a third mask is used to define the location of the hexagonal electrode pads and the cell contacts. The metal between the defined electrodes is removed by dry etching.

– In the last step of the process, the top dielectric layer above the hexagonal electrodes is deposited.

  A second layer of BCB with a thickness of 1 µm is deposited homogeneously on the substrate by spin coating Dow Cyclotene 3022-35. After photolithography using a fourth mask, the polymer is removed from the cell contacts by dry etching.

A picture of the produced substrate and a detailed microscope picture of one of the hexagonal pixels is shown in Figure 5.36. The mask

used for producing the hexagonal electrodes was slightly misaligned during the manufacturing process. This explains the eccentric location of the vias in the hexagons visible in Figure 5.36(b).

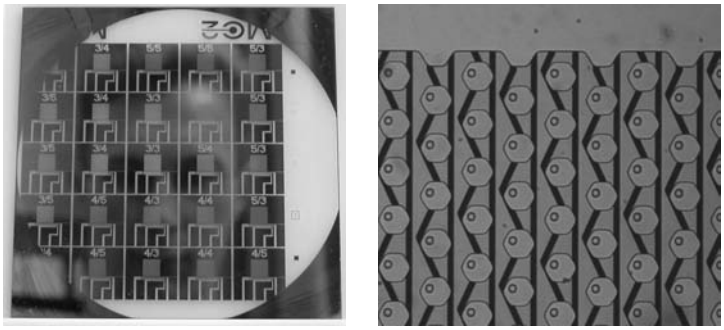

(a) Substrate with 25 cells (b) Detailed microscope picture

Figure 5.36: Picture of the substrate produced by Intec. (a) the whole 3×3 inch substrate with 25 cells, (b) a detailed microscope picture of the hexagonal electrodes (image size 73×68 µm), the interconnection electrodes and the vias in a cell with $a = 3$ µm and $b = 5$ µm

For the dielectric layers it was decided to work with the polymer BCB. The main reason is that BCB is deposited by spin coating, which simplifies and speeds up the production process. BCB has a low dielectric constant ε_d of approximately 2.5 and a refractive index n_d of 1.561 (Dow Chemical Company). The low dielectric constant ε_d is in fact a drawback for our device, since it reduces the strength of the electric field in the liquid crystal layer. To compensate for the low ε_d, the thickness d_0 of the top dielectric is reduced to 1 µm. An additional advantage of a spin coated polymer instead of an evaporated dielectric oxide is that it planarizes the top surface, yielding a flat top surface.

After production, the 3×3 inch glass substrate is cut into the individual cells by scratching a line between the individual cells with a diamond needle and breaking it afterward. The cells and the counter glass substrates are covered with the surfactant FC4430 by dip coating and finally both substrates are glued together using Norland Optical Adhesive NOA-68. To ensure a constant distance of 2.1 µm between the top and bottom substrate, spherical glass spacers with a diameter 2.1 µm of are added to the glue. Figure 5.37 shows a completed cell after wiring the contacts. The substrate with the electrodes is smaller than a paper clip, for ease of handling a larger counter glass substrate

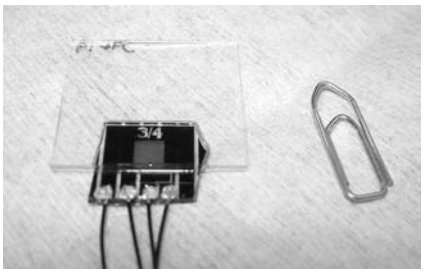

Figure 5.37: Picture of a finished hexagon cell. A 1 inch glass substrate is used as counter substrate and four wires are soldered to the contact pads.

is used (1×1 inch).

5.5.2 Measurements

In the experiments, it is not easy to verify the results of the optical simulations. The metal electrodes force us to use the wave plate in reflective mode. As illustrated in Figure 5.31, the main problem in reflective mode is to obtain a large contrast. The maximum reflection is achieved with the director along the polarizer axes and is limited by the intensity of the incident light. The minimum reflection depends on the retardation and the reflected light at the interfaces.

Narrow band color filters which fit in our microscope for measuring in reflective mode were not available. Therefore, the complete spectrum of the lamp must be used in the experiments. The incident light on the liquid crystal layer is linearly polarized. When the director is oriented at 45° with the polarizer ($\phi_d = \phi_p + 45°$), only for the wavelengths for which the total retardation in reflection is $\lambda/2 + n\lambda$ (with $n = 1, 2, \ldots$) the linear polarization is rotated over 90° and the light is absorbed when propagating backward through the polarizer. For all other wavelengths, the reflected wave is elliptically polarized and leaks partially through the polarizer. Therefore, the obtained contrast is very low.

The lack of monochromatic light and the resulting low contrast, make it impossible to verify the optical simulation results of section 5.4 directly. In a microscope however, the polarizer for the incident and reflected light are separated, as represented in Figure 5.38. Therefore, crossed polarizers can be used which gives two major advantages:

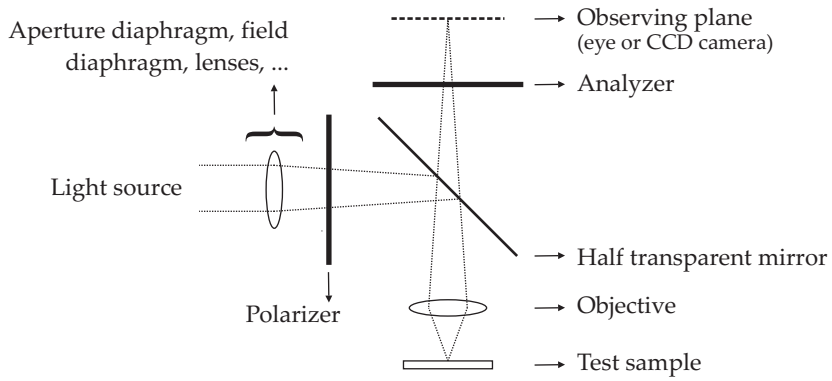

Figure 5.38: Simplified outline of a polarizing microscope used in reflective mode.

- The insertion losses at the interfaces have no influence when using crossed polarizers because they are absorbed by the analyzer.
- In reflective mode with crossed polarizers a dark state is easy to achieve. If the director is homogeneous and parallel to one of the polarizer axes, the linear polarization of the incident light is preserved and absorbed by the analyzer, independent of the wavelength.

With this setup, a good contrast can be obtained after all and this enables the demonstration of the working principle of the reconfigurable wave plate.

The hexagonal electrode pads in the tested cell have a side length a of 5 μm and the spacing b is 3 μm. The thickness of the BCB dielectric layer d_0 is 1 μm and the thickness d of the liquid crystal layer is 2.1 μm. The liquid crystal material used is E7. Both the top and bottom surface in direct contact with the liquid crystal are covered with the surfactant FC4430 to have a weak azimuthal anchoring, essential for unhindered horizontal rotation of the director.

a) Distinguishing the three different driving configurations

A first step in the experiments is to distinguish the three driving configurations and their corresponding average director orientation. One of the three directions is easy to find. From Figure 5.36(b) it can be seen

that for one driving configuration, the average director is oriented perpendicular to the sawtooth interconnection electrodes ($\phi_d = 90°$). If the rows of hexagonal electrodes at equal potential are parallel to the long interconnection electrodes and to one of the polarizer axes, the reflection should be low. This driving configuration will be referred to as C_1. The other two driving configurations, C_2 and C_3, have an average director twist ϕ_d of respectively 30° and 150°. Therefore, they should give a similar reflection image.

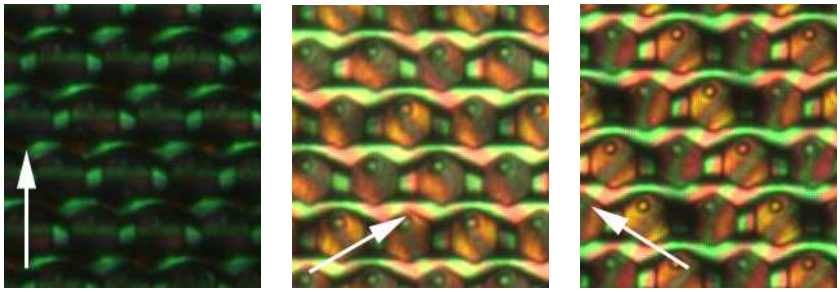

(a) Driving config. C_1 (b) Driving config. C_2 (c) Driving config. C_3

Figure 5.39: Pictures of the three driving configurations applied to the reconfigurable wave plate, with crossed polarizers parallel to the picture edges. The applied voltage is a 10 V/120 Hz square wave and the white arrow indicates the direction of the average electric field in the respective driving configurations. Image dimension 45 μm × 50 μm.

This is confirmed by the microscope observations in Figure 5.39. For these pictures, the sawtooth interconnection electrodes are oriented parallel to the horizontal edge of the picture. The transmission axes of the crossed polarizers of the microscope are oriented parallel to the horizontal and vertical edges of the pictures ($\phi_p = 0°$ and $\phi_a = 90°$). The waveform applied over the rows of hexagonal electrodes is a 120 Hz square wave with 10 V amplitude. As expected, one driving configuration (corresponding to C_1 with the average director vertically) gives a dark image, while the other two have a similar transmission. The white arrow in each picture indicates the average orientation of the director ϕ_d in the respective driving configuration.

C_2 and C_3 can be distinguished by the orientation of the colored line above the hexagonal electrodes. This line arises from a fast change of the director orientation at this location. The electric field at both sides of the equipotential mirror plane in the liquid crystal is tilted in different directions as illustrated in Figure 5.40 for driving configuration C_1.

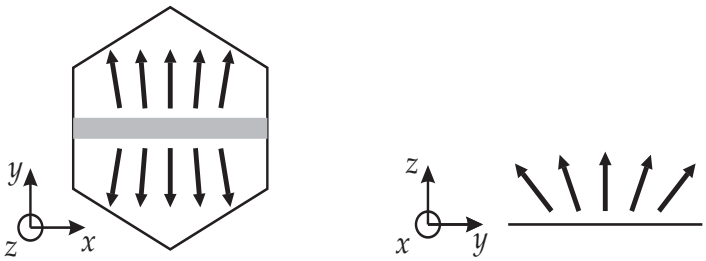

(a) top view (*xy*-plane) (b) side view (*xz*-plane)

Figure 5.40: Origin of the colored line observed through a microscope above the hexagonal electrodes for driving configuration C_1 with the average electric field along the y-axis. (a) the horizontal electric fields in the liquid crystal layer above a hexagonal electrode, (b) the fields parallel to yz-plane in the liquid crystal layer.

This results in a rather sharp change of the director tilt angle along the y-direction. The change in retardation induced by the tilt angle variation is visible with the microscope as a colored line (indicated in gray in Figure 5.40). The orientation of the line is perpendicular to the average electric field and is therefore an indication for the applied driving configuration.

b) Control of the average director alignment

By now, the three driving configurations and their average director are known. It is now possible to check whether the director is really on average oriented along the presumed directions indicated in Figure 5.39. Rotating the reconfigurable wave plate while keeping the polarizer orientations the same, should give a dark image each time one of the average director orientations is along the polarizer axes.

In Figure 5.41, this is verified. The three columns correspond the three driving configurations C_1, C_2 and C_3. The middle row shows the same device orientation as in the pictures of Figure 5.39, with the director vertical ($\phi_d = 90°$) for driving configuration C_1 and at angles of 30° and 150° for C_2 and C_3. The crossed polarizers are oriented along the vertical and horizontal direction. In the top and bottom row, the substrate was rotated 60° clockwise and counterclockwise respectively, while keeping the same polarizer orientation.

In each of the 9 pictures, the orientation of the average director after

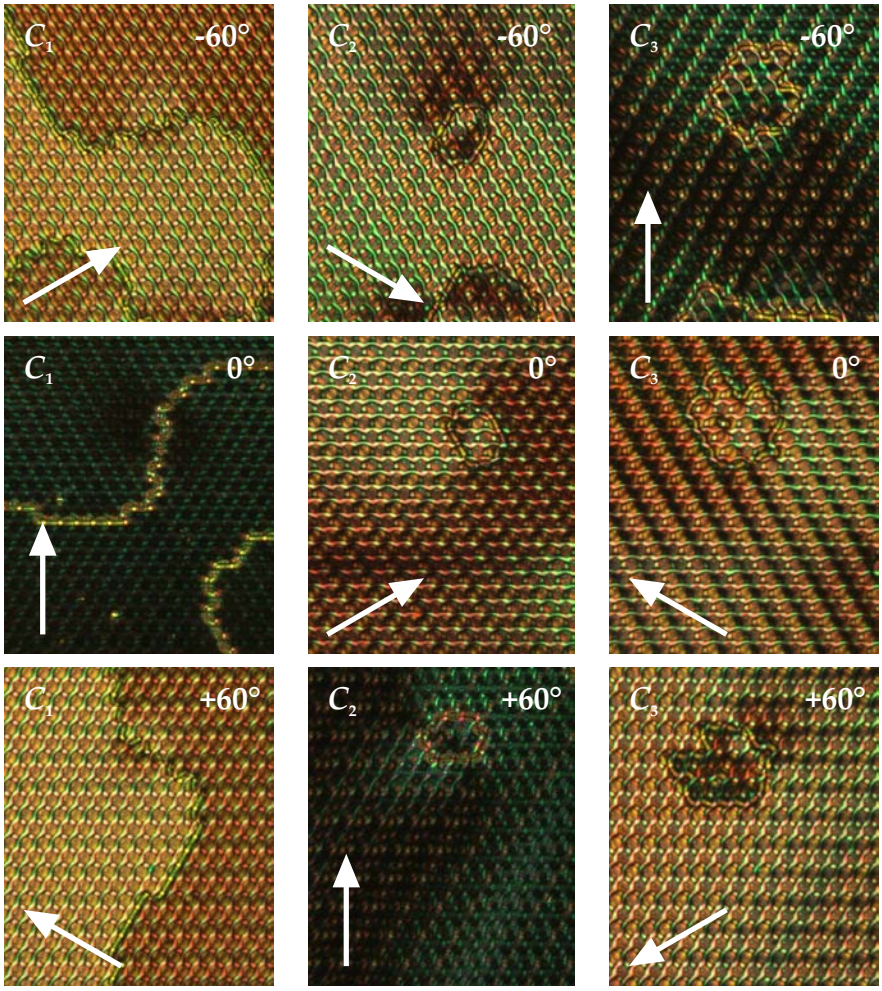

Figure 5.41: Observation of the reflection through a microscope for different orientations of the reconfigurable wave plate -60°, 0° and +60° (from top to bottom). In the three columns, the driving configurations C_1, C_2 and C_3 are respectively applied with a 10 V/120 Hz square wave. Picture taken in reflection with polarizer and analyzer along the horizontal and vertical edges of the pictures. Image dimension 190 μm $\times$ 225 μm.

rotating the substrate is indicated with a white arrow. By observation of the three rows, it is clear that for each row, the driving configuration in which the director lies along the vertical axis (parallel to one of the the polarizers axes) gives a dark image, while the other two have a similar color. This proves that three different driving configurations are obtained, with the director on average along the predicted orientations.

c) Influence of the applied potential

A last fact which can be verified by microscope observations, is the change of the director distribution while increasing the applied voltage. Without any electric field applied, the microscope image gives a Schlieren texture as shown in Figure 5.42. The weak azimuthal anchoring at the surfaces has resulted in large homogeneous regions. Studying the influence of the electric field and the rotation of the substrate, makes it possible to determine the director distribution as previously explained in section 4.6.2.d. The resulting director distribution is indicated on the picture with red lines. Three different types of singular points are visible, two with strength $s = +1$ and one with strength $s = -1$.

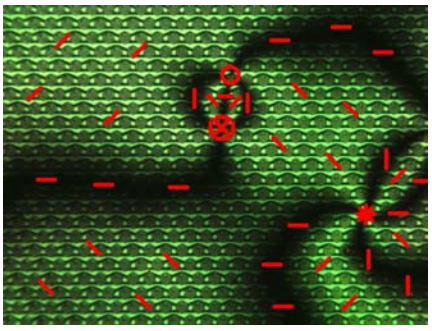

Figure 5.42: Observation of the Schlieren texture of the reconfigurable wave plate through the microscope when no voltage is applied, with indication of the director distribution. Image dimension 300 μm×225 μm.

In Figure 5.43, the three columns again represent the three driving configurations with the respective direction of the average electric field ϕ_{av} indicated by the white arrow. From top to bottom, the applied voltage is increased from 0 to 10 V in steps of 2.5 V and the polarizer transmission axes are oriented parallel to the vertical and horizontal edges for all the pictures.

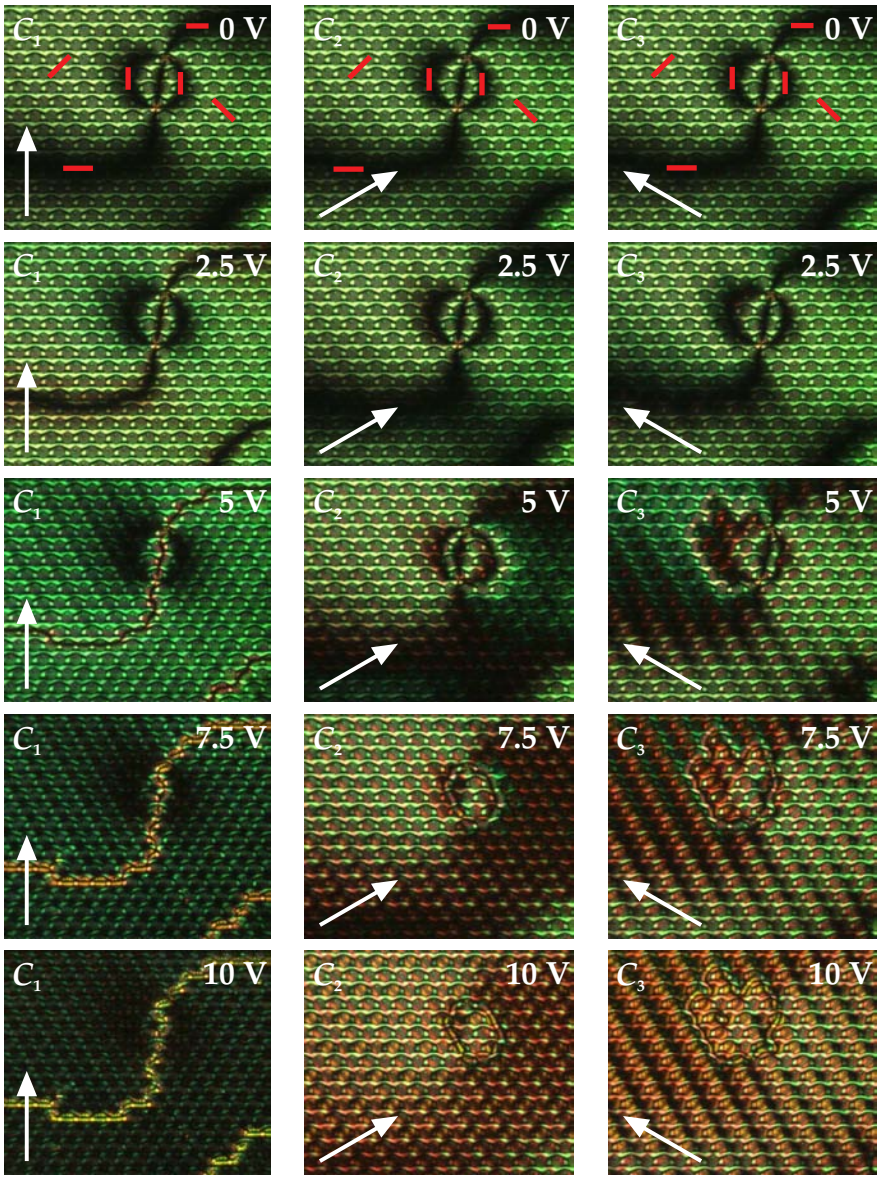

Figure 5.43: Observation of the reflection through a microscope for applied voltages of 0, 2.5, ..., 10 V (from top to bottom). In the three columns, the driving configurations C_1, C_2 and C_3 are respectively applied. Measurement in reflection with polarizer and analyzer along the horizontal and vertical edges of the pictures. Image dimension 190 μm $\times$ 160 μm.

At 0 V, the three driving configurations start from an identical director distribution, which is a zoom-in of the distribution shown in Figure 5.42. A first important observation is that already at 2.5 V (pictures in the the second row), the electric field influences the director distribution, especially for C_1. This clearly shows that weak azimuthal anchoring is achieved.

The effect of applying driving configuration C_1 is studied in the first column. The image at 0 V shows two defect points. The dark areas below and above the defect points have a horizontal director distribution (Figure 5.42), perpendicular to the average electric field of driving configuration C_1. When applying the electric field, these regions shrink at the expense of the neighboring green regions which have a director orientation at an azimuth of $\pm 45°$. For increasing voltages, the director in the 45° areas reorients to become more and more aligned along the vertical axis, which can be seen from the broadening of the two outer black brushes that interconnect the two defects and where the director remains at all times vertical. The original region with horizontal director at top and bottom and the center brush connecting the defects have shrunk to a thin surface inversion wall.

For C_2 in the middle column of Figure 5.43, the average electric field points to the right. In the green area at the top left of the 0 V picture, the average electric field is almost along the director. Therefore, only at high voltages this region changes color. In the green region at the right hand-side of the picture, the average electric field is almost perpendicular to the electric field. Therefore, a large rotation of almost 90° is required. During this rotation at 5 V, the director is horizontal and the region colors dark. A further increase of the applied voltage then rotates the director further and it becomes brighter again.

For C_3, the third column, the electric field points to the left. The reaction of the director is similar to the case for C_2. The region at the left is now almost perpendicular to the electric field and the region at the right hand-side almost parallel.

Generally when applying a certain driving configuration and increasing the applied voltage, the regions with the director oriented parallel to the average electric field grow at the expense of the neighboring regions. The regions with the original director perpendicular to the average electric field shrink and may form thin surface inversion walls. The location of the final surface inversion walls depends on the applied driving configuration as can be seen in Figure 5.43. Note that

for driving configuration C_1, the surface inversion wall becomes very long, while for C_2 and C_3 the surface inversion wall connects the point dislocations.

d) 360° in-plane rotation of the director

For 360° rotation as demonstrated in section 5.3, the three driving configurations must be applied sequentially. To do this, three waveforms were created using a 4-channel universal waveform generator. One of the four sets of hexagonal electrodes is connected to the mass, while a different waveform is applied the other three electrode groups as shown in Figure 5.44. The waveforms consist of three parts: twice a 120 Hz square wave with 10 V amplitude and one part where a short circuit is applied. The period of the whole waveform is 6 seconds, 2 seconds per driving configuration. To achieve a consistent electric field, the different channels of the waveform generator must be synchronized. At each point in time, the two channels to which the 120 Hz square wave is applied, must be positive and negative during the same time intervals.

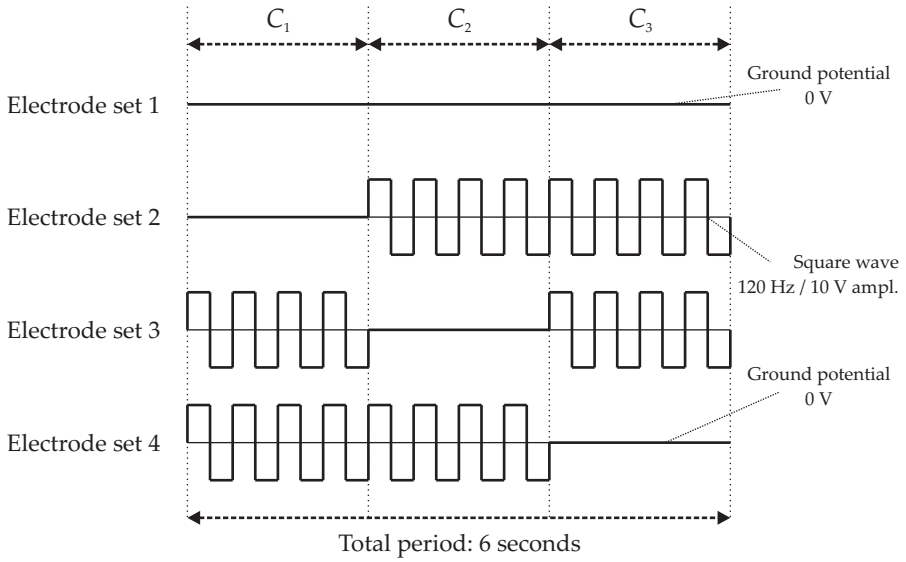

Figure 5.44: The waveforms applied to the four sets of interconnected hexagons in order to obtain a 360° in-plane rotation of the director.

When applying the waveforms to the test cell, the director does

not rotate 360° around the surface normal as expected. Instead, when changing the applied driving configuration the regions with the director along the average electric field grow at the expense of the rest. After ±0.5 second, a stable director distribution is obtained resulting in the images shown in Figure 5.45.

Thus, although a good homogeneous alignment along the presumed orientation can be obtained by gradually increasing the applied voltage within one driving configuration (Figure 5.43), when switching directly from one driving configuration to the next the obtained director distribution is not homogeneous. The resulting walls are much thicker as is shown in Figure 5.45. The difficulty is that, for a 360° in-plane rotation, the director should be switched homogeneously over the whole surface, whereas in reality the already correctly oriented regions grow. The slow response stems from the gradual growth of the regions in which the director is already along the average electric field.

Figure 5.45(a) shows that the alignment in driving configuration C_1 is better than in the other 2. Still, the director is not yet parallel to the vertical edge of the picture since the obtained image is not dark as in Figure 5.39(a). When rotating the substrate, it becomes clear that the twist angle in the regions above and below the inversion wall are slightly below and above 90°. The apparently stronger field in driving configuration C_1 comes from the interconnection electrodes below the hexagonal electrodes, which are in this case parallel to the rows of equally switched hexagons. Therefore, they strengthen the average electric field that reorients the director. In the other two driving configurations, they adversely influence the director reorientation.

e) Improvements to the device

A few suggestions can be made on different aspects of the device to improve it and maybe succeed in a 360° in-plane rotation.

A first and obvious improvement would be to increase the applied voltage, which would increase the homogeneity of the director twist angle ϕ and might force the director to make the full rotation. Unfortunately, 10 V is the maximum amplitude for the used wave generator.

Of course the anchoring at the top and bottom surface of the liquid crystal layer leaves room for improvement:

– Reducing the azimuthal anchoring even more or making it equal to zero, would surely be beneficial for the device.

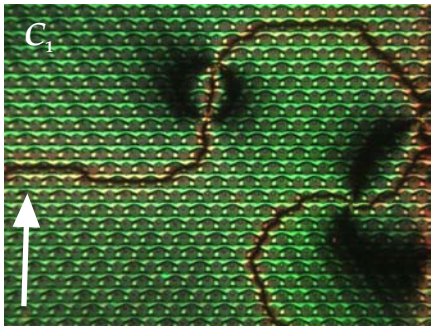

(a) Driving configuration C_1

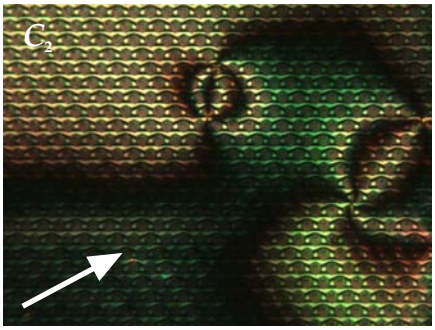

(b) Driving configuration C_2

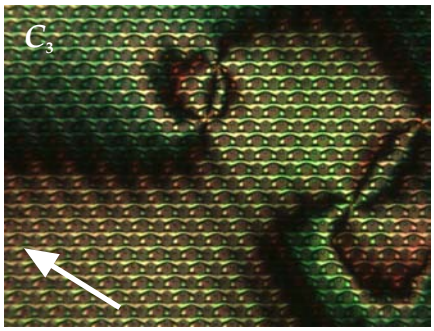

(c) Driving configuration C_3

Figure 5.45: Observation of the reflection through a microscope of the three driving configuration applied sequentially with 10 V amplitude and 2 s per driving configuration. Measurement in reflection with polarizer and analyzer along the horizontal and vertical edges of the pictures. Image dimension 300 μm $\times$ 225 μm.

– A second substantial improvement could be to start from homogeneous weak anchoring instead of a Schlieren texture. This could be obtained by applying an external horizontal magnetic field while filling the cell and cooling to the nematic phase.

Less influence of the interconnection electrodes on the electric field in the liquid crystal would increase the equivalence between the three driving configurations:

– If the thickness of the dielectric layer between the interconnection electrodes and the hexagonal electrodes is increased, their influence on the electric field in the liquid crystal is lower. On the other hand, this complicates the technology for the vias through the layer.

– A new design of the interconnection electrodes using thin lines instead of covering the whole surface would reduce their influence. But, in this case less light would be reflected by the device.

Finally a last improvement would be to use another metal for the electrode with a higher reflectivity such as gold, aluminum or silver. This is not critical for the working of the device, but would improve the optical characteristics.

5.6 Applications for the new liquid crystal device

The device acts as a rotating birefringent wave plate. Other device configurations that exhibit this characteristic have been proposed [49, 103, 124–129], but the advantage of the device with hexagonal electrodes is the distribution of the electrodes over the whole surface of the device. In this way, the required driving voltages can in principle be very low. Furthermore, there is no need for extra space next to the actual pixel to place the electrodes. A true azimuthally degenerated anchoring surface would enable the multistability of the device as explained above, but unfortunately such materials have not been reported yet.

The proposed operating principle has a number of interesting capabilities. Not only can it act as a wave plate, also other applications are possible for slightly modified parameters of the device. Possible extensions are briefly discussed below.

5.6.1 Hexagonal device with rubbed alignment layers

If the azimuthally degenerated planar anchoring surfaces at top and bottom are replaced by anti-parallel rubbed alignment layers with the preferential director along the average horizontal electric field of one driving configuration, a director rotation over an angle of 360° is no longer possible and the multistability disappears. On the other hand, the azimuthal angle now becomes continuously adjustable between $-60°$ and 60° about the rubbing direction by applying one of the other two driving configurations. The amount of rotation can be controlled by the strength of the applied electric field.

When the electric field is turned off, the elastic force stemming from the alignment at the boundaries will align the director in the liquid crystal homogeneously. By applying the driving configuration with average horizontal field parallel to the anchoring direction for a short time, the director is forced back into the off-state and thus the switching off time is decreased.

5.6.2 Electric field driven alignment direction

Some recent types of liquid crystal devices are based on switching between parallel and twisted states [131, 132]. Our new device can handle this type of switching. Decreasing the dimensions of the electrodes and the spacing between them below the thickness of the liquid crystal layer, lowers the effect of the driving field at the top substrate. The electrodes create an electric field at the bottom of the liquid crystal layer which forms a switchable alignment direction. A strong anchoring alignment layer on the top substrate in combination with such a switchable alignment at the bottom of the liquid crystal makes it possible to switch between the parallel and twisted state.

5.6.3 Intermediate director alignment

The liquid crystal director aligns along the average electric field. In the device proposed above, the average electric field and thus the director can be aligned along three different directions.

In order to align the director along an intermediate direction, two solutions are possible. If the device is really multistable, it is enough to switch off the applied voltage before the equilibrium state is achieved.

After switching off, the director will align along the average twist at that time.

If the surface suffers from too strong memory alignment and continuous application of the potential is required, another method might be possible. By alternating between two driving configurations at a high frequency, the time averaged electric field is then somewhere between the two driving configurations. So by varying the time ratio in which the two driving configurations are applied, any direction in between can be achieved.

The results of the director simulations have been published in the SCI Journal *Journal of applied physics D: applied physics* [133]. Abstract on the simulations and experiments have been submitted to the *International Workshop for Liquid Crystals on Photonics* (26–28 April 2006, Gent, Belgium) [134] and the *21st International Liquid Crystal Conference* (2–7 July, 2006, Keystone, Colorado, USA) [135] and are both accepted for oral presentation.

Chapter 6

Conclusion

In the preceding chapters, I have tried to explain the most important findings of my PhD research. The described work deals with many aspects of liquid crystals: modeling of the director distribution, optical transmission, surface anchoring and technology. In this chapter I want to conclude with a brief summary of the main achievements and an outlook to the future.

6.1 Achievements

The chapter on optical transmission compares three different optical algorithms in liquid crystals. Beside the accurate Rigorous Coupled Wave Method and the Reduced Grating Method, a simplified algorithm was demonstrated which allows a fast and easy calculation of the optical transmission through thin two or three-dimensional liquid crystal layers. The usefulness and correctness of this algorithm was demonstrated by comparison with the accurate optical algorithms throughout the whole thesis.

In a separate chapter, the alignment of liquid crystals at the surface was studied. The anchoring properties of different alignment materials were investigated with the aim of finding a surface material in which the azimuthal anchoring strength is reduced to a minimum. A measurement method was developed to accurately estimate the weak azimuthal anchoring strength. The surfactant FC4430 was identified as the material with the weakest azimuthal anchoring strength.

The different aspects of liquid crystals were used in the last chapter

to develop a new type of liquid crystal device in which the liquid crystal director rotates over 360° in the plane parallel to the glass substrates. Switching of the liquid crystal is induced by horizontal fields between hexagonal electrodes in a honeycomb arrangement below a stack containing a dielectric layer and a liquid crystal layer. This device can be used as a reconfigurable wave plate in optical setups.

First, the feasibility of the director rotation was demonstrated by three-dimensional director simulations. In the director simulation, special attention was paid to the different parameters of the device. By means of extensive optical simulations, the operation as a rotatable wave plate was demonstrated and a test device has been built. The true 360° rotation did not succeed, but by microscope observation was demonstrated that the director could be aligned in three different directions. At the end, a number of suggestions were given to improve the device and realize the 360° director rotation.

Beside the application as a controllable wave plate, other applications are feasible if the device would be slightly modified. The device could act as an electric field driven alignment layer which allows switching between a homogeneous and twisted state. Replacement of the azimuthal degenerated surface anchoring with rubbed alignment layers makes the rotation continuously adjustable over a limited range. A continuous rotation to any angle might be possible, but requires further investigation of the rotation, anchoring and relaxation processes.

The results of the work has been published in two papers in SCI Journals and is presented at several scientific meetings and international conferences.

6.2 Outlook

The work described in the previous chapters has lead to the demonstration of a new concept, but there is always room for future research. Anchoring was longtime considered a side topic of liquid crystals, but with the increasing importance of weak anchoring it entered in the spotlights in the past years. Nowadays, many of the mechanisms are being studied and it is a main challenge for chemists to develop new materials with specific anchoring properties.

The promising properties of the new reconfigurable wave plate have been described in detail, but more time is required to improve

several aspects of the device. The realization of a new device design included the suggested improvements would be worth investigating.

Bibliography

[1] F. Reinitzer, "Beiträge zur Kenntniss des Cholesterins," Monatsh. Chem. **9**, 421–430 (1888).

[2] P. J. Collings, *Liquid Crystals: Nature's Delicate Phase of Matter* (IOP Publishing Ltd., Bristol, 1990), 2nd edition.

[3] P. G. D. Gennes and J. Prost, *The Physics of Liquid Crystals*, International Series of Monographs on Physics (Oxford University Press, Oxford, 1995).

[4] S. Elston and J. R. Sambles, *The Optics of Thermotropic Liquid Crystals* (Taylor & Francis Ltd, London, 1998).

[5] I.-C. Khoo, *Liquid Crystals: Physical Properties and Nonlinear Optical Phenomena* (Wiley-Interscience, 1994).

[6] E. B. Priestley and P. J. Wojtowicz, *Introduction to Liquid Crystals* (Plenum Publishing Corporation, New York, 1975).

[7] A. Adamski, *Thresholdless Switching in Ferro- and Antiferro-electric Liquid Crystal Displays*, Ph.D. thesis, Universiteit Gent, Gent (2005).

[8] A. Adamski, H. Pauwels, K. Neyts, C. Desimpel, G. Stojmenovik and S. Vermael, "The Non-uniform Theory Simulations of the Continuous Director Rotation Mode of FLCD's," in *Proceedings of the 22nd International Display Research Conference / Eurodisplay* (SID, Nice, France, 2002), pp. 501–504.

[9] A. Adamski, H. Pauwels, K. Neyts, C. Desimpel and S. Vermael, "Simulation of V-shaped stability in AFLC," in *Proceedings of SPIE. XIV Conference on Liquid Crystals: Chemistry, Physics and Applications* (SPIE, Washington, USA, 2002), pp. 127–134.

[10] P. Yeh and C. Gu, *Optics of Liquid Crystal Displays* (Wiley-Interscience, 1999).

[11] L. M. Blinov and V. G. Chigrinov, *Electrooptic Effects in Liquid Crystal Materials*, Partially Ordered Systems (Springer-Verlag, New York, 1996).

[12] P. Sarkar, P. Mandal, S. Paul, R. Paul, R. Dabrowski and K. Czuprynski, "X-ray diffraction, optical birefringence, dielectric and phase transition properties of the long homologous series of nematogens 4-(trans-4 '-n-alkylcyclohexyl) isothiocyanatobenzenes," Liq. Cryst. **30**, 507–527 (2003).

[13] V. P. Vorflusev, H. S. Kitzerow and V. G. Chigrinov, "Azimuthal surface gliding of a nematic liquid crystal," Appl. Phys. Lett. **70**, 3359–3361 (1997).

[14] Y. Zhou and S. Sato, "Electrooptical and response/relaxation properties of liquid crystal cells in in-plane switching mode with polyvinylcinnamate photoinduced alignment layer," Jpn. J. Appl. Phys. Part 1-Regular Papers Short Notes & Rev. Papers **37**, 4439–4443 (1998).

[15] K. Ichimura, "Photoalignment of liquid-crystal systems," Chem. Rev. **100**, 1847–1873 (2000).

[16] S. Kobayashi, Y. Iimura and M. Nishikawa, "New development in alignment layers for active matrix TN-LCDs," in *Conference record of the International Display Research Conference* (SID, Monterey, California, 1994), pp. 78–84.

[17] H. De Vleeschouwer, B. Verweire, K. D'Have and H. Zhang, "Electrical and Optical Measurements of the Image Sticking Effect in Nematic LCD's," Mol. Cryst. Liq. Cryst. **331**, 567–574 (1999).

[18] H. De Vleeschouwer, F. Bougrioua and H. Pauwels, "Importance of Ion transport in Industrial LCD applications," Mol. Cryst. Liq. Cryst. **360**, 29–39 (2001).

[19] S. Vermael, *Ontwikkeling van 2D en 3D Monte Carlo Algoritmes om Ionentransport te Simuleren in Isotrope en Anisotrope Media*, Ph.D. thesis, Universiteit Gent, Gent (2004).

[20] G. Stojmenovik, *Ion Transport and Boundary Image Retention in Nematic Liquid Crystal Displays*, Ph.D. thesis, Universiteit Gent, Gent (2005).

[21] G. Stojmenovik, K. Neyts, S. Vermael, C. Desimpel, A. Adamski, A. R. Verschueren and R. a. Van Asselt, "Measurements of lateral ion transport in LCD cells," Mol. Cryst. Liq. Cryst. **409**, 515–527 (2004).

[22] H. Wohler and M. E. Becker, "Numerical modelling of LCD electro-optical performance," Opto-Electron. Rev. **10**, 23–33 (2002).

[23] R. N. Thurston and D. W. Berreman, "Equilibrium and stability of liquid-crystal configurations in an electric-field," J. Appl. Phys. **52**, 508–509 (1981).

[24] F. Cuypers, *Simulatie van de Evenwichtsorintaties in en de Optische Transmissie van Vloeibaar Kristal Beeldschermen*, Ph.D. thesis, Rijksuniversiteit Gent (1989).

[25] F. Di Pasquale, F. A. Fernández, S. E. Day and J. B. Davies, "Two-dimensional Modeling of Nematic LCD cells Using the In-Plane Switching Mode," in *Society for Information Display International Symposium Digest of Technical Papers* (SID, Boston, USA, 1997), pp. 695–698.

[26] F. Di Pasquale, H. F. Deng, F. Fernández, S. Day, J. Davies, M. Johnson, A. van der Put, J. van de Eerenbeemd, J. van Haaren and J. Chapman, "Theoretical and experimental study of nematic liquid crystaldisplay cells using the in-plane-switching mode," IEEE Trans. Electron Devices **46**, 661–668 (1999).

[27] F. Di Pasquale, F. A. Fernández, S. E. Day and J. B. Davies, "Two-dimensional finite-element modeling of nematic liquid crystal devices for optical communications and displays," IEEE J. Selected Topics In Quantum Electronics **2**, 128–134 (1996).

[28] J. B. Davies, S. Day, F. DiPasquale and F. A. Fernández, "Finite-element modelling in 2-D of nematic liquid crystal structures," Electron. Lett. **32**, 582–583 (1996).

[29] F. A. Fernández, S. E. Day, P. Trwoga, H. F. Deng and R. James, "Three-dimensional modelling of liquid crystal display cells using finite elements," Mol. Cryst. Liq. Cryst. **375**, 291–299 (2002).

[30] H. Mori, E. C. Gartland, J. R. Kelly and P. J. Bos, "Multidimensional director modeling using the Q tensor representation in a liquid crystal cell and its application to the pi cell with patterned electrodes," Jpn. J. Appl. Phys. Part 1-Regular Papers Short Notes & Rev. Papers **38**, 135–146 (1999).

[31] M. E. Becker, H. Wöhler, M. Kamm and J. Kreis, "Numerical Modelling of IPS Effects : A New Approach and More Results," in *Society for Information Display International Symposium Digest of Technical Papers* (SID, San Diego, USA, 1996), pp. 596–599.

[32] R. Dabrowski, "New liquid crystalline materials for photonic applications," Mol. Cryst. Liq. Cryst. **421**, 1–21 (2004).

[33] M. Schadt and W. Helfrich, "Voltage-dependent Optical Activity of a Twisted Nematic Liquid Crystal," Appl. Phys. Lett. **18**, 127–128 (1971).

[34] M. Oh-e and K. Kondo, "Electro-optical characteristics and switching behavior of the in-plane switching mode," Appl. Phys. Lett. **67**, 3895–3897 (1995).

[35] M. Oh-e and K. Kondo, "Response mechanism of nematic liquid crystals using the in-plane switching mode," Appl. Phys. Lett. **69**, 623–625 (1996).

[36] M. Oh-e, M. Yoneya, M. Ohta and K. Kondo, "Dependence of viewing angle characteristics on pretilt angle in the in-plane switching mode," Liq. Cryst. **22**, 391–400 (1997).

[37] E. Lueder, *Liquid Crystal Displays : Addressing Schemes and Electro-Optical Effects*, Wiley Series in Display Technology (John Wiley & Sons, Chichester, 2001).

[38] J. Nehring, A. R. Kmetz and T. J. Scheffer, "Analysis of weak-boundary-coupling effects in liquid-crystal displays," J. Appl. Phys. **47**, 850–857 (1976).

[39] C. J. Chen, J. P. Pang and T. H. Hsieh, "A Novel High Transmission In-Plane-Switching (IPS) LCD," in *Proceedings of the International Display Research Conference* (SID, Phoenix, Arizona, 2003), pp. 69–71.

[40] G. B. Arfken and H. J. Weber, *Mathematical Methods for Physicists* (Academic Press, 2000).

[41] D. Zwillinger, *CRC Standard Mathematical Tables and Formulae* (Chapman & Hall/CRC, 2002), 31st edition.

[42] L. F. Shampine, I. Gladwell and S. Thompson, *Solving ODEs with MATLAB* (Cambridge University Press, 2003).

[43] H. K. Hong and C. R. Seo, "Dependency of liquid crystal of in-plane switching mode on rubbing angle," Jpn. J. Appl. Phys. Part 1-Regular Papers Short Notes & Rev. Papers **43**, 7639–7642 (2004).

[44] S. H. Lee, G. J. You, H. Y. Kim, D. S. Lee, S. K. Kwon, H. S. Park and C. K. Kim, "Influence of Rubbing Direction on the Electro-Optic Characteristics of In-Plane-Switching-Mode LCDs," in *Society for Information Display International Symposium Digest of Technical Papers* (SID, Boston, USA, 1997), pp. 711–714.

[45] J. Beeckman, K. Neyts, X. Hutsebaut, C. Cambournac and M. Haelterman, "Simulations and experiments on self-focusing conditions in nematic liquid-crystal planar cells," Opt. Express **12**, 1011–1018 (2004).

[46] J. Beeckman, K. Neyts, X. Hutsebaut, C. Cambournac and M. Haelterman, "Simulation of 2-D lateral light propagation in nematic-liquid-crystal cells with tilted molecules and nonlinear reorientational effect," Opt. Quantum Electron. **37**, 95–106 (2005).

[47] S. Huard, *Polarisation de la lumière* (Masson, Paris, 1997).

[48] R. Azzam and N. Bashara, *Ellipsometry and Polarized Light* (Elsevier Science Publishers B.V., Amsterdam, 1987), 4th edition.

[49] K. Iizuka, *Elements of Photonics: In Free Space and Special Media*, Vol. 1 (Wiley-Interscience, New York, 2002).

[50] M. Born and E. Wolf, *Principles of Optics: Electromagnetic Theory of Propagation, Interference and Diffraction of Light* (Cambridge University Press, Cambridge, 1999), 7th edition.

[51] R. Jones, "A New Calculus for the Treatment of Optical Systems," J. Opt. Soc. Am. A **31**, 488–493 (1941).

[52] P. Yeh, *Optical Waves in Layered Media*, Wiley Series in Pure and Applied Optics (Wiley-Interscience, 1988).

[53] P. Yeh, "Extended jones matrix-method," J. Opt. Soc. Am. **72**, 507–513 (1982).

[54] A. Lien, "A detailed derivation of extended Jones matrix representation for twisted nematic liquid crystal displays," Liq. Cryst. **22**, 171–175 (1997).

[55] C. Gu and P. Yeh, "Extended jones matrix-method. II," J. Opt. Soc. Am. A-optics Image Science Vision **10**, 966–973 (1993).

[56] J. Simmons and K. S. Potter, *Optical Materials* (Academic Press, San Diego, USA, 1999).

[57] M. Bass, E. W. V. Stryland, W. R. David and W. L. Wolfe, *Handbook of Optics*, Vol. 1 (McGraw-Hill Professional, New York, 1994).

[58] M. Oh-e and K. Kondo, "The in-plane switching of homogeneously aligned nematic liquid crystals," Liq. Cryst. **22**, 379–390 (1997).

[59] M. Oh-e, M. Ohta, S. Aranti and K. Kondo, "Principles and characteristics of electro-optical behaviour with in-plane switching mode," in *Proceedings of the 15th International Display Research Conference / Asia Display* (SID, Hamamatsu, Japan, 1995), pp. 577–580.

[60] M. Ohta, M. Oh-e and K. Kondo, "Development of Super-TFTLCDs with In-Plane Switching Display Mode," in *Proceedings of the 15th International Display Research Conference / Asia Display* (SID, Hamamatsu, Japan, 1995), pp. 707–710.

[61] K. Vermeirsch, *Richtingsafhankelijkheid van de Optische Eigenschappen van Vloeibaar-Kristallagen*, Ph.D. thesis, Universiteit Gent, Gent (2000).

[62] E. E. Kriezis and S. J. Elston, "A wide angle beam propagation method for the analysis of tilted nematic liquid crystal structures," J. Modern Optics **46**, 1201–1212 (1999).

[63] E. E. Kriezis and S. J. Elston, "Light wave propagation in liquid crystal displays by the 2-D finite-difference time-domain method," Optics Comm. **177**, 69–77 (2000).

[64] E. E. Kriezis and S. J. Elston, "Numerical modelling of multidimensional liquid crystal optics: Finite-difference time-domain method," Mol. Cryst. Liq. Cryst. **359**, 609–619 (2001).

[65] E. E. Kriezis and S. J. Elston, "Finite-difference time domain method for light wave propagation within liquid crystal devices," Optics Comm. **165**, 99–105 (1999).

[66] E. E. Kriezis and S. J. Elston, "Light wave propagation in periodic tilted liquid crystal structures: a periodic beam propagation method," Liq. Cryst. **26**, 1663–1669 (1999).

[67] E. E. Kriezis and S. J. Elston, "Wide-angle beam propagation method for liquid-crystal device calculations," Appl. Optics **39**, 5707–5714 (2000).

[68] K. Rokushima and J. Yamakita, "Analysis of anisotropic dielectric gratings," J. Opt. Soc. Am. **73**, 901–908 (1983).

[69] M. Nevière and E. Popov, *Light Propagation in Periodic Media: Differential Theory and Design (Optical Engineering)* (Marcel Dekker, 2002).

[70] P. Galatola, C. Oldano and P. B. S. Kumar, "Symmetry properties of anisotropic dielectric gratings," J. Opt. Soc. Am. A-optics Image Science Vision **11**, 1332–1341 (1994).

[71] W. D. Sheng, "Calculation of the band structure of semiconductor quantum wells using scattering matrices," J. Phys.-Condens. Matter **8**, 10 347–10 352 (1996).

[72] O. Peverini, D. Olivero, C. Oldano, R. Orta, R. Tascone, D. de boer and R. Cortie, "A new reduced-order model technique for the analysis of anisotropic layered media: an application to liquid crystal displays," in *Proceedings of the International Conference on Electromagnetics in Advanced Applications* (Torino, Italy, 2001).

[73] O. A. Peverini, D. Olivero, C. Oldano, D. K. G. de Boer, R. Cortie, R. Orta and R. Tascone, "Reduced-order model technique for the analysis of anisotropic inhomogeneous media: application to

liquid-crystal displays," J. Opt. Soc. Am. A-optics Image Science Vision **19**, 1901–1909 (2002).

[74] D. Olivero and C. Oldano, "Numerical methods for light propagation in large LC cells: a new approach," Liq. Cryst. **30**, 345–353 (2003).

[75] Y. Saad, *Iterative Methods for Sparse Linear Systems* (Society for Industrial and Applied Mathematic, 2003), 2nd edition.

[76] G. Strang, *Introduction to Linear Algebra* (Wellesley College, 2003), 3rd edition.

[77] K. Neyts, K. Vermeirsch, S. Vermael, H. D. Vleeschouwer, F. Bougrioua, S. Rozanski, D. de Boer, J. van Haaren and S. Day, "Simulations of Refraction, Retardation and Transmission in Liquid Crystal Displays with Slow Lateral Variations," in *Conference Record of the 20th International Display Research Conference* (SID, Palm Beach, Florida, 2000), pp. 225–228.

[78] C. Desimpel, K. Neyts, I. Janevska, A. Gjurcinovski, D. K. G. de Boer and R. Cortie, "Polarization state of the diffraction peaks in In-Plane Switching Cells," in *Proceedings of the 21st International Display Research Conference in conjunction with The 8th International Display Workshops* (SID, Nagoya, Japan, 2001), pp. 161–164.

[79] C. Desimpel, K. Neyts, D. Olivero, C. Oldano, D. K. G. de Boer and R. Cortie, "Optical transmission model for thin two-dimensional layers," in *Book of Abstracts, 10th International Topical Meeting on Optics of Liquid Crystals* (Université d'Artois, Aussois, France, 2003), p. 75.

[80] C. Desimpel, K. Neyts, D. Olivero, C. Oldano, D. K. G. de Boer and R. Cortie, "Optical transmission model for thin two-dimensional layers," Mol. Cryst. Liq. Cryst. **422**, 185–195 (2004).

[81] W. Liu and J. Kelly, "Multidimensional Modeling of Liquid Crystal Optics Using a Ray-Tracing Technique," in *International Symposium Digest of Technical Papers* (SID, Long Beach, California, 2000), pp. 847–850.

[82] Y. Sato, K. Sato and T. Uchida, "Relationship between rubbing strength and surface anchoring of nematic liquid-crystal," Jpn. J. Appl. Phys. Part 2-Letters **31**, L579–L581 (1992).

[83] J. H. Kim, M. Yoneya and H. Yokoyama, "High-resolution bistable nematic liquid crystal device realized on orientational surface patterns," Appl. Phys. Lett. **83**, 3602–3604 (2003).

[84] H. Desmet, K. Neyts and R. Baets, "Influence of etched silicon patterns on the liquid crystal orientation," in *Programme & Abstracts of the 16th Conference on Liquid Crystals (Chemistry, Physics & Applications)* (Military University of Technology Warschau, Stare Jabłonki, Poland, 2005), p. 30.

[85] H. Desmet, K. Neyts and R. Baets, "Modeling nematic liquid crystals in the neighborhood of edges," J. Appl. Phys. **98**, 123 517 (2005).

[86] R. Barberi, I. Dozov, M. Giocondo, M. Iovane, P. Martinot-Lagarde, D. Stoenescu, S. Tonchev and L. V. Tsonev, "Azimuthal anchoring of nematic on undulated substrate: Elasticity versus memory," Eur. Phys. J. B **6**, 83–91 (1998).

[87] G. P. Crawford, R. J. OndrisCrawford and J. W. Doane, "Systematic study of orientational wetting and anchoring at a liquid-crystal-surfactant interface," Phys. Rev. E **53**, 3647–3661 (1996).

[88] A. L. Alexe-Ionescu, G. Barbero and S. Ponti, "Anchoring energy for the nematic liquid crystal Langmuir-Blodgett film interface," Liq. Cryst. **20**, 17–22 (1996).

[89] G. P. Bryan-Brown, M. J. Towler, M. S. Bancroft and D. G. McDonnell, "Bistable nematic alignment using bigratings," in *Conference Record of the International Display Research Conference* (SID, Montery, California, 1994), pp. 209–212.

[90] V. Sergan and G. Durand, "Anchoring Anisotropy Of A Nematic Liquid-Crystal On A Bistable Sio Evaporated Surface," Liq. Cryst. **18**, 171–174 (1995).

[91] C. Y. Huang, C. H. Lin, J. R. Wang, C. W. Huang, M. S. Tsai and A. Y. G. Fuh, "Multidirectional rubbed liquid-crystal cells," J. Appl. Phys. **92**, 7231–7235 (2002).

[92] O. O. Ramdane, P. Auroy, S. Forget, E. Raspaud, P. Martinot-Lagarde and I. Dozov, "Memory-free conic anchoring of liquid crystals on a solid substrate," Phys. Rev. Lett. **84**, 3871–3874 (2000).

[93] I. Dozov, D. N. Stoenescu, S. Lamarque-Forget, P. Martinot-Lagarde and E. Polossat, "Planar degenerated anchoring of liquid crystals obtained by surface memory passivation," Appl. Phys. Lett. **77**, 4124–4126 (2000).

[94] I. Janossy, "High-precision measurement of azimuthal rotation of liquid crystals on solid substrates," J. Appl. Phys. **98**, 043 523 (2005).

[95] I. Janossy and T. I. Kosa, "Gliding of liquid crystals on soft polymer surfaces," Phys. Rev. E **70**, 052 701 (2004).

[96] A. Rapini and M. Papoular, "Distorsion d'une lamelle nematique sous champ magnetique," J. Phys. (Paris) Coll. **30**, C4–54 (1969).

[97] A. Sugimura, G. R. Luckhurst and O. Y. Zhongcan, "Director deformation of a twisted chiral nematic liquid-crystal cell with weak anchoring boundaries," Phys. Rev. E **52**, 681–689 (1995).

[98] M. E. Becker, J. Nehring and T. J. Scheffer, "Theory of twisted nematic layers with weak boundary coupling," J. Appl. Phys. **57**, 4539–4542 (1985).

[99] W. Zhao, C. X. Wu and M. Iwamoto, "Weak boundary anchoring, twisted nematic effect, and homeotropic to twisted-planar transition," Phys. Rev. E **65**, 031 709 (2002).

[100] T. Beica, S. Frunza, R. Moldovan and D. N. Stoenescu, "Orientational structures in chiral nematic liquid crystals for weak anchoring," Mol. Cryst. Liq. Cryst. **301**, 39–55 (1997).

[101] C. V. Brown, M. J. Towler, V. C. Hui and G. P. Bryan-Brown, "Numerical analysis of nematic liquid crystal alignment on asymmetric surface grating structures," Liq. Cryst. **27**, 233–242 (2000).

[102] W. Zhao, C. X. Wu and M. Iwamoto, "Analysis of weak-anchoring effect in nematic liquid crystals," Phys. Rev. E **62**, R1481–R1484 (2000).

[103] J. H. Kim, M. Yoneya and H. Yokoyama, "Tristable nematic liquid-crystal device using micropatterned surface alignment," Nature **420**, 159–162 (2002).

[104] M. Yoneya, K. Iwasaki, Y. Tomioka and K. Kondo, "Cell gap margin enlargement of in-plane switching mode liquid crystal displays using weak-anchoring effects," Appl. Phys. Lett. **74**, 803–805 (1999).

[105] C.-S. H. Khoo and F. Simoni, *Physics of Liquid Crystalline Materials* (Gordon and Breach Science Publishers, 1991).

[106] D. Andrienko, F. Barbet, D. Bormann, Y. Kurioz, S. B. Kwon, Y. Reznikov and M. Warenghem, "Electrically controlled director slippage over a photosensitive aligning surface; in-plane sliding mode," Liq. Cryst. **27**, 365–370 (2000).

[107] E. Polossat and I. Dozov, "New optical method for the measurement of the azimuthal anchoring energy of nematic liquid crystals," Mol. Cryst. Liq. Cryst. **282**, 223–233 (1996).

[108] S. Faetti, M. Gatti and V. Palleschi, "A New Torsion Pendulum Technique To Measure The Twist Elastic-Constant Of Liquid-Crystals," J. De Phys. Lett. **46**, L881–L886 (1985).

[109] S. Faetti, M. Gatti, V. Palleschi and T. J. Sluckin, "Almost Critical-Behavior Of The Anchoring Energy At The Interface Between A Nematic Liquid-Crystal And A SiO Substrate," Phys. Rev. Lett. **55**, 1681–1684 (1985).

[110] J. Sicart, "Method Of Measuring Anchoring Energy Of A Nematic application To Anchoring On An Untreated Plate," J. De Phys. Lett. **37**, L25–L27 (1976).

[111] M. Kleman and C. Williams, "Anchoring Energies And Nucleation Of Surface Disclination Lines In Nematics," Phil. Mag. **28**, 725–731 (1973).

[112] G. Ryschenkow and M. Kleman, "Surface Defects And Structural Transitions In Very Low Anchoring Energy Nematic Thin-Films," J. Chem. Phys. **64**, 404–412 (1976).

[113] S. Faetti, "Measurements of the azimuthal anchoring energy at a polyimide-nematic interface with a new transmitted light method," Mol. Cryst. Liq. Cryst. **421**, 225–234 (2004).

[114] S. Faetti and M. Nobili, "An accurate optical method for measuring the azimuthal anchoring energy of nematic liquid crystals," Liq. Cryst. **25**, 487–494 (1998).

[115] B. S. Zhang, P. Sheng and H. S. Kwok, "Optical measurement of azimuthal anchoring strength in nematic liquid crystals," Phys. Rev. E **67**, 041 713 (2003).

[116] S. Faetti, G. C. Mutinati and I. Gerus, "Measurements of the azimuthal anchoring energy at the interface between a nematic liquid crystal and photosensitive polymers," Mol. Cryst. Liq. Cryst. **421**, 81–93 (2004).

[117] I. Dierking, *Textures of Liquid Crystals* (Wiley-VCH Verlag GmbH & Co. KGaA, Weinheim, 2003).

[118] P. Vetter, Y. Ohmura and T. Uchida, "Study of memory alignment of nematic liquid-crystals on polyvinyl-alcohol coatings," Jpn. J. Appl. Phys. Part 2-Letters **32**, L1239–L1241 (1993).

[119] G. P. Bryan-Brown, E. L. Wood and I. C. Sage, "Weak surface anchoring of liquid crystals," Nature **399**, 338–340 (1999).

[120] I. R. Peterson, "Langmuir-blodgett-films," J. Phys. D-Appl. Phys. **23**, 379–395 (1990).

[121] D. de Boer, R. Cortie, A. Pearson, M. Becker, H. Whler, D. Olivero, O. Peverini, K. Neyts, E. Kriezis and S. Elston, "Optical simulations and measurements of In-Plane Switching structures with rapid refractive-index variations," in *International Symposium Digest of Technical Papers* (SID, San Jose, California, USA, 2001), pp. 818–821.

[122] C. Desimpel, F. Beunis, H. Desmet and K. Neyts, "Experiments on azimuthal degenerated anchoring surfaces," in *Programme & Abstracts of the 16th Conference on Liquid Crystals (Chemistry, Physics & Applications)* (Military University of Technology Warschau, Stare Jabłonki, Poland, 2005), p. 69.

[123] C. Desimpel, F. Beunis, H. Desmet and K. Neyts, "Experiments on azimuthal degenerated anchoring surfaces," (2006), accepted for publication in Proceedings of SPIE.

[124] A. J. Davidson, S. J. Elston and E. P. Raynes, "Optical properties of the cartwheel cell," J. Phys. D-Appl. Phys. **38**, 376–384 (2005).

[125] R. Yamaguchi, T. Yamanaka and S. Sato, "Liquid-crystal optical rotator using weak azimuthal anchoring surface," Jpn. J. Appl.

Phys. Part 1-Regular Papers Short Notes & Rev. Papers **40**, 6522–6525 (2001).

[126] H. R. Kim, Y. W. Lee, S. J. Kim, D. W. Kim, C. J. Yu, B. Lee and S. D. Lee, "A rotatable waveplate using a vertically aligned deformed-helix ferroelectric liquid crystal," Ferroelectrics **312**, 479–484 (2004).

[127] I. Dierking, L. Komitov and S. T. Lagerwall, "On in-plane smectic layer reorientation in ferroelectric liquid crystal cells," Jpn. J. Appl. Phys. Part 2-Letters **37**, L57–L60 (1998).

[128] M. Ozaki, H. Moritake, K. Nakayama and K. Yoshino, "Smectic Layer Rotation In Antiferroelectric Liquid-Crystal," Jpn. J. Appl. Phys. Part 2-Letters **33**, L1620–L1623 (1994).

[129] K. Nakayama, H. Moritake, M. Ozaki and K. Yoshino, "Smectic layer rotation in ferroelectric liquid crystals," Jpn. J. Appl. Phys. Part 2-Letters **34**, L1599–L1602 (1995).

[130] P. H. Moon, *Field theory handbook: Including coordinate systems, differential equations, and their solutions* (Springer-Verlag, 1988).

[131] I. Dozov, M. Nobili and G. Durand, "Fast bistable nematic display using monostable surface switching," Appl. Phys. Lett. **70**, 1179–1181 (1997).

[132] C. Y. Xiang, X. W. Sun and X. J. Yin, "Fast response wide viewing angle liquid crystal cell with double-side fringe-field switching," Appl. Phys. Lett. **83**, 5154–5156 (2003).

[133] C. Desimpel, J. Beeckman, H. Desmet, K. Neyts, R. James and F. Fernández, "A four-electrode liquid crystal device for 2π in-plane director rotation," J. Phys. D-Appl. Phys. **38**, 3976–3984 (2005).

[134] C. Desimpel, K. Neyts, S. Verstuyft, D. Van Thourhout, K. D'havé and P. Rudquist, "Optical measurements on a new reconfigurable liquid crystal wave plate," in *Book of Abstracts of the International Workshop on Liquid Crystals for Photonics (26-28 April 2006, Gent, Belgium)* (Universiteit Gent, Gent, Belgium, 2006), pp. O–19.

[135] C. Desimpel, K. Neyts, S. Verstuyft, D. Van Thourhout, K. D'havé and P. Rudquist, "Optical simulations and measurements on a

new reconfigurable liquid crystal wave plate," Accepted for oral presentation at the 21st International Liquid Crystal Conference (2–7 July 2006, Keystone, Colorado, USA).

List of Publications

[Ada01] A. Adamski, H. Pauwels, C. Desimpel and S. Vermael, "Simulation of V-shaped stability in AFLC," in *XIV Conference on Liquid Crystals (Chemistry, Physics and Applications). CLC2001 Zakopane, Poland*, P. Perkowski, ed. (Military University of Technology Warschau, Warsaw, 2001), p. O5.

[Des01:1] C. Desimpel, K. Neyts, I. Janevska, A. Gjurcinovski, D. K. G. de Boer and R. Cortie, "Polarization state of the diffraction peaks in In-Plane Switching Cells," in *Proceedings of the 21st International Display Research Conference in conjunction with The 8th International Display Workshops* (SID, Nagoya, Japan, 2001), pp. 161–164.

[Ver01] S. Vermael, K. Neyts, C. Desimpel, D. de Boer, S. Day, A. Fernandez, P. Trwoga and F. Lanowith, "Two-dimensional Monte Carlo based Ion Transport algorithm in Liquid Crystals," in *Proceedings of the 21st International Display Research Conference in conjunction with The 8th International Display Workshops* (SID, Nagoya, Japan, 2001), pp. 33–35.

[Des01:2] C. Desimpel, K. Neyts, I. Janevska, A. Gjurcinovski, D. de Boer and R. Cortie, "Polarization state of the diffraction peaks in In-Plane Switching cells," in *Second FTW PhD Symposium* (2001), pp. 1–2.

[Ver02] S. Vermael, G. Stojmenovik, C. Desimpel, A. Adamski and K. a. Neyts, "Ion Currents in In-Plane Switching Liquid Crystal Displays," in *Proceedings of the 22nd International Display Research Conference / Eurodisplay* (SID, 2002), pp. 187–190.

[Ada02:1] A. Adamski, H. Pauwels, K. Neyts, C. Desimpel, G. Stojmenovik and S. Vermael, "The Non-uniform Theory Simula-

tions of the Continuous Director Rotation Mode of FLCD's," in *Proceedings of the 22nd International Display Research Conference / Eurodisplay* (SID, Nice, France, 2002), pp. 501–504.

[Ada02:2] A. Adamski, H. Pauwels, K. Neyts, C. Desimpel and S. Vermael, "Simulation of V-shaped stability in AFLC," in *Proceedings of SPIE. XIV Conference on Liquid Crystals: Chemistry, Physics and Applications* (SPIE, Washington, USA, 2002), pp. 127–134.

[Sto02] G. Stojmenovik, K. Neyts, S. Vermael, A. Verschueren, R. Van Asselt, C. Desimpel and A. Adamski, "Measurements of lateral ion transport in LCD cells, 075," in *Third FTW PhD Symposium*, K. Neyts, ed. (2002).

[Ney03] K. Neyts, S. Vermael, C. Desimpel, G. Stojmenovik, A. Verschueren, D. de Boer, R. Snijkers, P. Machiels and A. van Brandenburg, "Lateral ion transport in nematic liquid-crystal devices," J. Appl. Phys. **94**, 3891–3896 (2003).

[Des03:1] C. Desimpel, K. Neyts, D. Olivero, C. Oldano, D. K. G. de Boer and R. Cortie, "Optical transmission model for thin two-dimensional layers," in *Book of Abstracts, 10th International Topical Meeting on Optics of Liquid Crystals* (Université d'Artois, Aussois, France, 2003), p. 75.

[Des03:2] C. Desimpel, K. Neyts, D. Olivero, C. Oldano, D. de Boer and R. a. Cortie, "Optical transmission model for thin two-dimensional layers," in *Fourth FTW PhD Symposium* (FTW, Universiteit Gent, Gent, 2003), pp. 1–2.

[Sto04] G. Stojmenovik, K. Neyts, S. Vermael, C. Desimpel, A. Adamski, A. R. Verschueren and R. a. Van Asselt, "Measurements of lateral ion transport in LCD cells," Mol. Cryst. Liq. Cryst. **409**, 515–527 (2004).

[Des04] C. Desimpel, K. Neyts, D. Olivero, C. Oldano, D. K. G. de Boer and R. Cortie, "Optical transmission model for thin two-dimensional layers," Mol. Cryst. Liq. Cryst. **422**, 185–195 (2004).

[Des05:1] C. Desimpel, F. Beunis, H. Desmet and K. Neyts, "Experiments on azimuthal degenerated anchoring surfaces," in

Programme & Abstracts of the 16th Conference on Liquid Crystals (Chemistry, Physics & Applications) (Military University of Technology Warschau, Stare Jabłonki, Poland, 2005), p. 69.

[Des05:2] C. Desimpel, J. Beeckman, H. Desmet, K. Neyts, R. James and F. Fernández, "A four-electrode liquid crystal device for 2π in-plane director rotation," J. Phys. D-Appl. Phys. **38**, 3976–3984 (2005).

[Des06:1] C. Desimpel, F. Beunis, H. Desmet and K. Neyts, "Experiments on azimuthal degenerated anchoring surfaces," (2006), accepted for publication in Proceedings of SPIE.

[Des06:2] C. Desimpel, K. Neyts, S. Verstuyft, D. Van Thourhout, K. D'havé and P. Rudquist, "Optical measurements on a new reconfigurable liquid crystal wave plate," in *Book of Abstracts of the International Workshop on Liquid Crystals for Photonics (26-28 April 2006, Gent, Belgium)* (Universiteit Gent, Gent, Belgium, 2006), pp. O–19.

[Des06:3] C. Desimpel, K. Neyts, S. Verstuyft, D. Van Thourhout, K. D'havé and P. Rudquist, "Optical simulations and measurements on a new reconfigurable liquid crystal wave plate," Accepted for oral presentation at the 21st International Liquid Crystal Conference (2–7 July 2006, Keystone, Colorado, USA).

Index